creative commons

COMMONS DEED

저작자표시-비영리-변경금지 **2.0** 대한민국

이용자는 아래의 조건을 따르는 경우에 한하여 자유롭게

- 이 저작물을 복제, 배포, 전송, 전시, 공연 및 방송할 수 있습니다.

다음과 같은 조건을 따라야 합니다:

저작자표시. 귀하는 원저작자를 표시하여야 합니다.

비영리. 귀하는 이 저작물을 영리 목적으로 이용할 수 없습니다.

변경금지. 귀하는 이 저작물을 개작, 변형 또는 가공할 수 없습니다.

- 귀하는, 이 저작물의 재이용이나 배포의 경우, 이 저작물에 적용된 이용허락조건을 명확하게 나타내어야 합니다.
- 저작권자로부터 별도의 허가를 받으면 이러한 조건들은 적용되지 않습니다.

저작권법에 따른 이용자의 권리는 위의 내용에 의하여 영향을 받지 않습니다.

이것은 이용허락규약(Legal Code)을 이해하기 쉽게 요약한 것입니다.

Disclaimer

dCollection

Doctoral Dissertation

VISIBLE LIGHT-ACTIVE PHOTOCATALYSIS AND ITS HYBRID SYSTEMS WITH FENTON-LIKE REACTION FOR OXIDATION OF ORGANIC POLLUTANTS

Jiwon Seo

Department of Urban and Environmental Engineering
(Environmental Science and Engineering)

Graduate School of UNIST

2019

VISIBLE LIGHT-ACTIVE PHOTOCATALYSIS AND ITS HYBRID SYSTEMS WITH FENTON-LIKE REACTION FOR OXIDATION OF ORGANIC POLLUTANTS

Jiwon Seo

Department of Urban and Environmental Engineering
(Environmental Science and Engineering)

Graduate School of UNIST

Visible light-active photocatalysis and its hybrid systems with the Fenton-like reaction for oxidation of organic pollutants

A dissertation
submitted to the Graduate School of UNIST
in partial fulfillment of the
requirements for the degree of
Doctor of Philosophy

Jiwon Seo

01/10/2019 of submission
Approved by

Advisor
Kyung Hwa Cho

Visible light-active photocatalysis and its hybrid systems with the Fenton-like reaction for oxidation of organic pollutants

Jiwon Seo

This certifies that the dissertation of Jiwon Seo is approved.

01/10/2019 of submission

Advisor: Kyung Hwa Cho

Young-Nam Kwon

Changsoo Lee

Changha Lee

Kangwoo Cho

ABSTRACT

Various recalcitrant organic pollutants in water have become a worldwide concern and advanced oxidation processes (AOPs) have been suggested as an effective solution to control these compounds. However, the processes usually require an excess amount of energy for water treatment. Among the AOPs, a photocatalytic reaction has received huge attention due to the simultaneous reaction of energy production and water treatment, ideally.

Most of the photocatalysts for water treatment only can utilize UV-light energy in the sunlight. However, visible light occupies the largest part of the total irradiance spectrum of sunlight. Therefore, many researchers have tried to change band level to utilize a huge amount of visible light energy. A variety of approaches have been attempted to extend the range of light spectrum available for photocatalysts activation to the visible-light region, including metal and non-metal doping, dye photosensitization, and ligand to metal charge transfer (LMCT), etc.

This study investigated the visible light active photocatalysis and its hybrid systems with Fenton-like reaction for degradation of organic pollutants. Several visible light active photocatalysts (Am-peroxo-titania, S-TiO_2, and g-C_3N_4-AQ) were synthesized and the photochemical activities for the oxidation of organic compounds were examined.

Firstly, amorphous peroxo-titania (denoted as Am-peroxo-TiO_2), synthesized in this study by a facile method, demonstrated photochemical activity for the oxidation of organic pollutants under visible light illumination (λ > 400 nm). Am-peroxo-TiO_2 was synthesized by a one-step sol-gel method using titanium isopropoxide and hydrogen peroxide (H_2O_2) at room temperature and atmospheric pressure. The material produced was a yellow powdered precipitate; the measurement of diffuse reflectance confirmed light absorption of up to 600 nm. High-resolution transmission electron microscopy (HRTEM) revealed that Am-peroxo-TiO_2 forms aggregates of small nanoparticles (ca < 10 nm). The surface peroxo-groups (Ti-OOH or Ti-OO-Ti) were characterized by Fourier-transform infrared spectroscopy (FT-IR) and X-ray photoelectron spectroscopy (XPS). Visible light-illuminated Am-peroxo-TiO_2 completely degraded 10 μM 4-chlorophenol (4-CP) in 4 h. The photochemical activity of Am-peroxo-TiO_2 was selective to the target organic compound. Experiments using scavengers and probes of reactive oxidants revealed that reactive oxygen species such as hydroxyl and superoxide radicals are not responsible for the degradation of organic compounds. Liquid chromatography-mass spectrometry showed that 4-CP was oxidized to produce 4-chlorocatechol, hydroquinone, and benzoquinone as primary products. The results suggest that oxidation is initiated by electron abstraction or hydroxylation by the photogenerated reactive intermediates on the peroxo surface. Am-peroxo-TiO_2 was stable under both dark and illuminated conditions in the absence of organic compounds. Importantly, in the presence of organic compounds, the photochemical activity of

Am-peroxo-TiO_2 gradually decreased. Further, platinization enhanced the photochemical activity as well as the stability of Am-peroxo-TiO_2.

Secondly, sulfur doped TiO_2 (denoted as S-TiO_2) demonstrated its visible light photocatalytic activity with Fenton-like reagents (Fe(III) and H_2O_2) for degradation of organic compounds. S-TiO_2 exhibited a small rectangular-shaped crystalline structure which is composed of the mixture of anatase and rutile crystalline phases. FT-IR and X-ray fluorescence (XRF) analysis confirmed Ti-O-S on the surface of S-TiO_2. In photochemical activity, visible light-illuminated S-TiO_2/Fe(III) system completely degraded 10 μM 4-chlorophenol (4-CP) within 2 h. The photochemical activity of S-TiO_2/Fe(III) limited within pH 3.0 and was selective in degradation of the organic compound. Experiments using radical scavengers and oxidant probes revealed that the oxidation by photogenerated holes is responsible for the degradation of organic compounds by illuminated S-TiO_2/Fe(III) and the role of $^{\bullet}OH$ is negligible. Meanwhile, visible light-illuminated S-TiO_2/Fe(III)/H_2O_2 system effectively degraded 10 μM benzoic acid in 1h. The photochemical activity of S-TiO_2/Fe(III)/H_2O_2 also limited within pH 3.0 and was non-selective in degradation of the organic compound. Experiments using radical scavengers and oxidant probes revealed that $^{\bullet}OH$ is mainly responsible for the degradation of organic compounds by illuminated S-TiO_2/Fe(III)/H_2O_2. The repeated use of S-TiO_2/Fe(III) system decreased the photocatalytic activity for the 4-CP degradation, however, that of S-TiO_2/Fe(III)/H_2O_2 system maintained the photocatalytic activity for the BA degradation.

Lastly, anthraquinone anchored graphitic carbon nitride (denoted as g-C_3N_4-AQ), reported in the photochemical production of H_2O_2, demonstrated its visible light photocatalytic activity with Fe(III) for degradation of organic compounds. g-C_3N_4-AQ exhibited similar crystallinity and light absorption spectrum with the pristine g-C_3N_4. FT-IR and XPS confirmed the covalent bonds between AQ and g-C_3N_4. The visible light illuminated g-C_3N_4-AQ/Fe(III) showed different photochemical activities in accordance with the existence of dissolved oxygen. In visible light illuminated g-C_3N_4-AQ/Fe(III), experiments using various target organic compounds, radical scavengers, and oxidant probes elucidated that $^{\bullet}OH$ is responsible for the degradation of organic compounds in the presence of dissolved oxygen, however, hole is the main oxidant in the absence of dissolved oxygen.

CONTENTS

Abstract i

Contents iii

List of figures v

List of tables xiii

CHAPTER 1. INTRODUCTION 1

- **I. Research background** 1
- **II. Research trend of photocatalyst** 4
- **III. Objectives of the study** 7

CHAPTER 2. MATERIALS AND METHODS 8

- **I. Reagents** 8
- **II. Synthesis of photocatalyst** 8
  - **1. Amorphous peroxo-titania (Am-peroxo-TiO_2)** 8
  - **2. Sulfur doped TiO_2 (S-TiO_2)** 8
  - **3. Anthraquinone anchored graphitic carbon nitride (g-C_3N_4-AQ)** 9
- **III. Characterization** 9
- **IV. Photochemical experiments** 9
- **V. Analytical methods** 10

CHAPTER 3. RESULTS AND DISCUSSION 12

- **I. Am-peroxo-TiO_2** 12
  - **1. Results** 12
    - 1.1. Synthesis and characterization of Am-peroxo-TiO_2 12
    - 1.2. Photochemical degradation of organic compounds 17

1.3. Photostability of Am-peroxo-TiO_2 20

1.4. Oxidation products of 4-CP 23

2. Discussion 28

2.1. Photochemical activity of Am-peroxo-TiO_2 28

2.2. Roles of ROS 29

2.3. Photochemical reactions of illuminated Am-peroxo-TiO_2 30

2.4. Mechanism of organic compound degradation by illuminated Am-peroxo-TiO_2 31

II. Sulfur doped TiO_2 (S-TiO_2) 35

1. Results 35

1.1. Synthesis and characterization of S-TiO_2 35

1.2. Photochemical degradation of organic compounds 37

1.3. Effect of radical scavengers 42

1.4. Oxidant production 43

1.5. Repetition test under visible light illumination 44

2. Discussion 45

2.1. Roles of ROS 45

2.2. Photochemical mechanisms for the degradation of organic compounds 45

III. Anthraquinone anchored graphitic carbon nitride (g-C_3N_4-AQ) 48

1. Results 48

1.1. Synthesis and characterization of g-C_3N_4-AQ 48

1.2. Photochemical reaction of g-C_3N_4-AQ 53

1.3 Effect of AQ loading and Fe(III) injection 54

1.4 Photochemical degradation of various organic compounds 57

1.5. Effect of ROS scavengers 59

1.6. Oxidant production 59

2. Discussion 60

2.1. Roles of ROS 60

2.2. Photochemical mechanisms for the degradation of organic compounds 61

CHAPTER 4. CONCLUSIONS 63

REFERENCES 65

감사의 글 74

List of figures

Fig. 1.1. Advanced oxidation processes. **1**

Fig. 1.2. The general mechanism of photocatalytic reaction. **2**

Fig. 1.3. Total irradiation spectrum of sunlight. **3**

Fig. 1.4. Metal and non-metal doping in photocatalyst. **4**

Fig. 2.1. Light emission spectra of the fluorescent lamp (a) and the xenon arc lamp (b) with a 400 nm longpass filter. **10**

Fig. 3.1.1. Photographs of Am-peroxo-TiO_2 synthesized with varying H_2O_2 concentrations and drying temperature, and photochemical degradation of 4-CP using synthesized materials under visible light illumination (time-concentration profiles and pseudo first-order rate constants): effects of H_2O_2 concentration ((a) – (c)) and drying temperature ((d) – (f)) ([Am-peroxo-TiO_2] = 0.5 g/L, $[4\text{-CP}]_0$ = 10 μM, pH = 5, I = 6.43 × 10^{-6} Einstein/L·s (fluorescent lamp, λ > 400 nm). **13**

Fig. 3.1.2. Diffuse reflectance spectra of Am-peroxo-TiO_2 (a) and X–ray diffraction patterns of Am-peroxo-TiO_2 prepared at different drying temperature (b). **14**

Fig. 3.1.3. HR-TEM images of Am-peroxo-TiO_2 prepared at different drying temperature (a), HR-TEM image (b), and EDX spectra of Am-peroxo-TiO_2 (50°C). **15**

Fig. 3.1.4. X–ray photoelectron spectra (O 1s level) and FT-IR spectra of Am-peroxo-TiO_2 ((a) and (b)), and TiO_2 (Degussa P25) ((c) and (d)). **16**

Fig. 3.1.5. Degradation of 4-CP by Am-peroxo-TiO_2 under visible-light illumination: comparison with control TiO_2 photocatalysts and dechlorination of 4-CP by Am-peroxo-TiO_2 (a) comparison of different light sources (b) ([Am-peroxo-TiO_2] = 0.5 g/L, $[4\text{-CP}]_0$ = 10 μM, pH = 5, I = 6.43 × 10^{-6} Einstein/L·s (fluorescent lamp, λ > 400 nm), $[TiO_2]_0$ = 0.5 g/L for (a), I = 2.46 × 10^{-5} Einstein/L·s (xenon arc lamp, λ > 400 nm) for (b)). **17**

Fig. 3.1.6. Degradation of 4-CP (a) and TOC removal (b) by Am-peroxo-TiO_2 under visible light illumination ([Am-peroxo-TiO_2] = 0.5 g/L, $[4\text{-CP}]_0$ = 0.1 mM, pH = 5, I = 6.43 × 10^{-6}

Einstein/L·s (fluorescent lamp, λ > 400 nm)). **18**

Fig. 3.1.7. Degradation of organic compounds by Am-peroxo-TiO_2 under visible light illumination ([Am-peroxo-TiO_2] = 0.5 g/L, $[4\text{-CP}]_0 = [\text{Phenol}]_0 = [\text{BA}]_0 = [\text{AAP}]_0 = [\text{CBZ}]_0 = 10$ μM, pH = 5, I = 6.43×10^{-6} Einstein/L·s (fluorescent lamp, λ > 400 nm)). **18**

Fig. 3.1.8. Degradation of 4-CP by Am-peroxo-TiO_2 under visible light illumination: effects of ROS scavengers (a), and dissolved oxygen (b) ([Am-peroxo-TiO_2] = 0.5 g/L, $[4\text{-CP}]_0$ = 10 μM, pH = 5, I = 6.43×10^{-6} Einstein/L·s (fluorescent lamp, λ > 400 nm), $[\text{Methanol}]_0$ = [*tert*-Butanol]$_0$ = 200 mM for (a)). **19**

Fig. 3.1.9. Formation of XTT-formazan by Am-peroxo-TiO_2 under visible light illumination ([Am-peroxo-TiO_2] = 0.5 g/L, $[\text{XTT}]_0$ = 0.1 mM, pH = 5, I = 6.43×10^{-6} Einstein/L·s (fluorescent lamp, λ > 400 nm)). **20**

Fig. 3.1.10. Repeated degradation of 4-CP by Am-peroxo-TiO_2 (and Pt-Am-peroxo-TiO_2) under visible light irradiation: effect of pre-illumination (a) and comparison with Pt-Am-peroxo-TiO_2 (b) ([Am-peroxo-TiO_2] = 0.5 g/L, pH = 5, I = 6.43×10^{-6} Einstein/L·s (fluorescent lamp, λ > 400 nm), $[4\text{-CP}]_0$ = 1 μM for (a), [Pt-Am-peroxo-TiO_2]$_0$ = 0.5 g/L and $[4\text{–CP}]_0$ = 10 μM for (b)). **21**

Fig. 3.1.11. Repeated degradation of 4-CP by Am-peroxo-TiO_2 under visible light illumination ([Am-peroxo-TiO_2] = 0.5 g/L, $[4\text{-CP}]_0$ = 10 μM, pH = 5, I = 6.43×10^{-6} Einstein/L·s (fluorescent lamp, λ > 400 nm)). **22**

Fig. 3.1.12. Generation of Fe(III)/Fe(II) redox couple photocurrent of Am-peroxo-TiO_2 (and Pt-Am-peroxo-TiO_2) under visible light irradiation ([Am-peroxo-TiO_2]$_0$ = [Pt-Am-peroxo-TiO_2]$_0$ = 0.5 g/L, $[4\text{–CP}]_0$ = 0.1 mM, $[NaClO_4]_0$ = 0.1 M, $[\text{Fe(III)}]_0$ = 1 mM, pH = 1.8, I = 2.46×10^{-5} Einstein/L·s (xenon arc lamp, λ > 400 nm), working and counter electrodes = platinum plate (2.5 cm x 1.5 cm), reference electrode = Calomel electrode, bias potential = +0.7 V). **23**

Fig. 3.1.13. Formation of oxidation products during 4-CP degradation by Am-peroxo-TiO_2 under visible light illumination ([Am-peroxo-TiO_2] = 0.5 g/L, $[4\text{-CP}]_0$ = 0.1 mM, pH = 5, I = 6.43×10^{-6} Einstein/L·s (fluorescent lamp, λ > 400 nm)). **25**

Fig. 3.1.14. Formation of oxidation products during 4-CP degradation by Am-peroxo-TiO_2 under visible light illumination ([Am-peroxo-TiO_2] = 0.5 g/L, $[4\text{-CP}]_0$ = 0.1 mM, pH = 5, I = 6.43 × 10^{-6} Einstein/L·s (fluorescent lamp, λ > 400 nm)). **26**

Fig. 3.1.15. Formation of oxidation products during 4-CP degradation by Am-peroxo-TiO_2 under visible light illumination: chromatograms of oxidation products at 4h with mass spectra ([Am-peroxo-TiO_2] = 0.5 g/L, $[4\text{-CP}]_0$ = 0.1 mM, pH = 5, I = 6.43 × 10^{-6} Einstein/L·s (fluorescent lamp, λ > 400 nm)). **27**

Fig. 3.1.16. Pathways depicting oxidative degradation of 4-CP by Am-peroxo-TiO_2 under visible light illumination. **28**

Fig. 3.1.17. Production of HCHO, 4-HBA, and 7-HC by Am-peroxo-TiO_2 under visible light illumination. ([Am-peroxo-TiO_2] = 0.5 g/L, $[\text{Methanol}]_0$ = 200 mM, $[\text{BA}]_0$ = 10 mM, $[\text{Coumarin}]_0$ = 1 mM, pH = 5, I = 6.43 × 10^{-6} Einstein/L·s (fluorescent lamp, λ > 400 nm)). .. **30**

Fig. 3.1.18. Schematic diagrams of photochemical reactions occurring on visible light-illuminated Am-peroxo-TiO_2 in the absence (a) and presence (b) of organic compounds. **31**

Fig. 3.1.19. Proposed mechanisms for primary oxidation of 4-CP by visible light-illuminated Am-peroxo-TiO_2. .... **32**

Fig. 3.1.20. X-ray photoelectron spectra (O 1s level) of Am-peroxo-TiO_2 (a, b) and Pt-Am-peroxo-TiO_2 (c, d) before (a, c) and after (b, d) 4-CP degradation under visible light illumination ($[\text{Am-peroxo-TiO}_2]_0$ = $[\text{Pt-Am-peroxo-TiO}_2]_0$ = 0.5 g/L, $[4\text{-CP}]_0$ = 10 μM, pH = 5, I = 6.43 × 10^{-6} Einstein/L·s (fluorescent lamp, λ > 400 nm)). **33**

Fig. 3.1.21. Diffuse reflectance spectra of Am-peroxo-TiO_2 (a) and Pt-Am-peroxo-TiO_2 (b) before and after 4-CP degradation under visible light illumination ([Am-peroxo-TiO_2] = [Pt-Am-peroxo-TiO_2] = 0.5 g/L, $[4\text{-CP}]_0$ = 10 μM, pH = 5, I = 6.43 × 10^{-6} Einstein/L·s (fluorescent lamp, λ > 400 nm)). **34**

Fig. 3.2.1. XRD pattern (a) and HRTEM image (b) of S-TiO_2. Notations 'A' and 'R' in (a) represent anatase and rutile crystalline phase. **35**

Fig. 3.2.2. FT-IR spectra of S-TiO_2 and TiO_2 (degussa P25). **36**

Fig. 3.2.3. Diffuse reflectance spectrum (a), valence band XPS (b), and electronic band structure (c) of S-TiO_2. .... **37**

Fig. 3.2.4. Degradation of 4-CP (a) and reduction of Fe(III) (b) by S-TiO_2/Fe(III) system under visible light illumination ([S-TiO_2] = 0.5 g/L, $[Fe(III)]_0$ = 0.1 mM, $[4\text{-}CP]_0$ = 10 μM, pH = 3, I = 6.43×10^{-6} Einstein/L·s (fluorescent lamp, λ > 400 nm)). **38**

Fig. 3.2.5. Pseudo-first order rate constants for the degradation of 4-CP as a function of pH (a) and dose of Fe(III) (b) by S-TiO_2/Fe(III) system under visible light illumination ([S-TiO_2] = 0.5 g/L, $[4\text{-}CP]_0$ = 10 μM, I = 6.43×10^{-6} Einstein/L·s (fluorescent lamp, λ > 400 nm), $[Fe(III)]_0$ = 0.1 mM for (a), pH = 3 for (b)). **39**

Fig. 3.2.6. Degradation of benzoic acid by S-TiO_2/Fe(III)/H_2O_2 systems under (a) dark condition and (b) visible light illumination ([S-TiO_2] = 0.5 g/L, $[Fe(III)]_0$ = 0.1 mM, $[H_2O_2]_0$ = 0.1 mM, $[BA]_0$ = 10 μM, pH = 3, I = 6.43×10^{-6} Einstein/L·s (fluorescent lamp, λ > 400 nm)). **40**

Fig. 3.2.7. Pseudo-first order rate constants for the degradation of benzoic acid as a function of pH (a), dose of Fe(III) (b), and dose of H_2O_2 (c) by S-TiO_2/Fe(III)/H_2O_2 system under visible light illumination ([S-TiO_2] = 0.5 g/L, $[BA]_0$ = 10 μM, I = 6.43×10^{-6} Einstein/L·s (fluorescent lamp, λ > 400 nm), $[H_2O_2]_0$ = 0.1 mM for (a) and (b), $[Fe(III)]_0$ = 0.1 mM for (a) and (c), pH = 3 for (b) and (c)). **41**

Fig. 3.2.8. Degradation of organic compounds by S-TiO_2/Fe(III) (a) and S-TiO_2/Fe(III)/H_2O_2 (b) under visible light illumination (([S-TiO_2] = 0.5 g/L, $[Fe(III)]_0$ = 0.1 mM, $[Phenol]_0$ = $[4\text{-}CP]_0$ = $[BA]_0$ = $[CBZ]_0$ = 10 μM, pH = 3, I = 6.43×10^{-6} Einstein/L·s (fluorescent lamp, λ > 400 nm)...... .... **42**

Fig. 3.2.9. Degradation of organic compounds by S-TiO_2/Fe(III) (a) and S-TiO_2/Fe(III)/H_2O_2 (b) under visible light illumination: effects ROS scavengers (([S-TiO_2] = 0.5 g/L, $[Fe(III)]_0 = 0.1$ mM, $[Methanol]_0$ = [*tert*-Butanol]$_0$ = 200 mM, pH = 3, I = 6.43×10^{-6} Einstein/L·s (fluorescent lamp, $\lambda > 400$ nm), $[4\text{-CP}]_0 = 10$ μM for (a), $[BA]_0 = 10$ μM for (b), $[H_2O_2]_0 = 0.1$ mM for (b)). **43**

Fig. 3.2.10. Production of HCHO, 4-HBA, and 7-HC by S-TiO_2/Fe(III) (a) and S-TiO_2/Fe(III)/H_2O_2 (b) under visible light illumination ([S-TiO_2] = 0.5 g/L, $[Fe(III)]_0 = 0.1$ mM, $[Methanol]_0 = 200$ mM, [Benzoic acid]$_0$ = 10 mM, [Coumarin]$_0$ = 1 mM, pH = 3, I = 6.43×10^{-6} Einstein/L·s (fluorescent lamp, $\lambda > 400$ nm), $[H_2O_2]_0 = 0.1$ mM for (b)). **44**

Fig. 3.2.11. Repeated degradation of 4-CP by S-TiO_2/Fe(III) (a) and benzoic acid by S-TiO_2/Fe(III)/H_2O_2 (b) under visible light illumination (([S-TiO_2] = 0.5 g/L, $[Fe(III)]_0 = 0.1$ mM, pH = 3, I = 6.43×10^{-6} Einstein/L·s (fluorescent lamp, $\lambda > 400$ nm), $[4\text{-CP}]_0 = 10$ μM for (a), [benzoic acid]$_0$ = 10 μM for (b), $[H_2O_2]_0 = 0.1$ mM for (b)). **45**

Fig. 3.2.12. Photochemical reaction mechanisms for the degradation of organic compounds in S-TiO_2/Fe(III) system (a) and S-TiO_2/Fe(III)/H_2O_2 system (b). **47**

Fig. 3.3.1. X-ray diffraction patterns (a) and diffuse reflectance spectra (b)of g-C_3N_4 and g-C_3N_4-AQ. **48**

Fig. 3.3.2. Diffuse reflectance spectrum (a), valence band XPS (b), and electronic band structure (c) of g-C_3N_4 and g-C_3N_4-AQ. **49**

Fig. 3.3.3. FT-IR spectra of AQ, g-C_3N_4 and g-C_3N_4-AQ. Notations '#' and '*' in (b) – (e) represent the main IR absorption of g-C_3N_4 and AQ. **50**

Fig. 3.3.4. X-ray photoelectron spectra (C 1s ((a) and (d)), O 1s ((b) and (e)), and N 1s ((c) and (f)) levels) of g-C_3N_4 ((a) – (c)) and g-C_3N_4-AQ ((d) –(f)). **52**

Fig. 3.3.5. Production of H_2O_2 by photocatalytic systems under visible light illumination: Dark condition (a) and light illumination condition (b) ([Catalyst] = 0.5 g/L, pH=3, Xenon lamp (150 W, $\lambda > 400$ nm) for (b))........ **53**

Fig. 3.3.6. Degradation of BA by photocatalytic systems under visible light illumination: In the absence of Fe(III) (a) and in the presence of Fe(III) (b) ([Catalyst] = 0.5 g/L, $[BA]_0 = 10$ μM, pH=3, Xenon lamp (150 W, $\lambda > 400$ nm), $[Fe(III)]_0 = 0.1$ mM for (b)). **54**

Fig. 3.3.7. Degradation of benzoic acid (a) and pseudo-first order rate constant of benzoic acid degradation (b) by varied g-C_3N_4-AQ/Fe(III) systems under visible light illumination: As dose of AQ ([g-C_3N_4-AQ] = 0.5 g/L, $[BA]_0 = 10$ μM, $[Fe(III)]_0 = 0.1$ mM, pH=3, Xenon lamp (150 W, $\lambda > 400$ nm)). **55**

Fig. 3.3.8. Degradation of benzoic acid (a), pseudo-first order rate constant of benzoic acid degradation (b) and reduction of Fe(III) (c) by varied g-C_3N_4-AQ/Fe(III) systems under visible light illumination: As dose of Fe(III) ([g-C_3N_4-AQ] = 0.5 g/L, $[BA]_0 = 10$ μM, pH=3, Xenon lamp (150 W, $\lambda > 400$ nm))........ **56**

Fig. 3.3.9. Degradation of organic compounds ((a) and (b)) and reduction of Fe(III) ((c) and (d)) by g-C_3N_4-AQ/Fe(III) systems under visible light illumination: air saturation ((a) and (c)) and deaeration ((b) and (d)) condition ([g-C_3N_4-AQ] = 0.5 g/L, $[Phenol]_0 = [4\text{-}CP]_0 = [BA]_0 = [CBZ]_0 = 10$ μM, $[Fe(III)]_0 = 0.1$ mM, pH=3, Xenon lamp (150 W, $\lambda > 400$ nm), N_2 gas sparging for (b)). **58**

Fig. 3.3.10. Degradation of organic compounds by g-C_3N_4-AQ/Fe(III) in the presence of ROS scavengers under visible light illumination: air saturation (a) and deaeration (b) condition (([g-C_3N_4-AQ] = 0.5 g/L, $[Fe(III)]_0 = 0.1$ mM, pH = 3, Xenon lamp (150 W, $\lambda > 400$ nm), $[BA]_0 = 10$ μM for (a), $[Methanol]_0$ = [*tert*-Butanol]$_0$ = 200 mM for (a), $[phenol]_0 = 10$ μM for (b), $[Methanol]_0$ = [*tert*-Butanol]$_0$ = 1 M for (b), N_2 gas sparging for (b))........ **59**

Fig. 3.3.11. Production of HCHO, 4-HBA, and 7-HC by g-C_3N_4-AQ/Fe(III) under visible light illumination: air saturation (a) and deaeration (b) condition (([g-C_3N_4-AQ] = 0.5 g/L, $[Fe(III)]_0$ = 0.1 mM, $[Methanol]_0$ = 200 mM, $[Benzoic\ acid]_0$ = 10 mM, $[Coumarin]_0$ = 1 mM, pH = 3, Xenon lamp (150 W, $\lambda > 400$ nm), N_2 gas sparging for (b)). **60**

Fig. 3.3.12. Photochemical reaction mechanisms for the degradation of organic compounds in g-C_3N_4-AQ/Fe(III) system in air-saturated (a) and deaerated (b) condition. **62**

List of Table

Table 3.1.1. Products of 4-CP degradation by visible light-illuminated Am-peroxo-TiO_2 identified by HPLC and LC/MS analyses. **24**

CHAPTER 1. INTRODUCTION

I. Research background

For decades, the developments of chemical and industrial processes have accelerated the emergence of recalcitrant pollutants in the aquatic systems. The recalcitrant pollutants such as pharmaceuticals and personal care products (PPCPs), polycyclic aromatic hydrocarbons (PAHs), polychlorinated biphenyls (PCBs), and endocrine disruptors have been raised as important issues in the water treatment process [1,2]. However, the traditional water treatment methods were insufficient to remove the recalcitrant pollutants [3,4]. It is the reason that advanced oxidation processes (AOPs) required.

AOPs, one of the powerful alternative water treatments, have been widely studied in the environmental remediation, which generate strong reactive oxidant species (ROS) such as hydroxyl radical ($^{\bullet}OH$) from ozonation [5-7], Fenton [8-11], γ-radiolysis [12], and photocatalysis [13,14] etc. (Fig. 1.1). However, those processes have yet to overcome the energy efficiencies and the operation cost competitiveness [15-17].

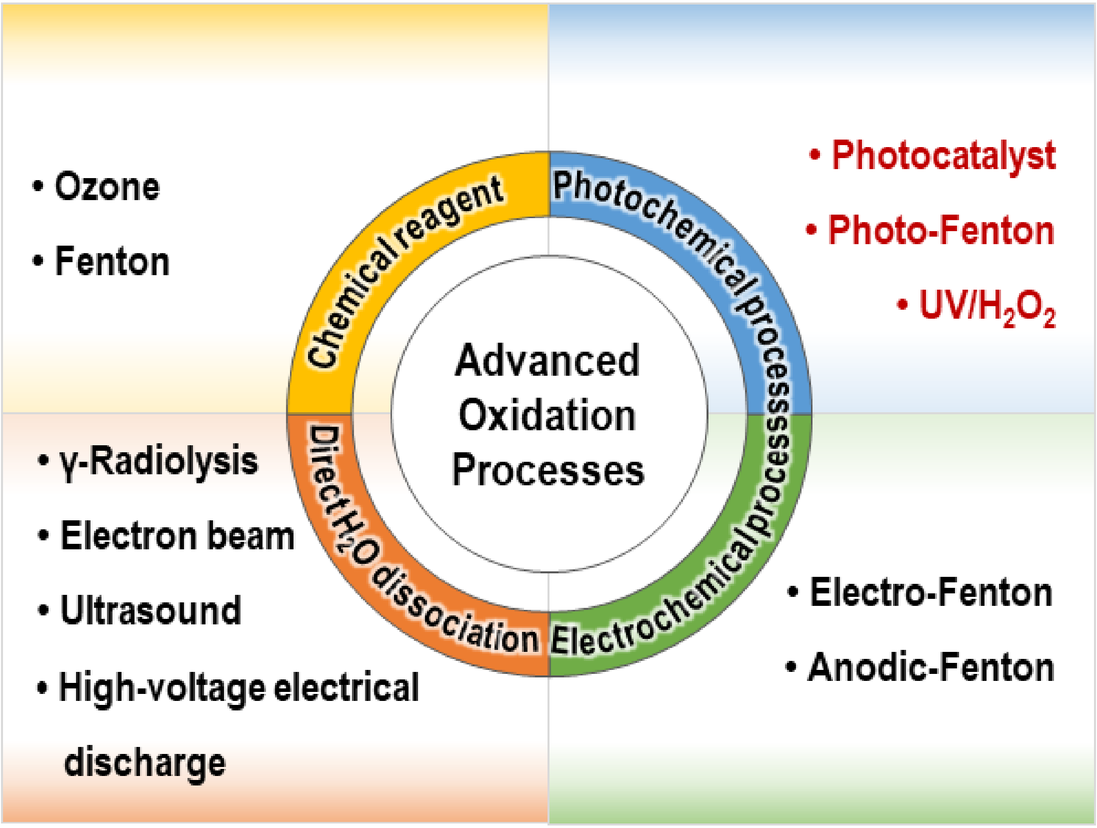
• Ozone
• Fenton
• Photocatalyst
• Photo-Fenton
• UV/H_2O_2
Chemical reagent
Photochemical processes
Advanced Oxidation Processes
Direct H_2O dissociation
Electrochemical processes
• γ-Radiolysis
• Electron beam
• Ultrasound
• High-voltage electrical discharge
• Electro-Fenton
• Anodic-Fenton

Fig. 1.1. Advanced oxidation processes.

Among AOPs, photocatalytic water treatment process has received spotlight as one of the ideal

AOP, which is possible to the simultaneous reaction of energy production and water treatment (Fig. 1.2). In detail, the photocatalytic reaction occurs from the illumination of light energy which can overcome the bandgap energy of photocatalyst. The hole (h^+) and electron (e^-) are separated by the light illumination, which leads to the production of energy resources (H_2, CH_4, and H_2O_2) and the degradation of organic compounds [18-24].

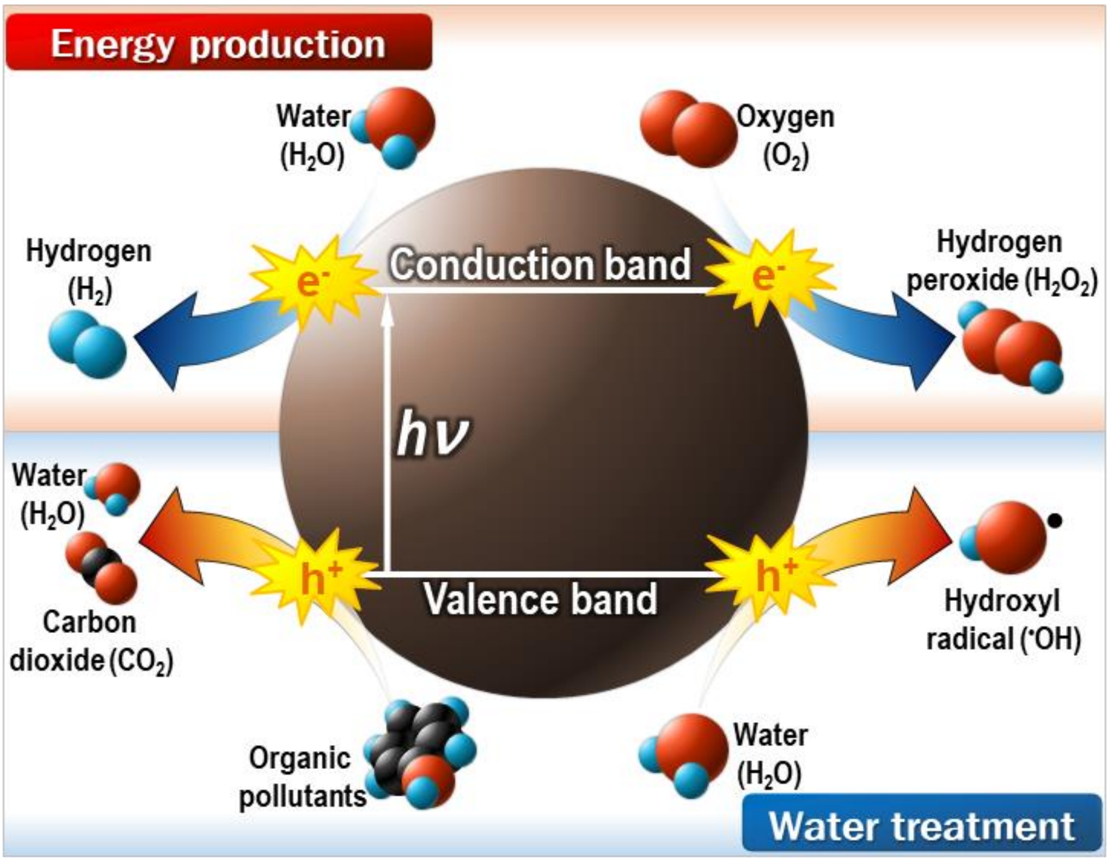
Energy production
Water
(H_2O)
Oxygen
(O_2)
Hydrogen
(H_2)
e^-
Conduction band
e^-
Hydrogen
peroxide (H_2O_2)
$h\nu$
Water
(H_2O)
Carbon
dioxide (CO_2)
h^+
Valence band
h^+
Hydroxyl
radical (•OH)
Organic
pollutants
Water
(H_2O)
Water treatment

Fig. 1.2. The general mechanism of photocatalytic reaction

The total light spectrum of sunlight is expressed in Fig. 1.3. Among the total light spectrum, visible light occupies the largest part of the total irradiance of sunlight. However, most of the traditional photocatalysts require UV-light energy to utilize the energy for degradation of organic compounds. The photocatalytic activity can be limited by the wide bandgap energy of photocatalyst, therefore, methods that could (1) compensate the wide bandgap energy and (2) utilize the huge amount of visible light energy efficiently have been intensively studied.

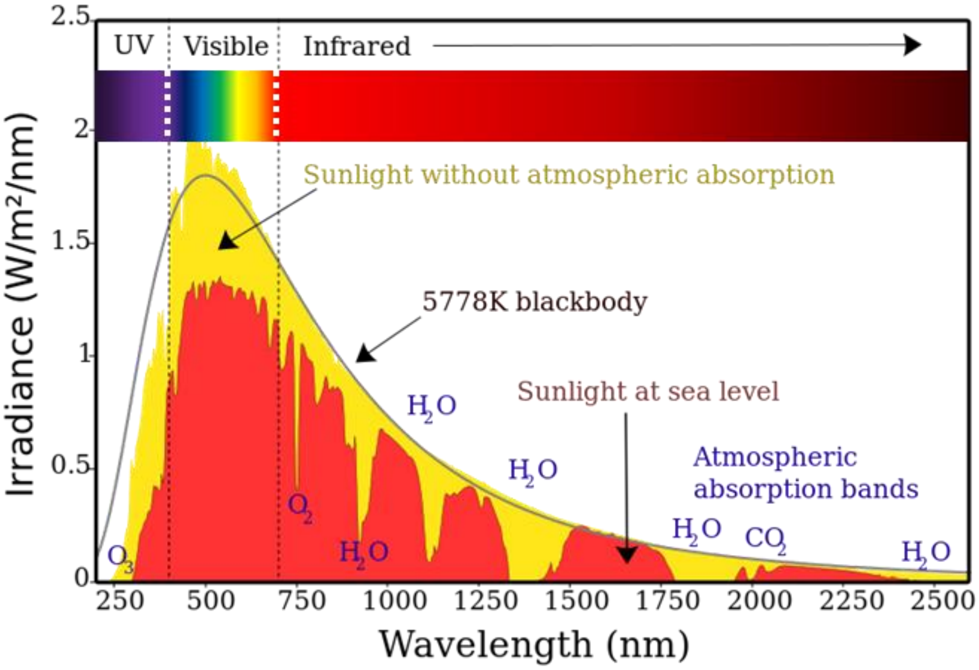

Fig. 1.3. Total irradiation spectrum of sunlight

II. Research trend of photocatalyst

1. Modification of photocatalysts

A variety approaches have been attempted to extend the range of light spectrum available for photocatalyst to the visible-light region by metal and non-metal doping, dye photosensitization, heterojunction, and ligand to metal charge transfer (LMCT) method etc..

Among those reported methods, metal and non-metal doping methods have widely studied due to a utilization of simple methods to increase visible light absorptivity effectively. Metal and nonmetal dopants generate mid-gap states between the valence band (VB) and the conduction band (CB) of TiO_2. Transition metals (Fe, Cu, Co, Ni, etc.) and noble metals (Pt, Au, Ag, etc.) have been typically used as metal dopants [25-27]. Metal-doping adjusts the bandgap of TiO_2 and promotes the interfacial electron transfer [28]. However, some metal dopants can act as recombination sites of electron-hole pairs, inhibiting the generation of reactive species on the TiO_2 surface [29,30].

Meanwhile, nonmetal-doping uses a different modification approach in which oxygen in the TiO_2 lattice is replaced by the doping element (C, N, and F etc.) [31-35]. Among the nonmetal dopants, sulfur have taken attention. Several reports examined that sulfur could insert in the TiO_2 lattice as a cationic or anionic state in accordance with the employed sulfur sources [36-40]. An anionic state of sulfur substitutes oxygen in the TiO_2 lattice and effectively decreases bandgap energy of TiO_2 [36-38], on the other hand, a cationic state of sulfur (S^{4+}) substitutes titanium in the TiO_2 lattice to change the bandgap energy [39,40].

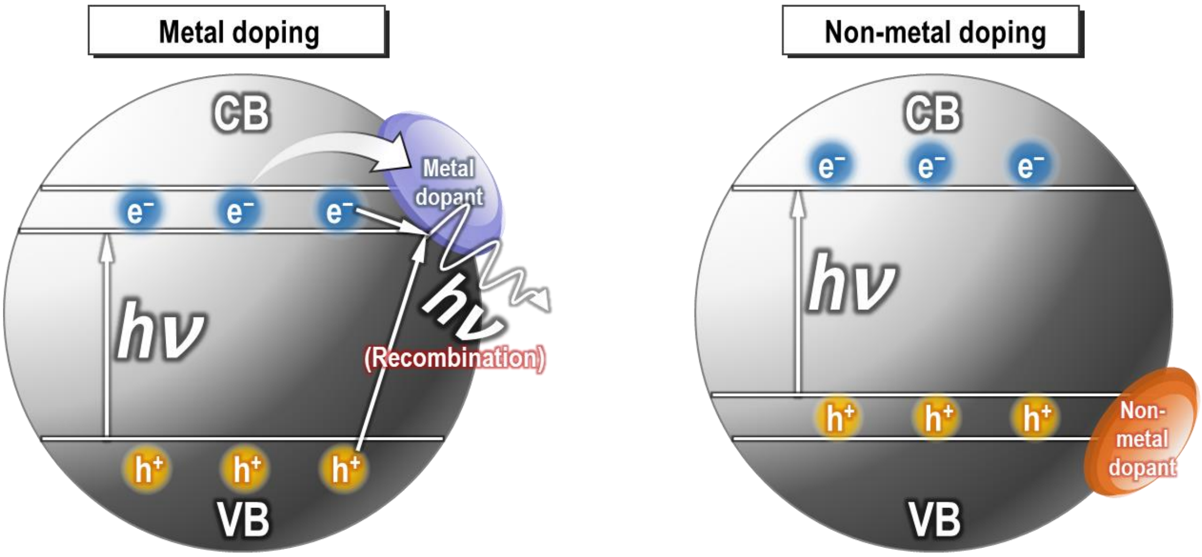

Fig. 1.4. Metal and non-metal doping in photocatalyst

Further, several studies have reported that the interaction of TiO_2 with hydrogen peroxide (H_2O_2) can generate visible light responsive photochemical activity [41-44]. The addition of H_2O_2 to the aqueous suspension of TiO_2 leads to the formation of peroxo-complexes on the TiO_2 surface [41,42,44]. It has been suggested that these peroxo-titania complexes are photoexcited by visible light, which can lead to the transfer of electrons, permitting the conduction band of TiO_2 that subsequently reduces adsorbed H_2O_2 to $^{\bullet}OH$ [41]. TiO_2 with externally supplied H_2O_2 has been found to degrade salicylic acid [41] and methylene blue [44], and oxidize 1-decene to an epoxide [42] under visible light illumination.

Although TiO_2 as a photocatalyst has been actively studied, the synthesis of peroxo-titania complexes as a stable solid material has been seldom reported and discussed. There have been a few cases where H_2O_2 was used to synthesize oxygen-rich TiO_2, which exhibited visible light responsive activity, causing the degradation of methylene blue [45] and the reduction of carbon dioxide [46]. Of significance, these oxygen-rich TiO_2 products did not have any peroxo-complexes on the surface (in the synthetic process, peroxo-titania complexes are formed as intermediates, but they disappear during calcination). Therefore, the photochemical activity and mechanisms observed to date are entirely different from those of peroxo-titania discussed here. One study has reported the synthesis of peroxo-titania and its use for methanol oxidation under visible light illumination [43]. However, the aforementioned study strikingly differs from this study due to the following: i) the synthetic conditions were harsher and more complicated (e.g., the use of ammonia and commercial TiO_2 powder, autoclaving step for 12 h, etc.); ii) the photochemical activity and mechanism of the material were different from ours (refer to the results and discussion parts for details); and iii) no interpretations were offered for the oxidation pathways of the organic compounds (i.e. the oxidation pathways were not elucidated).

2. Combination of photocatalytic system and other AOPs

The photocatalytic activity is usually limited by the wide bandgap energy of photocatalyst, however, fast hole and electron recombination and weak oxidizing power of photocatalysts also limit the application of photocatalyst in water treatment. Those limitations could be serious in some of the modified photocatalysts because the diminish of bandgap energy often reduces the oxidizing power and makes more chance to contact hole and electron pairs. To compensate the weak oxidizing power and fast hole-electron recombination, the injection of oxidant precursors (e.g., H_2O_2, IO_4^-, and $S_2O_8^{2-}$) and combination with AOPs (O_3 and Fenton) are attempted [47-50].

A combination with the Fenton(-like) reagent (Fe(III) and H_2O_2) increases the photocatalytic activity of TiO_2 for the degradation of organic compounds through (1) electron scavenging effect of Fe(III) and H_2O_2, which leads to improve charge separation, (2) additional production of $^{\bullet}OH$ by reductive conversion of H_2O_2, and (3) acceleration of Fenton(-like) reaction by photo-reduction of Fe(III) [51]. The combination of WO_3 and Fenton(-like) reagent also enhanced the photocatalytic degradation of organic compounds under visible light illumination, however, the reusability of the combined system decreased continuously [52].

3. Synthesis of visible light active photocatalyst

New types of visible light active photocatalyst have been actively developed and graphitic carbon nitride (g-C_3N_4) has raised attention recently. g-C_3N_4 is one of metal free photocatalysts that exhibit high stability and visible light absorptivity [53-57]. g-C_3N_4 also exhibits narrow bandgap energy (2.6–2.7 eV) that can easily utilize the visible light energy. Importantly, g-C_3N_4 could be easily synthesized by the thermal polymerization method using nitrogen-rich carbon precursors such as melamine [58-62], dicyandiamide [63-67], and urea [68-71] etc.. Such merits of g-C_3N_4, g-C_3N_4 has been applied in various photochemical activation part, especially in the photochemical production of H_2O_2.

Unlike the general metal oxide photocatalysts [72], g-C_3N_4 not only splits water by photocatalytic reaction (1.8 vs.RHE for valence band and −0.9 vs. RHE for conduction band) [73] but also exhibits the photochemical production of H_2O_2 with high selectivity by the sequential generation of a superoxide radical and 1,4-endoperoxide species [74,75]. To increase the H_2O_2 productivity using photochemical reaction of g-C_3N_4, several modification methods, such as attachment of noble metal and carbon materials, have been attempted [76-82]. However, the application of g-C_3N_4 in water treatment, especially the application of the photochemically generated H_2O_2 in water treatment, has not yet attempted.

III. Objective of the study

This study investigated visible light active photocatalytic system for degradation of organic pollutants under visible light illumination. The present research had the following two specific objectives:

1. To synthesize visible light response photocatalyst and assess the potential of the synthesized photocatalyst for degradation of organic compounds under visible light illumination.

For this purpose, amorphous peroxo-titania (Am-peroxo-TiO_2) was synthesized by a simple sol-gel method using H_2O_2 under mild condition (< 50°C and atmospheric pressure), and also prepared are its composites with platinum dopants. The prepared materials were characterized by different methods including TEM-EDS, XRD, XPS, and FT-IR. The degradation of various organic compounds by these materials was examined under visible light illumination, and the mechanism behind the visible light-response reactivity was elucidated.

2. To develop a combined system of visible light active photocatalyst (S-TiO_2) and Fenton-like system (Fe(III)/H_2O_2) for the degradation of organic compounds.

For this purpose, sulfur doped TiO_2 (S-TiO_2) was synthesized by a sol-gel method and the photocatalytic activity for oxidation of various organic compounds was examined under visible light illumination. The synthesized S-TiO_2 was characterized by different methods which include XRD, HRTEM-EDX, FT-IR, and XRF. The degradation of organic compounds by the combined system was examined under visible light illumination, and the mechanism of the combined system was elucidated.

3. To assess the combination of H_2O_2 producing photocatalyst (g-C_3N_4-AQ) and Fe(III) for the degradation of organic compounds.

For this purpose, anthraquinone anchored graphitic carbon nitride (g-C_3N_4-AQ) was synthesized by the sequential reaction of thermal polymerization and peptide bond formation. The synthesized g-C_3N_4-AQ was characterized by different methods which include XRD, DRS, FT-IR, and XPS. The combination of g-C_3N_4-AQ and Fe(III), which lead to the photochemically induced Fenton reaction, was assessed by the degradation of various organic compounds under visible light illumination. The effect of ROS scavengers and the oxidation of probe compounds was examined under visible light illumination. From the basis of the result, the photochemical mechanism of the combined system was elucidated.

CHAPTER 2. MATERIALS AND METHODS

I. Reagents

All chemicals were reagent grade and used without further purification. Chemicals used in this study included: titanium(IV) isopropoxide (TIP), H_2O_2, sulfuric acid, chloroplatinic acid (H_2PtCl_6), dicyandiamide, anthraquinone-2-carboxylic acid (AQ-COOH), nitric acid, sodium hydroxide, perchloric acid, phenol, 4–chlorophenol (4–CP), benzoic acid (BA), acetaminophen (AAP), carbamazepine (CBZ), methanol, tert–butanol, phosphoric acid, 1,10 phenanthroline, para–hydrobenzoic acid (*p*-HBA), coumarin, 7-hydroxycoumarin (7-HC), 2,3-bis(2-methyl-4-nitro-5-sulfophenyl)-2H-tetrazolium-5-carboxanilide (XTT), and 5,5-dimethyl-1-pyrroline N-oxide (DMPO) (all purchased from Sigma–Aldrich Co.). Other materials used were TiO_2 powder (P25, Degussa Co.) and acetonitrile (J.T. Baker Co.). All solutions were prepared in deionized (DI) water (18 MΩ·cm Milli–Q water, Millipore Co.). Stock solutions of phenol (10 mM), 4–CP (10 mM), BA (10 mM), AAP (1 mM), CBZ (0.1 mM), coumarin (1 mM), and XTT (1 mM) were prepared and stored at 4ºC until use.

II. Synthesis of photocatalysts

1. Amorphous peroxo-titania (Am-peroxo-TiO_2)

Am-peroxo-TiO_2 was synthesized by the sol–gel method. 2 mL TIP was mixed with 10 mL H_2O_2 solution (1 M), where the mixture was stirred for 1 h at room temperature (22 ± 2ºC). The resulting gel was collected by centrifugation at 3000 g for 15 min, and subsequently washed three times with DI water. Next, the gel was dried at 50ºC for 4 h to obtain the powdered sample. For the control test, the TiO_2 powder was synthesized by the same method in the absence of H_2O_2; all steps were identical, but DI water was used in place of the 1 M H_2O_2 solution.

Platinized Am-peroxo-TiO_2 (Pt-Am-peroxo-TiO_2) was synthesized as follows. 1.25 mL TIP and 25 mL ethanol were added to a 250 mL acidic solution (pH 1.5 maintained with nitric acid), containing 1 M H_2O_2 and 0.08 mM H_2PtCl_6, and stirred overnight. The resulting gel was evaporated at 50ºC. The final powder product was washed with DI water and dried at 50ºC for 4 h.

2. Sulfur doped TiO_2 (S-TiO_2)

S-TiO_2 was synthesized by the sol–gel method. 2.97 mL of TIP was added into 22 mL of sulfuric acid solution (3.21 M). The mixture was stirred for 2 h and all the solvents were evaporated at 350ºC for 6 h. The resulting solid was ground to powder in an alumina mortar. Next, the ground powder was heated to 850ºC at a rate of 5ºC/min and then the temperature maintained at 850ºC for 2 h. Finally, the synthesized TiO_2 was washed with DI water and dried at 50ºC.

3. Anthraquinone anchored graphitic carbon nitride (g-C_3N_4-AQ)

The synthesis of g-C_3N_4-AQ, reported in Kim et al. (2018) [81], was divided into 2 steps: the synthesis of g-C_3N_4 and the formation of peptide bonds between AQ-COOH and g-C_3N_4. First, g-C_3N_4 was synthesized through thermal polymerization of dicyandiamide. In detail, 5 g of dicyandiamide was heated to 520°C at a rate of 2.3°C/min and then heated at 520°C for 4 h. The collected solid was ground to powder in an alumina mortar. Next, the prepared g-C_3N_4 (0.4 g) powder and AQ-COOH (0.04 g) was added into acetonitrile (36 mL). The suspension was sonicated for 30 min and the formation of peptide bonds was performed with stirring for 12 h at 50°C. g-C_3N_4-AQ was collected by filtration and subsequently washed with DI water.

III. Characterization

X–ray diffraction patterns of the synthesized materials were recorded using an X-ray diffractometer (D8 ADVANCE, Bruker AXS Inc.) with Cu–Kα radiation. Morphology and surface elemental distribution were analyzed with a high–resolution transmission electron microscope, coupled with an energy dispersive X-ray spectrometer (HRTEM/EDX) at 200 kV (JEM–2100F, Jeol Co.). X–ray photoelectron spectroscopy (XPS) with monochromatic Al–Kα radiation (K–alpha, Thermo Fisher Scientific Inc.) and Fourier transform infrared (FT–IR) spectroscopy (Nicolet 6700, Thermo Fisher Scientific Inc.) were used to examine the surface compositions and functional groups of the powdered products. A UV/vis/near IR spectrophotometer (Cary 5000, Agilent Co.) was used to obtain the diffuse reflectance spectra. Specific surface area (SSA) of the powder was determined by the 5 point Brunauer–Emmett–Teller (BET) method using N_2 physisorption measurements on an ASAP 2420 Accelerated Surface Area and Porosimetry system (Micromeritics Co.).

IV. Photochemical experiments

All experiments were performed in a quartz batch reactor at room temperature (22 ± 2ºC). For the photochemical experiments of Am-peroxo-TiO_2 and S-TiO_2, light illumination was performed using fluorescent lamps (six 4 W lamps; Shin–Kwang electronics Co.) with a 400 nm longpass filter in a dark chamber. For the experiments of g-C_3N_4-AQ, illumination was performed by a 150 W xenon arc lamp (LS 150, Abet Technologies, Inc.) equipped with an AM 1.5G filter and a 400 nm longpass filter; the light intensity with AM 1.5G filter was adjusted to one–sun condition (100 mW/cm^2). Light emission spectra of the fluorescent lamp and the xenon arc lamp were recorded by a spectroradiometer (SPR-4001, Luzchem Research Inc.) (Fig. 2.1).

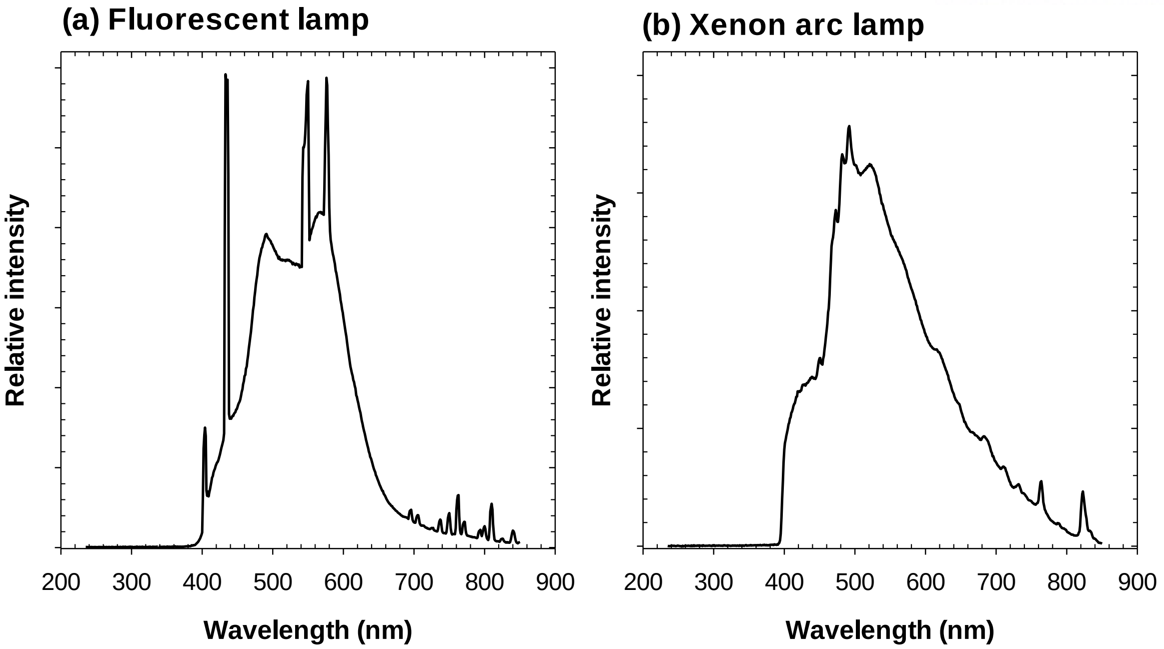

Fig. 2.1. Light emission spectra of the fluorescent lamp (a) and the xenon arc lamp (b) with a 400 nm longpass filter.

The reaction solution (50 mL) was prepared by adding the photocatalyst powder (0.5 g/L) and the target organic compound (10 μM). Initial pH of the solution was adjusted at 5.0 for the experiment of Am-peroxo-TiO_2 and 3.0 for the experiments of S-TiO_2 and g-C_3N_4-AQ. pH variations during the experiments were maintained at less than 0.2 units. Initiation of the reaction occurred upon light illumination. The incident photon, which flowed into the reaction solution were 6.43×10^{-6} Einstein/L·s (fluorescent lamp) and 2.46×10^{-5} Einstein/L·s (xenon arc lamp), were measured by chemical actinometry using the potassium Reinecke's salt (400~650 nm).[#] The abovementioned values were converted to 1.45 mW/cm^3 and 5.61 mW/cm^3, respectively, where the calculation was derived from the respective light emission profiles shown in Fig. 2.1. During the photochemical reaction, samples (1 mL) were withdrawn at predetermined time intervals, and immediately filtered using a 0.45 μm PTFE syringe filter (Advantech Co.). All experiments were performed in triplicates, at a minimum. Average values and standard deviations (error bars) have been presented.

V. Analytical methods

The concentrations of the organic compounds were measured by high performance liquid chromatography (HPLC, UltiMate^{TM} 3000, Dionex Co.) with UV absorbance detection (at 277, 230, 227, 241, 285, 270, and 320 nm for phenol, 4–CP, BA, AAP, CBZ, *p*–HBA, and 7–HC, respectively). Separation was performed on a 150 mm × 4.6 mm, 5 μm C18 column (ZORBAX Eclipse XDB–C18, Agilent Co.). A mixture of phosphoric acid solution (0.1%v/v), acetonitrile, and methanol was used as the mobile phase at a flow rate of 1 mL/min. Chloride ion was measured by ion chromatography (ICS 2100, Dionex Co.) equipped with a conductivity detector. Separation was performed on a Dionex IonPac As-16 column using 22 mM potassium hydroxide solution as the mobile phase at a flow rate of 1 mL/min. The concentration of total organic carbon (TOC) was determined by TOC analyser (TOC-V/CPH, Shimadzu Co.).

The degradation products of 4-CP were analyzed by the rapid separation liquid chromatography (RSLC) (UltiMate 3000, Dionex Co.) system coupled with a quadrupole-Orbitrap mass spectrometer (Q Exactive™, Thermo Fisher Scientific Inc.) (LC/MS). Chromatographic separation was performed on a 2.1 × 150 mm, 5 μm C18 column (Acclaim^{TM} 120 C18, Thermo Fisher Scientific Inc.), using 0.1% (v/v) formic acid solution and acetonitrile as the eluent with a 65:35 ratio at a flow rate of 0.3 mL/min. The heated electrospray ionization source interface was operated in the negative ionization mode under the following conditions: spray voltage = 3.1 kV, sheath gas = 40 arbitrary units, auxiliary gas = 10 arbitrary units, sweep gas = 0 arbitrary units, capillary temperature = 320˚C, S-lens RF level = 65.0 arbitrary units and vaporizer temperature = 300˚C. Mass spectra were obtained in full scanning mode from 50 to 230 m/z at a resolution of 35000, an automatic gain control target value of 5×10^4, and a maximum injection time of 100 ms. All data acquisition and its processing were performed using Xcalibur 3.0.2 software (Thermo Fisher Scientific Inc.).

Photocurrents were measured of the aqueous suspensions of Am-peroxo-TiO_2 and Pt-Am-peroxo-TiO_2 containing 1 mM Fe(III) as an electron shuttle and 0.1 M $NaClO_4$ as an electrolyte under visible light conditions (xenon arc lamp) [20]. A three-electrode cell with platinum plates (2.5 cm x 1.5 cm), serving as working and counter electrodes, and a saturated calomel electrode (SCE) as a reference electrode, were used. Currents were recorded using a potentiostat (VSP, Bio-Logic Science Instruments) with the chronoamperometry mode on a working electrode biased at +0.7 V (vs. SCE).

An electron paramagnetic resonance (EPR) spectroscopy (JES-X310, Jeol Co.), using 10 mM DMPO as a spin-trapping agent, was used to detect ROS. Samples were collected from the photochemical reactor, and transferred into a quartz flat cell for the EPR analysis. EPR signals of the DMPO-radical adducts were scanned under the following conditions: microwave frequency at 9.42 GHz, microwave power at 1.00 mW, modulation frequency at 100 kHz, and modulation amplitude at 2.0 G.

CHAPTER 3. RESULTS AND DISCUSSION

I. Amorphous peroxo-titania (Am-peroxo-TiO_2)

1. Results

1.1. Synthesis and characterization of Am-peroxo-TiO_2

In preliminary experiments, different varieties of Am-peroxo-TiO_2 were synthesized using varying concentrations of H_2O_2 (for the sol-gel process) and the drying temperature, and then their photochemical activity to degrade 4-CP were examined under visible-light illumination (Fig. 3.1.1). The yellow color of the powdered substance intensified with increasing concentrations of the H_2O_2 utilized in the synthetic process (Fig. 3.1.1a). Importantly, the degradation rate of 4-CP was optimized when 1 M H_2O_2 was used to synthesize the powdered precipitate (Figs. 3.1.1b and c). Interestingly, the yellow color of the material faded with increasing temperatures (Fig. 3.1.1d) during the drying process, and correspondingly the degradation rate of 4-CP drastically decreased when dried at temperatures higher than 100ºC (Figs. 3.1.1e and f). Based on these results, the synthetic conditions of Am-peroxo-TiO_2 for photochemical experiments were selected, where 1 M of H_2O_2 (the concentration of H_2O_2 used in the sol-gel process) and 50ºC (the drying temperature) were used for the present study.

(a) Photographs (H_2O_2)

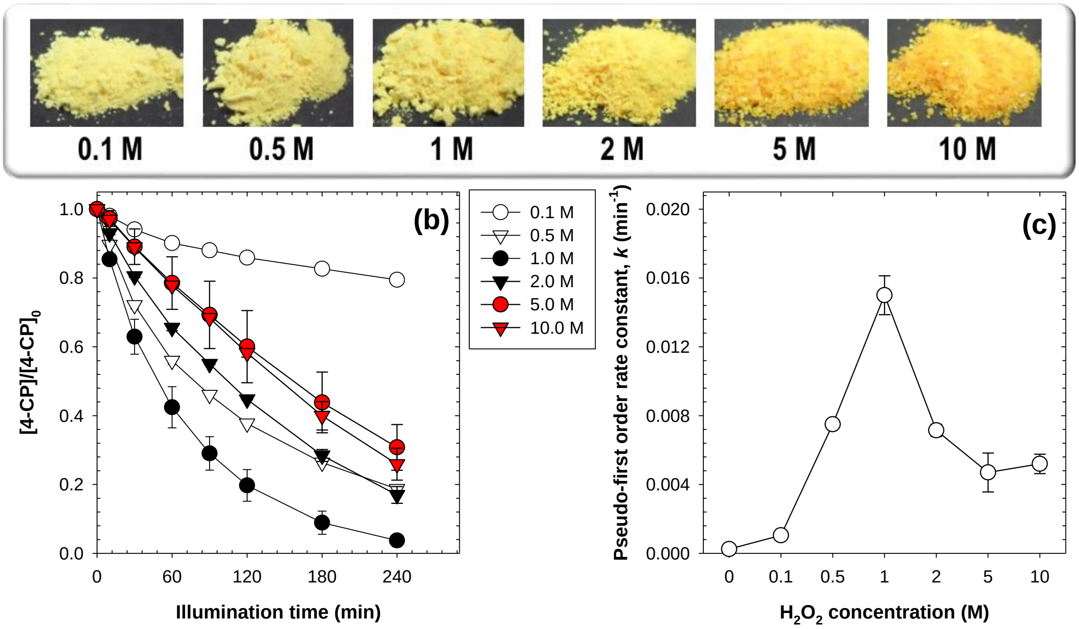

(d) Photographs (Drying Temp.)

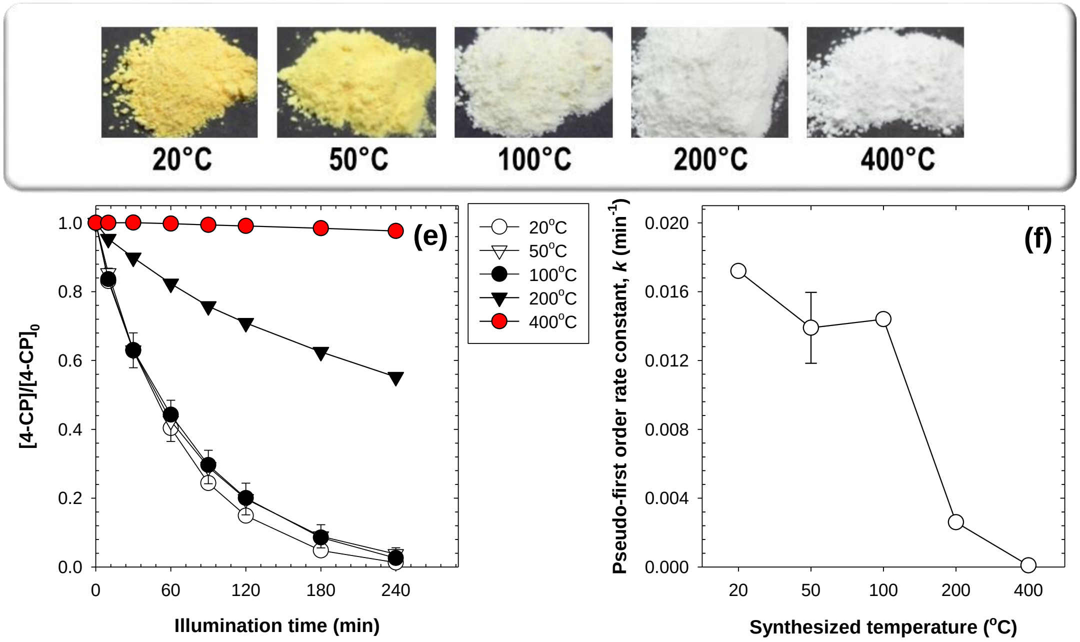

Fig. 3.1.1. Photographs of Am-peroxo-TiO_2 synthesized with varying H_2O_2 concentrations and drying temperature, and photochemical degradation of 4-CP using synthesized materials under visible light illumination (time-concentration profiles and pseudo first-order rate constants): effects of H_2O_2 concentration ((a) – (c)) and drying temperature ((d) – (f)) ([Am-peroxo-TiO_2] = 0.5 g/L, $[4\text{-CP}]_0 = 10$ μM, pH = 5, I = 6.43×10^{-6} Einstein/L·s (fluorescent lamp, λ > 400 nm).

The Am-peroxo-TiO_2 material product was a yellow powdered precipitate, with a diffuse reflectance spectrum of visible light absorption of up to 600 nm (Fig. 3.1.2a). XRD patterns of Am-peroxo-TiO_2 recorded mostly amorphous phases with poor crystallinity; and Am-peroxo-TiO_2 exhibited very weak and broad anatase peaks (Fig. 3.1.2b). Calcination of Am-peroxo-TiO_2 at elevated temperatures can enhance the anatase phase (Fig. 3.1.2b) with crystal particle growth through the sintering process (Fig. 3.1.2b). However, as shown in Fig. 3.1.1, heat treatment appears to destroy any surface peroxo complexes of Am-peroxo-TiO_2, thereby eliminating its photochemical activity. HRTEM images indicated that Am-peroxo-TiO_2 forms aggregates of small nanoparticles (ca < 10 nm) (Fig. 3.1.3b). The specific surface area of Am-peroxo-TiO_2 was determined to be 267.89 m^2/g, which is approximately 5-fold greater than that of commercial TiO_2 (Degussa P25, average particle size is 25 nm; specific surface area is 52.68 m^2/g). Additionally, HRTEM-EDX analysis indicates that Am-peroxo-TiO_2 has a high atomic oxygen to titanium ratio (O:Ti = 46.1:53.9), possibly due to the presence of its surface peroxo groups (Fig. 3.1.3c); the O:Ti atomic ratio of P25 has been measured to be at 33.1:66.9.

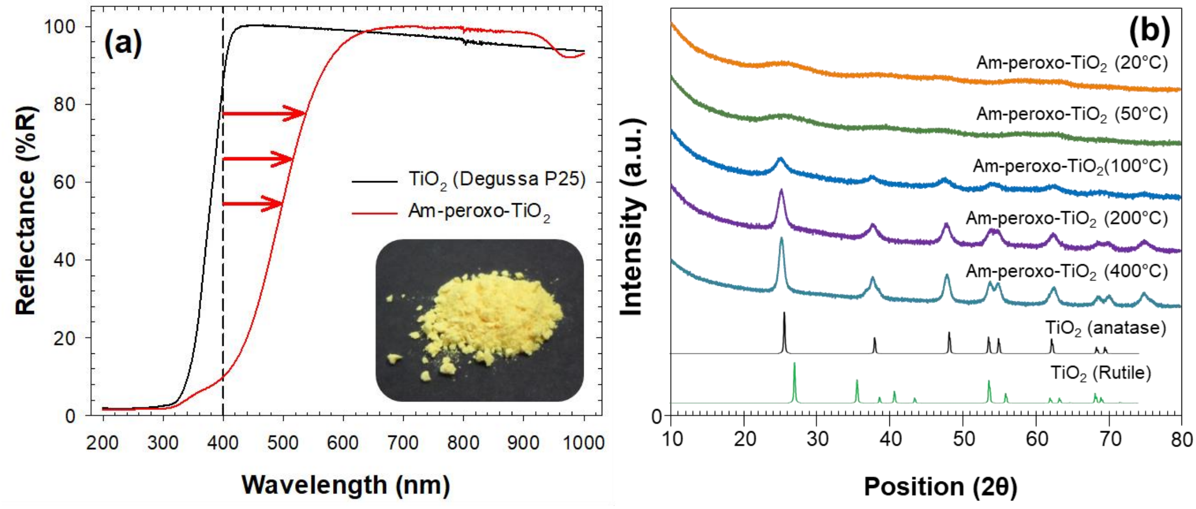

Fig. 3.1.2. Diffuse reflectance spectra of Am-peroxo-TiO_2 (a) and X–ray diffraction patterns of Am-peroxo-TiO_2 prepared at different drying temperature (b).

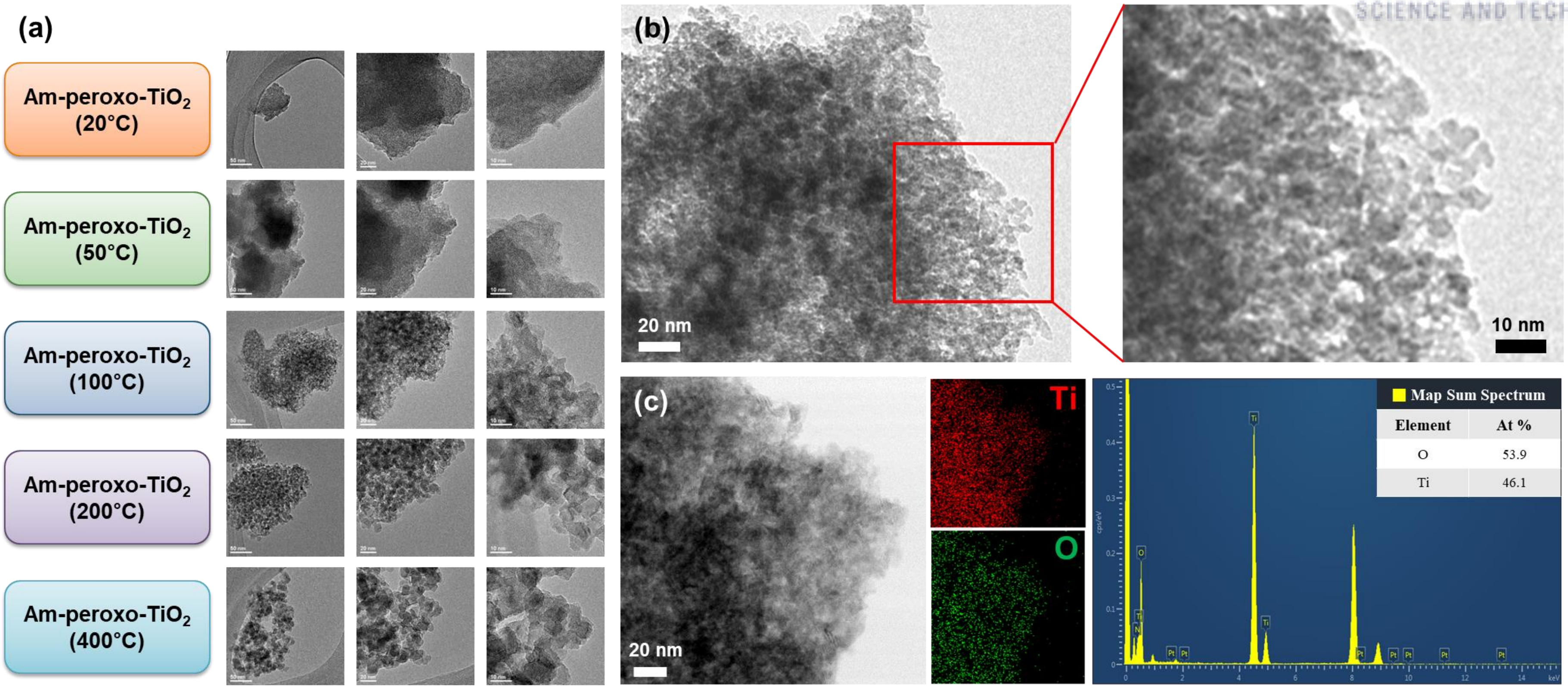
(a)
Am-peroxo-TiO2 (20°C)
Am-peroxo-TiO2 (50°C)
Am-peroxo-TiO2 (100°C)
Am-peroxo-TiO2 (200°C)
Am-peroxo-TiO2 (400°C)
(b)
20 nm
10 nm
(c)
20 nm
Ti
O
Map Sum Spectrum
Element
At %
O
53.9
Ti
46.1
keV

Fig. 3.1.3. HR-TEM images of Am-peroxo-TiO$_2$ prepared at different drying temperature (a), HR-TEM image (b), and EDX spectra of Am-peroxo-TiO$_2$ (50°C).

The O 1s XPS spectrum of Am-peroxo-TiO_2 revealed three bands (Fig. 3.1.4a). The bands at 529.8 and 531.8 eV represent the lattice oxygen (Ti4+–O) and the hydroxide oxygen (Ti4+–OH), respectively [42,83]. The band at 533 eV correlates to the peroxo complexes, Ti4+–OOH [83]. However, the XPS spectrum of P25 did not reveal a band corresponding to the peroxo complex, and only displayed a small hydroxide band relative to that of Am-peroxo-TiO_2 (Fig. 3.1.4c). In addition, the FT-IR spectrum registered absorbance bands reflecting the surface peroxo groups in the range of 950–700 cm^{-1}, resulting from the stretching vibrations of the –O–O– bonds [42,84]. The Ti-peroxo groups are known to have two different species (i.e., Ti–η^2–peroxide (932–800 cm^{-1}) and Ti–μ–peroxide (770–700 cm^{-1})) [42,84]. The FT–IR spectrum of Am-peroxo-TiO_2 displayed an absorption band centered at 900 cm^{-1} that was attributable to Ti–η^2–peroxide (Fig. 3.1.4b), on the other hand, the FT–IR spectrum of P25 did not reveal any of the Ti-peroxo-groups (Fig. 3.1.4d).

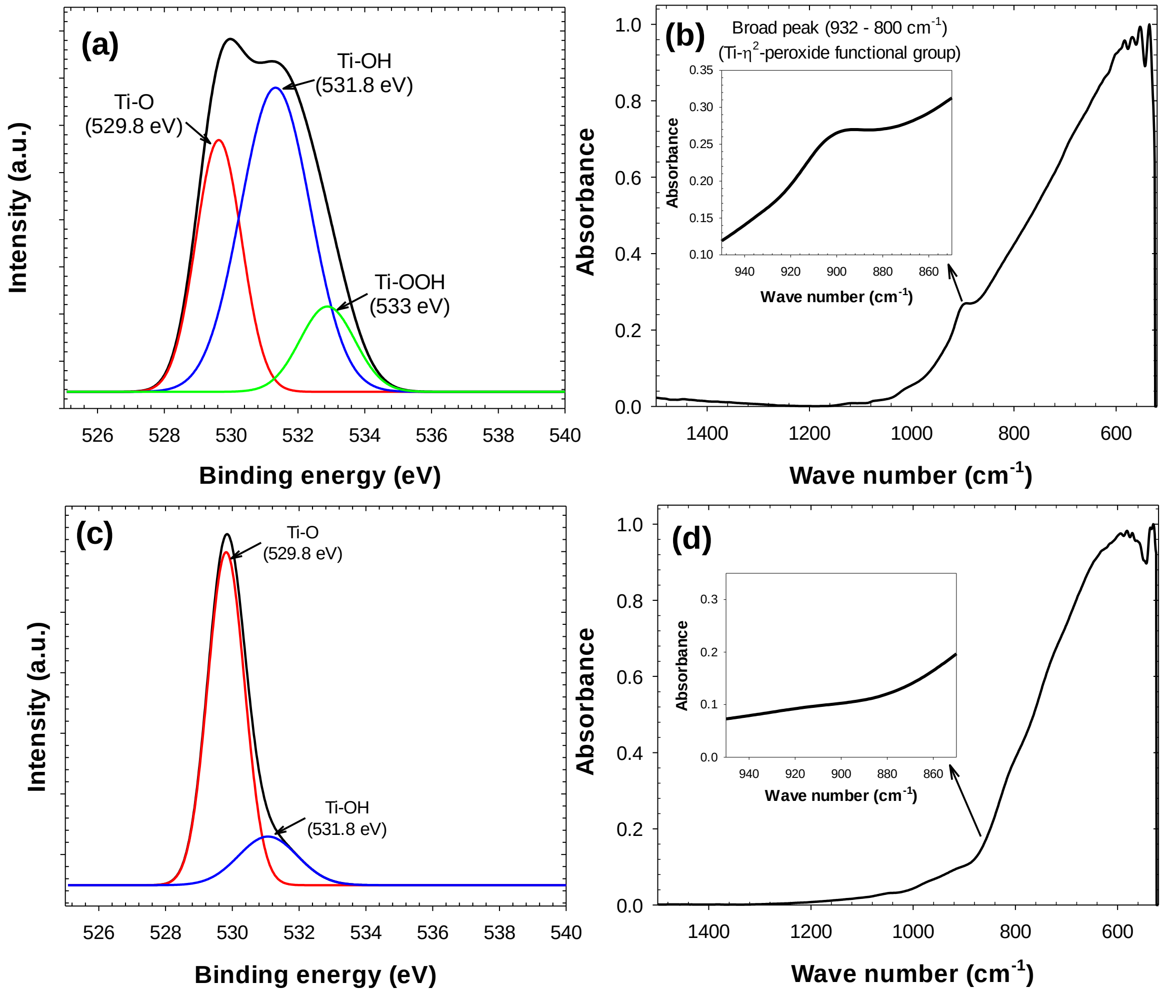

Fig. 3.1.4. X–ray photoelectron spectra (O 1s level) and FT-IR spectra of Am-peroxo-TiO_2 ((a) and (b)), and TiO_2 (Degussa P25) ((c) and (d)).

1.2. Photochemical degradation of organic compounds

Degradation of 4-CP by Am-peroxo-TiO_2 and the respective control materials (synthesized TiO_2 and Degussa P25) were examined under visible light (Fig. 3.1.5a). Synthesized TiO_2 did not degrade 4–CP for the full reaction time of 4 h. Also, P25 demonstrated a poor ability to degrade 4-CP (24% degradation in 4 h), likely owing to the ligand-to-metal charge transfer (LMCT) pathway [85]. In contrast, Am-peroxo-TiO_2 can completely degrade 4-CP in 4 h. Measurements of chloride ion during the degradation of 4-CP indicates that approximately 66% of 4-CP degradation products were dechlorinated. Degradation of 4–CP with the xenon arc lamp system was 3.5-fold faster ($k_{4\text{-CP}}$ = 2.91 h^{-1}) than with the fluorescent lamp system ($k_{4\text{-CP}}$ = 0.83 h^{-1}) (Fig. 3.1.5b), which can be reasonably explained by the difference in incident photon flows of the two systems (there was an approximately 3.8-fold difference, refer to CHAPTER 2-IV for the values). When the concentration of 4-CP was increased up to 0.1 mM, Am-peroxo-TiO_2 could degrade 41% of 4-CP in 4 h under visible light illumination and approximately 50% of the degraded 4-CP was mineralized (Fig. 3.1.6).

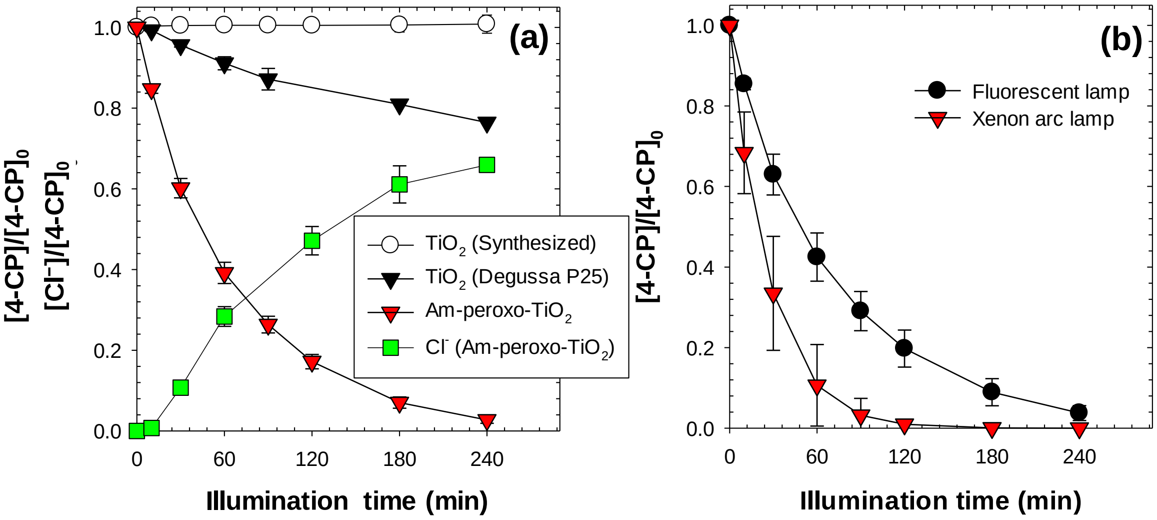

Fig. 3.1.5. Degradation of 4-CP by Am-peroxo-TiO_2 under visible-light illumination: comparison with control TiO_2 photocatalysts and dechlorination of 4-CP by Am-peroxo-TiO_2 (a) comparison of different light sources (b) ([Am-peroxo-TiO_2] = 0.5 g/L, $[4\text{-CP}]_0$ = 10 μM, pH = 5, I = 6.43 × 10^{-6} Einstein/L·s (fluorescent lamp, λ > 400 nm), $[TiO_2]_0$ = 0.5 g/L for (a), I = 2.46 × 10^{-5} Einstein/L·s (xenon arc lamp, λ > 400 nm) for (b)).

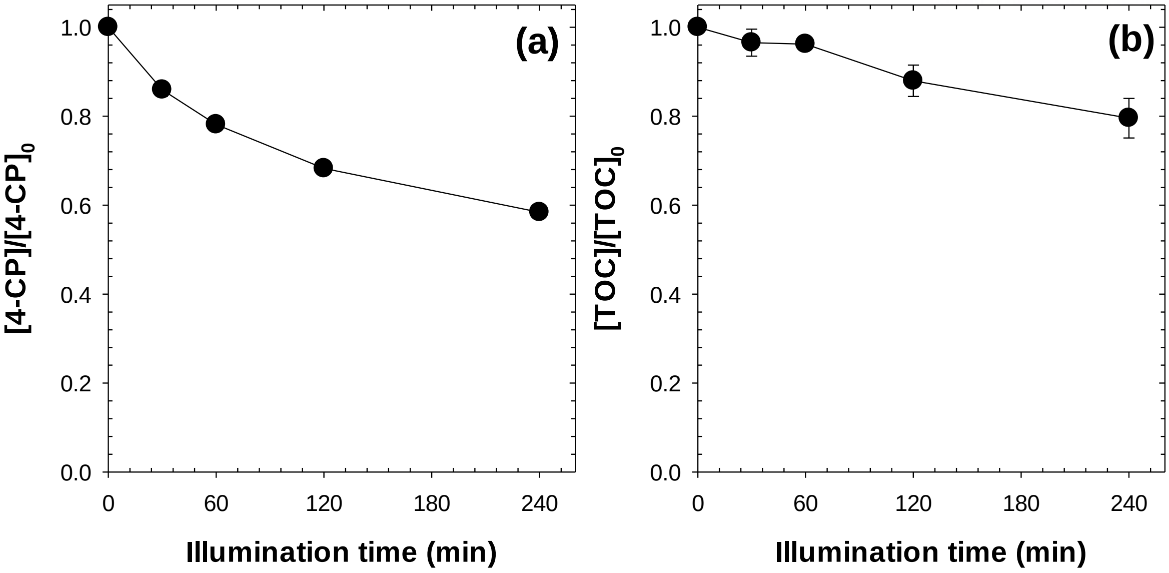

Fig. 3.1.6. Degradation of 4-CP (a) and TOC removal (b) by Am-peroxo-TiO_2 under visible light illumination ([Am-peroxo-TiO_2] = 0.5 g/L, $[4\text{-CP}]_0$ = 0.1 mM, pH = 5, I = 6.43 × 10^{-6} Einstein/L·s (fluorescent lamp, λ > 400 nm)).

Photochemical degradation of different organic compounds (phenol, 4–CP, BA, AAP, and CBZ) was examined in illuminated Am-peroxo-TiO_2 suspension (Fig. 3.1.7). The degradation rate of AAP was the greatest (complete degradation in 1 h, $k_{\text{AAP}} = 5.15\ \text{h}^{-1}$), which was followed by those of 4-CP and phenol ($k_{\text{4-CP}} = 0.83\ \text{h}^{-1}$ and $k_{\text{Phenol}} = 0.57\ \text{h}^{-1}$). However, BA and CBZ hardly degraded.

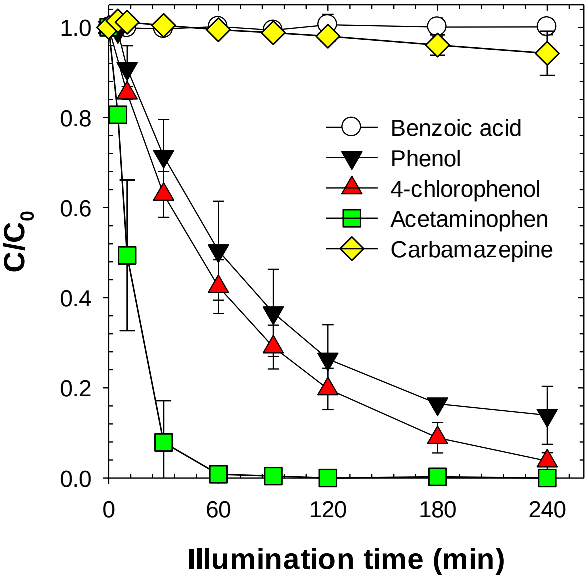

Fig. 3.1.7. Degradation of organic compounds by Am-peroxo-TiO_2 under visible light illumination ([Am-peroxo-TiO_2] = 0.5 g/L, $[4\text{-CP}]_0 = [\text{Phenol}]_0 = [\text{BA}]_0 = [\text{AAP}]_0 = [\text{CBZ}]_0$ = 10 μM, pH = 5, I = 6.43 × 10^{-6} Einstein/L·s (fluorescent lamp, λ > 400 nm)).

The effect of $^•OH$ scavengers on the photochemical degradation of 4-CP was also examined (Fig. 3.1.8a); methanol and *tert*–butanol were used as the respective $^•OH$ scavengers. It is believed that *tert*–butanol mainly scavenges free $^•OH$ in the bulk phase, but methanol can scavenge both free and surface-bound $^•OHs$ [86]. As shown in Fig. 3.1.8a, the addition of methanol and *tert*–butanol did not significantly affect the degradation rate of 4-CP by illuminated Am-peroxo-TiO_2.

To examine the effects of dissolved oxygen, photochemical degradation 4-CP by illuminated Am-peroxo-TiO_2 was monitored under deaerated conditions (N_2 sparging), and compared with air-saturated conditions (open to the atmosphere) (Fig. 3.1.8b). Degradation of 4-CP was not significantly affected by deaeration, (only a marginal inhibition was observed), indicating that dissolved oxygen does not play an important role in the photochemical activity of Am-peroxo-TiO_2. This observation is inconsistent with an earlier study where TiO_2 photocatalysis in the presence of dissolved oxygen accelerated the degradation of organic compounds [87]. Specifically, oxygen captures electrons from the conduction band of TiO_2 (E_{CB} = –0.51 V_{NHE} at pH 7) to form $O_2^{•-}$ ($E^0[O_2/O_2^{•-}] = -0.33$ V) [88]. This electron trapping, in turn, is believed to inhibit the electron-hole recombination on the illuminated TiO_2 surface, causing an increase in the steady-state concentration of oxidizing species in the valence band, which are ultimately responsible for degrading organic compounds.

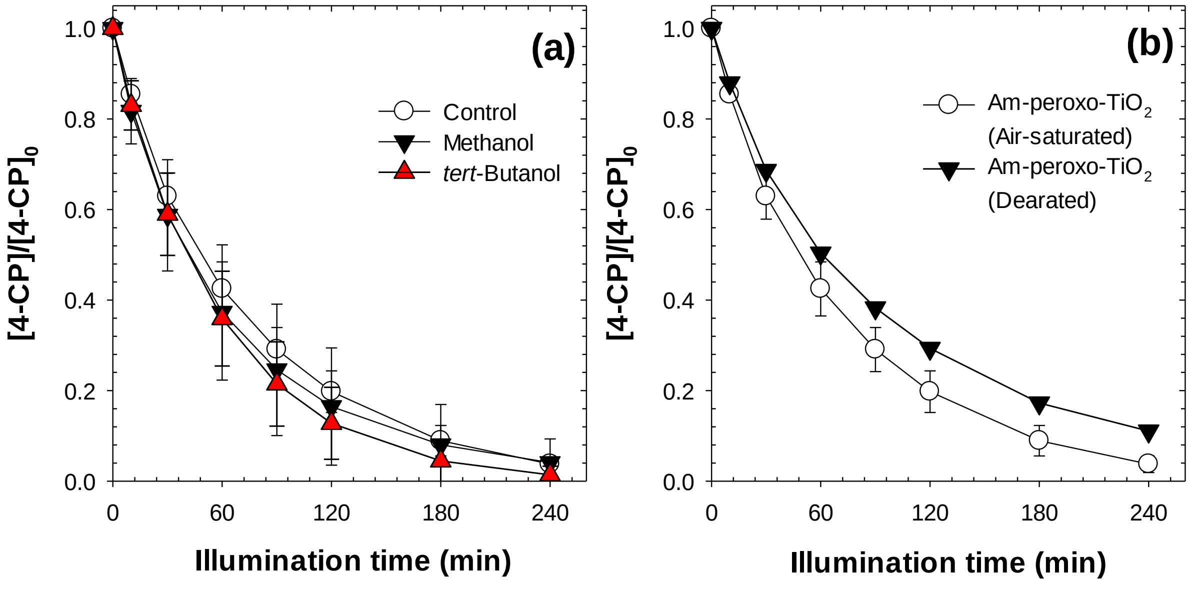

Fig. 3.1.8. Degradation of 4-CP by Am-peroxo-TiO_2 under visible light illumination: effects of ROS scavengers (a), and dissolved oxygen (b) ([Am-peroxo-TiO_2] = 0.5 g/L, $[4\text{-CP}]_0$ = 10 μM, pH = 5, I = 6.43 × 10^{-6} Einstein/L·s (fluorescent lamp, λ > 400 nm), $[\text{Methanol}]_0$ = $[\textit{tert}\text{-Butanol}]_0$ = 200 mM for (a)).

XTT (2,3-bis(2-methyl-4-nitro-5-sulfophenyl)-2H-tetrazolium-5-carboxanilide) was used as a probe for $O_2^{•-}$. $O_2^{•-}$ is known to reduce XTT to form XTT-formazan, which correspondingly displays a strong visible-light absorption band at 470 nm [89]. However, testing with XTT failed to detect any $O_2^{\bullet-}$ (Fig. 3.1.9). In addition, EPR analysis also failed to detect DMPO spin adducts of $^{\bullet}OH$ and $O_2^{\bullet-}$ (data not shown).

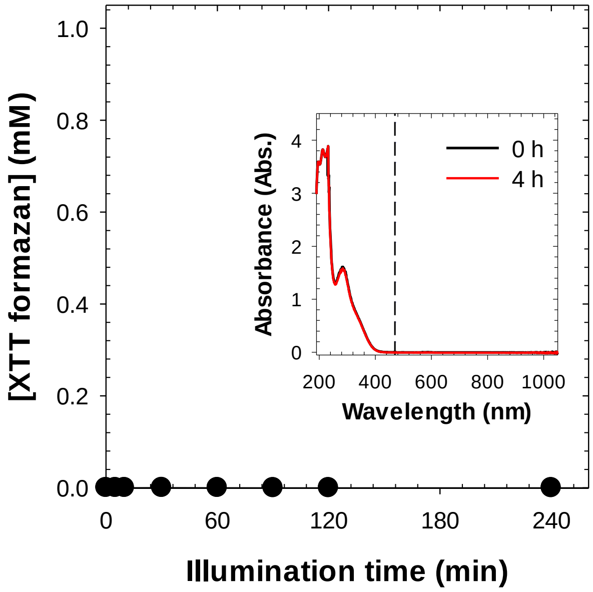

Fig. 3.1.9. Formation of XTT-formazan by Am-peroxo-TiO_2 under visible light illumination ([Am-peroxo-TiO_2] = 0.5 g/L, $[XTT]_0$ = 0.1 mM, pH = 5, I = 6.43 × 10^{-6} Einstein/L·s (fluorescent lamp, $\lambda >$ 400 nm)).

1.3. Photostability of Am-peroxo-TiO_2

To evaluate the stability of Am-peroxo-TiO_2, repeated degradation of 4-CP in illuminated Am-peroxo-TiO_2 suspension was performed. Briefly, Am-peroxo-TiO_2 was added once at the beginning of the reaction, and 4–CP (1 μM) was injected every 2 h (Fig. 3.1.10a). The degradation efficiency of 4-CP decreased slightly over four cycles (open circles in Fig. 3.1.10a). Additionally, the Am-peroxo-TiO_2 suspension was pre-illuminated for 12 h in the absence of 4-CP, and then repeated degradation with 4-CP was tested in the same manner (filled circles in Fig. 3.1.10a). The trends of 4-CP degradation of Am-peroxo-TiO_2 under pre-illuminated conditions almost synchronized with those of material that hadn’t been pre-irradiated (compare open and filled circles in Fig. 3.1.10a), indicating that light illumination in the absence of an organic compound does not decrease the photochemical activity of Am-peroxo-TiO_2.

Repeated photocatalytic degradation was carried out with 4-CP, as previously described, with increasing concentrations of 4-CP (10 μM) as input (open circles in Fig. 3.1.10b). The degradation efficiency of 4-CP substantially decreased over the four cycles (99%, 65%, 35%, and 27% at each cycle). Note that the decrease in degradation efficiency with 1 μM 4-CP was minor (Fig. 3.1.10a).

The decrease in 4-CP degradation efficiency is likely attributable to interference by accumulated oxidation products in the solution and on the material surface. To test this assumption, the used Am-peroxo-TiO_2 material was collected after four cycles of 4-CP degradation, rinsed with DI water three times, and resuspended in a new solution for another four-cycle repetition test (Fig. 3.1.11). The degradation efficiency recovered from 27% to 65%, upon washing and resuspension, confirming that the oxidation byproducts partially contribute to the efficiency loss. Of note, in the second round of the repetition test, the 4-CP degradation efficiency decreased more rapidly. Strikingly, the yellow color of the material faded after the first repetition test. These observations collectively imply that surface peroxo-complexes of Am-peroxo-TiO_2 are unstable under visible light in the presence of specific organic compounds. In contrast, Pt-Am-peroxo-TiO_2 exhibited greater photostability than Am-peroxo-TiO_2 in the repetition test (filled circles in Fig. 3.1.10b); illuminated Pt-Am-peroxo-TiO_2 generated a higher photocurrent (Fig. 3.1.12).

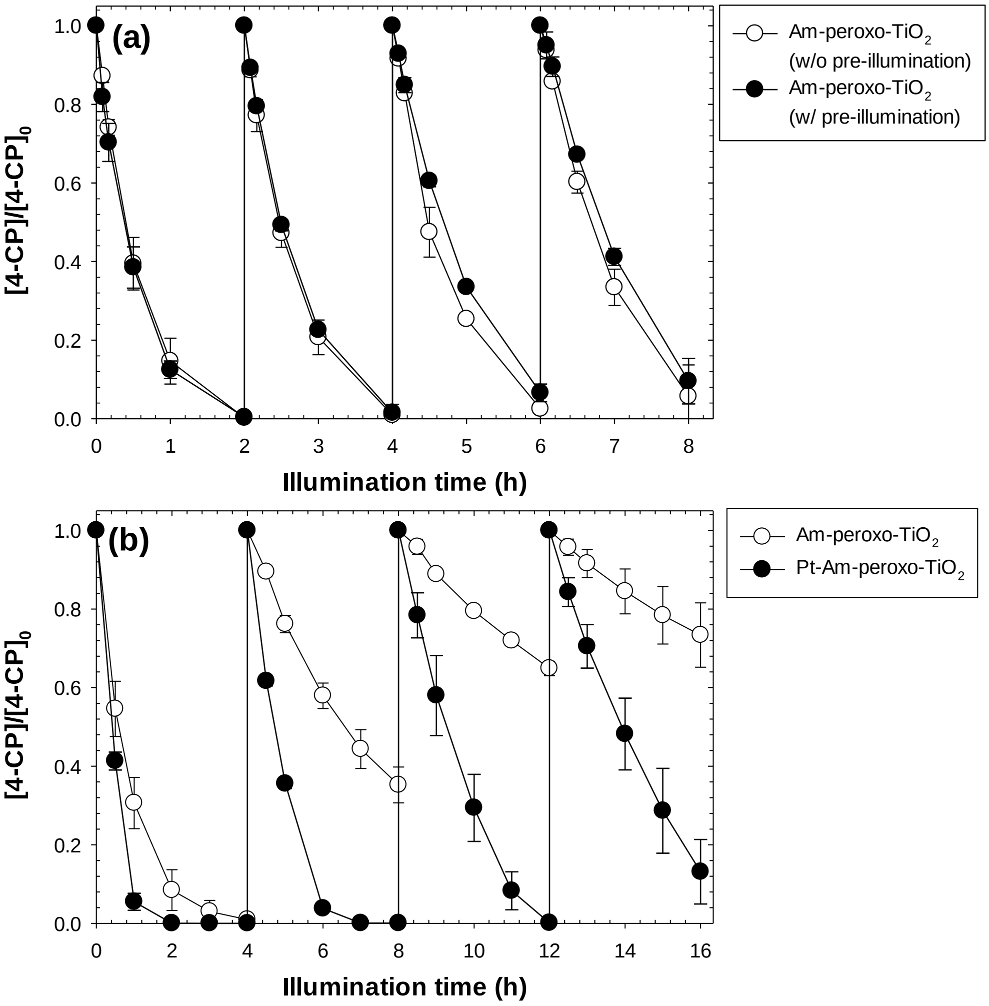

Fig. 3.1.10. Repeated degradation of 4-CP by Am-peroxo-TiO_2 (and Pt-Am-peroxo-TiO_2) under visible light irradiation: effect of pre-illumination (a) and comparison with Pt-Am-peroxo-TiO_2 (b) ([Am-peroxo-TiO_2] = 0.5 g/L, pH = 5, I = 6.43×10^{-6} Einstein/L·s (fluorescent lamp, $\lambda > 400$ nm), $[4\text{-CP}]_0 = 1\ \mu M$ for (a), $[\text{Pt-Am-peroxo-TiO}_2]_0 = 0.5$ g/L and $[4\text{–CP}]_0 = 10\ \mu M$ for (b)).

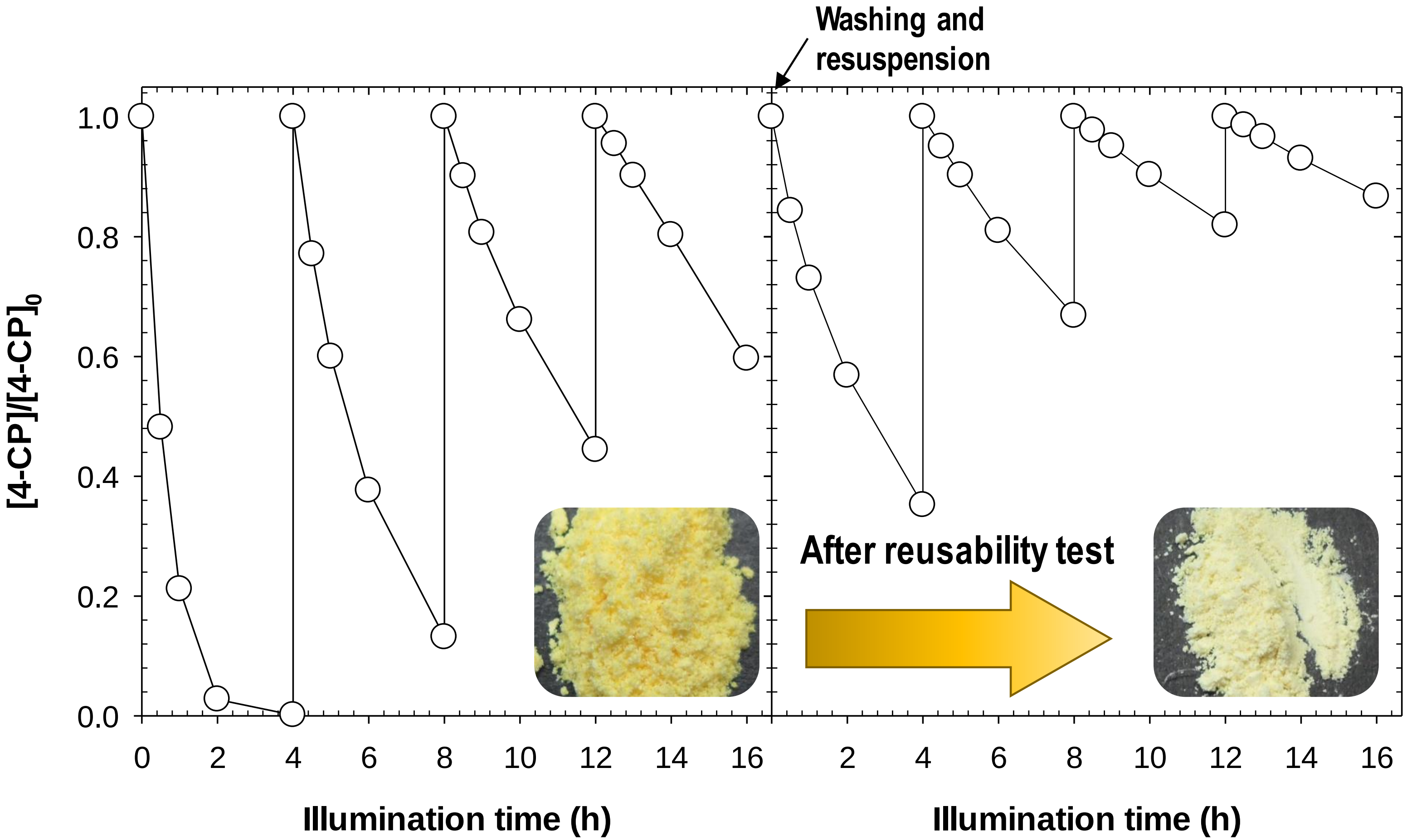

Fig. 3.1.11. Repeated degradation of 4-CP by Am-peroxo-TiO_2 under visible light illumination ([Am-peroxo-TiO_2] = 0.5 g/L, [4-CP]$_0$ = 10 μM, pH = 5, I = 6.43×10^{-6} Einstein/L·s (fluorescent lamp, λ > 400 nm)).

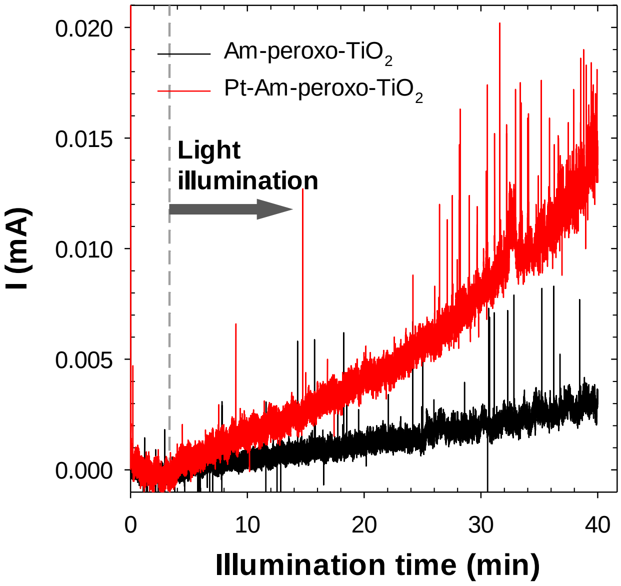

Fig. 3.1.12. Generation of Fe(III)/Fe(II) redox couple photocurrent of Am-peroxo-TiO_2 (and Pt-Am-peroxo-TiO_2) under visible light irradiation ([Am-peroxo-TiO_2]$_0$ = [Pt-Am-peroxo-TiO_2]$_0$ = 0.5 g/L, [4–CP]$_0$ = 0.1 mM, [$NaClO_4$]$_0$ = 0.1 M, [Fe(III)]$_0$ = 1 mM, pH = 1.8, I = 2.46×10^{-5} Einstein/L·s (xenon arc lamp, $\lambda > 400$ nm), working and counter electrodes = platinum plate (2.5 cm x 1.5 cm), reference electrode = Calomel electrode, bias potential = +0.7 V).

1.4. Oxidation products of 4-CP

HPLC and LC/MS analyses identified 14 products from the photochemical degradation of 4-CP by illuminated Am-peroxo-TiO_2. The identified products (listed in Table 3.1.1), the corresponding time-dependent variations of their abundance and chromatograms for the identified products are presented in Figs. 3.1.13–15 in the supplementary data. Based on these results, the degradation pathways of 4-CP were determined (Fig. 3.1.16).

4-Chlorocatechol (Product 7), hydroquinone (Product 2), and benzoquinone (Product 1) were the primary oxidation products of the reaction, which is consistent with previous observations of photocatalysis of 4-CP with bare TiO_2 [90-93]. Hydroquinone and benzoquinone were further oxidized to hydroxyquinol (Product 4), hydrobenzoquinone (Product 3), 1,2,4,5-benzenetetriol (Product 6), and 2,5-dihydroxy-1,4-benzoquinone (Product 5). 4-Chlorocatechol was further oxidized to chloromaleic acid (Product 8), *(2E,4E)*-3-chloro-2,4-hexadienedioic acid (Product 11), 5-chloro-1,2,4-benzenetriol (Product 10), and 4-chloro-5-hydroxy-1,2-benzoquinone (Product 9). In addition, bicyclic compounds such as dichlorobiphenyl (Product 14) and 5-chloro-2,4-dihydroxybiphenyl (Product 13) were also found.

Table 3.1.1. Products of 4-CP degradation by visible light-illuminated Am-peroxo-TiO_2 identified by HPLC and LC/MS analyses.

Product No.	Compounds	Chemical formula	Theoretical m/z	Observed m/z	Δ (ppm)	Ionization form	Analysis method
1	Benzoquinone	$C_6H_4O_2$	107.0138	108.0206	-11135.01	$[M]^-$	HPLC, LC-MS
2	Hydroquinone	$C_6H_6O_2$	-	-	-	-	HPLC
3	Hydroxybenzoquinone	$C_6H_4O_3$	123.0087	123.0075	9.76	$[M-H]^-$	LC-MS
4	Hydroxyquinol	$C_6H_6O_3$	125.0244	125.0236	6.40	$[M-H]^-$	LC-MS
5	2,5-Dihydroxy-1,4- benzoquinone	$C_6H_4O_4$	139.0036	139.0027	6.47	$[M-H]^-$	LC-MS
6	1,2,4,5-Benzenetetrol	$C_6H_6O_4$	141.0182	141.0183	-0.71	$[M-H]^-$	LC-MS
7	4-Chlorocatechol	$C_6H_5O_2Cl$	142.9905	142.9898	4.90	$[M-H]^-$	HPLC, LC-MS
8	Chloromaleic acid	$C_4H_3O_4Cl$	148.9647	148.9634	8.73	$[M-H]^-$	LC-MS
9	4-Chloro-5-hydroxy-1,2,-benzoquinone	$C_6H_3O_3Cl$	156.9697	156.9693	2.55	$[M-H]^-$	LC-MS
10	5-Chloro-1,2,4,-benzenetriol	$C_6H_5O_3Cl$	158.9854	158.9846	5.03	$[M-H]^-$	LC-MS
11	(*2E*,*4E*)-3-Chloro-2.4-hexadienedioic acid	$C_6H_5O_4Cl$	174.9792	174.9799	-4.00	$[M-H]^-$	LC-MS
12	2-Chloro-5-hydroxy-2,4-hexadienedioic acid	$C_6H_5O_5Cl$	190.9741	190.9976	-123.05	$[M-H]^-$	LC-MS
13	5-Chloro-2,4-dihydroxybiphenyl	$C_{12}H_9O_2Cl$	219.0207	219.0214	-3.20	$[M-H]^-$	LC-MS
14	Dichlorobiphenyl	$C_{12}H_8Cl_2$	220.9930	221.0009	-35.75	$[M-H]^-$	LC-MS

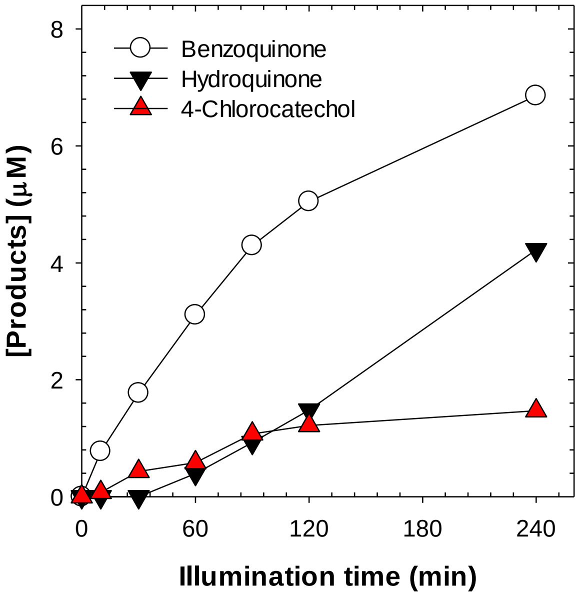

Fig. 3.1.13. Formation of oxidation products during 4-CP degradation by Am-peroxo-TiO_2 under visible light illumination ([Am-peroxo-TiO_2] = 0.5 g/L, $[4\text{-CP}]_0 = 0.1$ mM, pH = 5, I = 6.43×10^{-6} Einstein/L·s (fluorescent lamp, $\lambda > 400$ nm)).

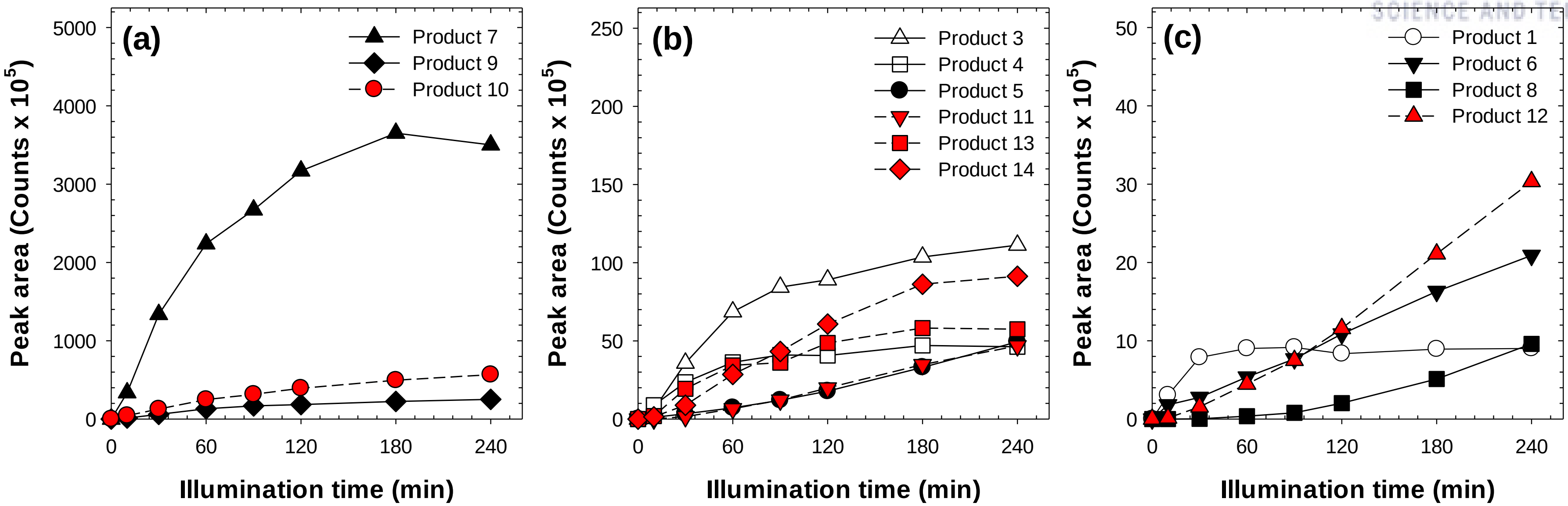

Fig. 3.1.14. Formation of oxidation products during 4-CP degradation by Am-peroxo-TiO_2 under visible light illumination ([Am-peroxo-TiO_2] = 0.5 g/L, $[4\text{-CP}]_0$ = 0.1 mM, pH = 5, I = 6.43 × 10^{-6} Einstein/L·s (fluorescent lamp, λ > 400 nm)).

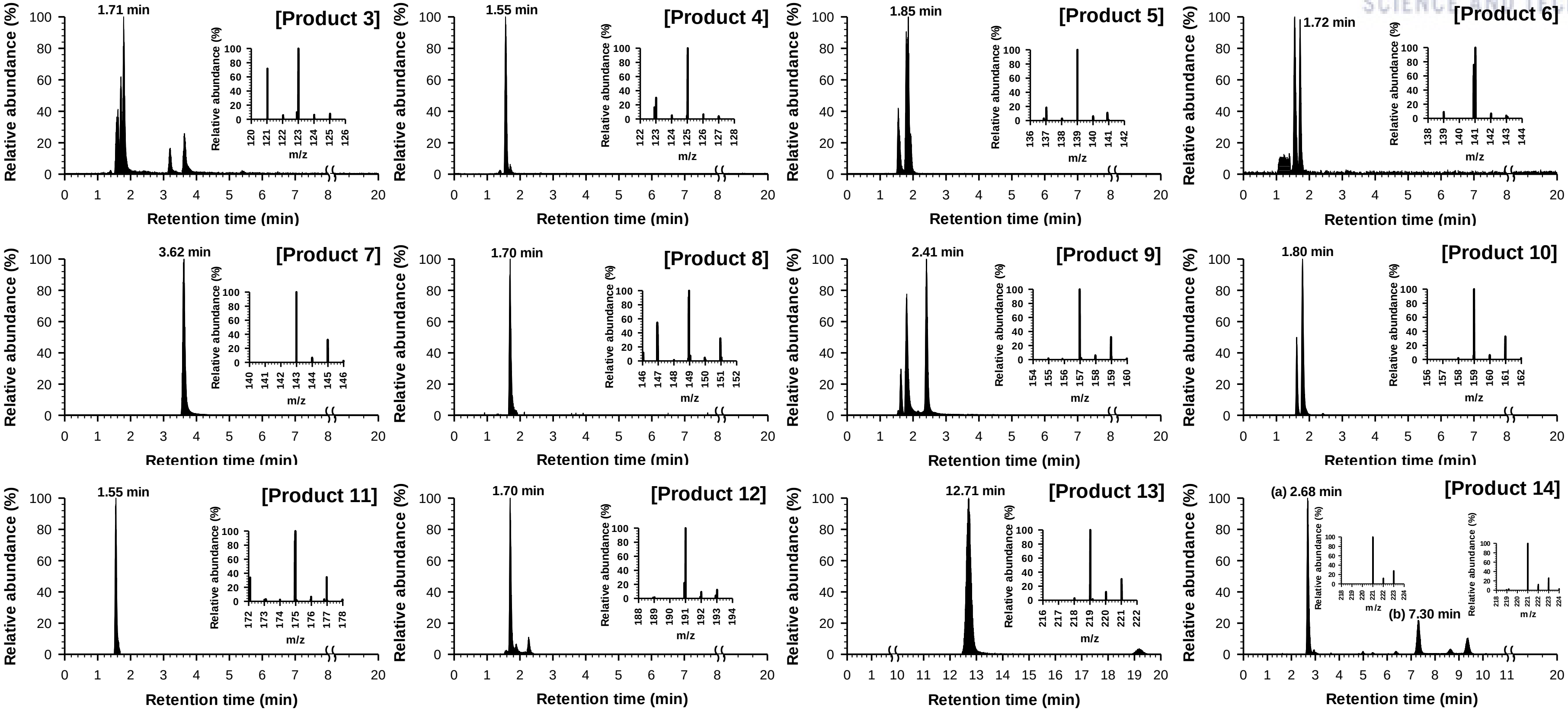

Fig. 3.1.15. Formation of oxidation products during 4-CP degradation by Am-peroxo-TiO_2 under visible light illumination: chromatograms of oxidation products at 4h with mass spectra ([Am-peroxo-TiO_2] = 0.5 g/L, $[4\text{-CP}]_0$ = 0.1 mM, pH = 5, I = 6.43×10^{-6} Einstein/L·s (fluorescent lamp, λ > 400 nm)).

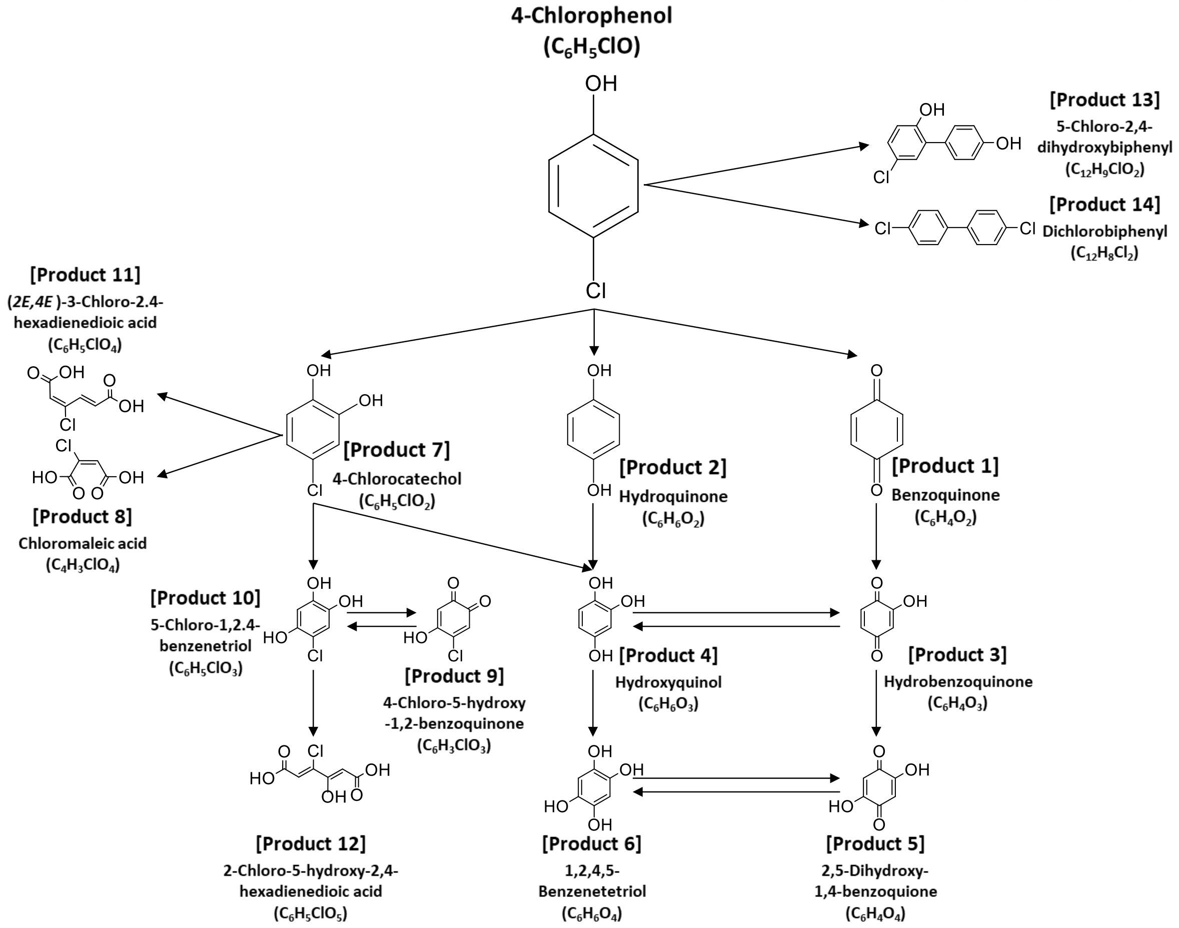
4-Chlorophenol
(C_6H_5ClO)
OH
Cl
[Product 13]
5-Chloro-2,4-dihydroxybiphenyl
($C_{12}H_9ClO_2$)
[Product 14]
Dichlorobiphenyl
($C_{12}H_8Cl_2$)
[Product 11]
(2E,4E)-3-Chloro-2.4-hexadienedioic acid
($C_6H_5ClO_4$)
[Product 8]
Chloromaleic acid
($C_4H_3ClO_4$)
[Product 7]
4-Chlorocatechol
($C_6H_5ClO_2$)
[Product 2]
Hydroquinone
($C_6H_6O_2$)
[Product 1]
Benzoquinone
($C_6H_4O_2$)
[Product 10]
5-Chloro-1,2.4-benzenetriol
($C_6H_5ClO_3$)
[Product 9]
4-Chloro-5-hydroxy-1,2-benzoquinone
($C_6H_3ClO_3$)
[Product 4]
Hydroxyquinol
($C_6H_6O_3$)
[Product 3]
Hydrobenzoquinone
($C_6H_4O_3$)
[Product 12]
2-Chloro-5-hydroxy-2,4-hexadienedioic acid
($C_6H_5ClO_5$)
[Product 6]
1,2,4,5-Benzenetetriol
($C_6H_6O_4$)
[Product 5]
2,5-Dihydroxy-1,4-benzoquione
($C_6H_4O_4$)

Fig. 3.1.16. Pathways depicting oxidative degradation of 4-CP by Am-peroxo-TiO_2 under visible light illumination.

2. Discussion

2.1 Photochemical activity of Am-peroxo-TiO_2

Am-peroxo-TiO_2 appears to demonstrate comparable or superior visible-light responsive photochemical activity to the photocatalysts reported in previous studies (although explicit comparison is difficult, given the nuances of experimental conditions such as the intensity and profile of incident light, etc.). In this study, photochemical degradation of 4-CP by Am-peroxo-TiO_2 was 96% in 4 h (Fig. 3.1.5a), which was more rapid than what was reported previously for nonmetal-doped TiO_2. For example, 4-CP degradation by N-doped TiO_2, S-doped TiO_2, and C/S-codoped TiO_2 was approximately 25%, 90%, and 35% in 3 h, 6 h, and 3 h, respectively, under visible light illumination using 150-300 W xenon arc and halogen lamps [94-96]. Ce/N-codoped TiO_2 and oxygen-rich TiO_2 exhibited faster degradation kinetics of organic dyes under visible-light illumination (100% and 98% degradation in 5 h and 3 h, respectively) [8, 45]. Importantly, dyes used as target compounds can also serve as photosensitizers, thereby accelerating any photochemical processes. Additionally, Shankar et al. reported that peroxo-titania exhibited only a two-fold greater activity for methanol oxidation (to formaldehyde) than P25 under visible light illumination [43]. Note that the 4-CP degradation rate by Am-peroxo-TiO_2 was 9.6-fold greater than that of P25 (Fig. 3.1.5a)

2.2 Roles of ROS

Earlier studies on photochemical systems using TiO_2/H_2O_2 [41] and peroxo-titania [43] suggest that $^{\bullet}OH$ serves as a major reactive oxidant, and is responsible for the degradation of organic compounds. It has been suggested that photoexcited peroxo-titania complexes transfer electrons to the conduction band of TiO_2, facilitating the conversion of adsorbed H_2O_2 to $^{\bullet}OH$ by one-electron reduction.

However, experimental results from this study present evidence against $^{\bullet}OH$. The data suggests that Am-peroxo-TiO_2 may have different photochemical properties from other TiO_2 systems with peroxo-functionality that have been reported previously [41,43]. First, the selective degradation of organic compounds (Fig. 3.1.7) cannot be explained by the reaction of $^{\bullet}OH$ since $^{\bullet}OH$, a powerful oxidant ($E°[^{\bullet}OH/H_2O] = +2.80\ V_{NHE}$), nonselectively oxidizes organic compounds at diffusion-controlled reaction rates ($>10^9\ M^{-1}\ s^{-1}$) [98]. Second, the negligible effects of $^{\bullet}OH$ scavengers (methanol and *tert*-butanol) on 4-CP degradation also lends support to the idea that $^{\bullet}OH$ plays an insignificant role (Fig. 3.1.8a). In addition, when excess BA and coumarin were employed as $^{\bullet}OH$ probes in the illuminated Am-peroxo-TiO_2 suspension, the reaction did not yield the expected hydroxylated products (*p*-HBA and 7-HC), which implies that BA and coumarin were either not oxidized at all or were oxidized but do not produce hydroxylated products (Fig. 3.1.17). Lastly, the XTT assay did not detect $O_2^{\bullet-}$ in the illuminated Am-peroxo-TiO_2 suspension (Fig. 3.1.9), indicating that $O_2^{\bullet-}$ does not affect 4-CP degradation.

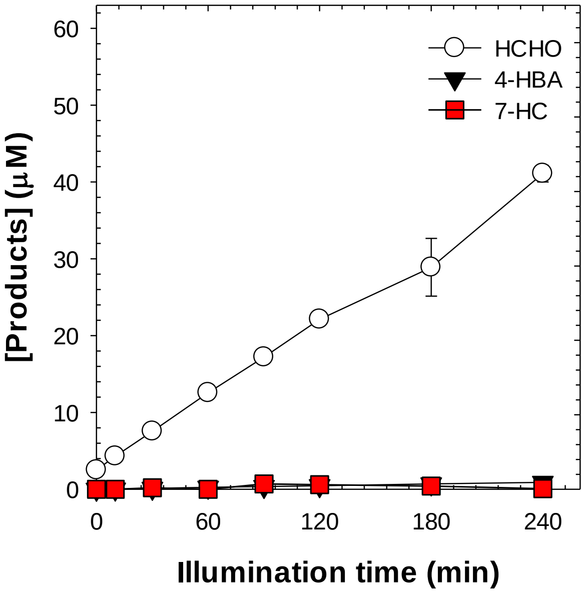

Fig. 3.1.17. Production of HCHO, 4-HBA, and 7-HC by Am-peroxo-TiO_2 under visible light illumination. ([Am-peroxo-TiO_2] = 0.5 g/L, $[Methanol]_0$ = 200 mM, $[BA]_0$ = 10 mM, $[Coumarin]_0$ = 1 mM, pH = 5, I = 6.43 × 10^{-6} Einstein/L·s (fluorescent lamp, λ > 400 nm)).

2.3 Photochemical reactions of illuminated Am-peroxo-TiO_2

Photochemical reactions of illuminated Am-peroxo-TiO_2 are proposed in Fig. 3.1.18 (also refer to reactions 3.1.1–4 below). When surface Ti (IV)-peroxo complexes are photoexcited under visible-light illumination (reaction 3.1.1), an electron transfers to the conduction band (CB) of TiO_2, generating an oxidized peroxo intermediate ($[\equiv Ti^{IV}–^{\bullet}OOH]^+$) (reaction 3.1.2). Electron transfer from the CB to the surface peroxo complexes generates a reduced peroxo intermediate ($[\equiv Ti^{III}–OOH]^-$) (reaction 3.1.3). The two photogenerated intermediates ($[\equiv Ti^{IV}–^{\bullet}OOH]^+$ and $[\equiv Ti^{III}–OOH]^-$) immediately recombine on the surface (reaction 3.1.4). Am-peroxo-TiO_2 is stable under visible light irradiation (Fig. 3.1.10a), as a result of rapid electron circulation that occurs through reactions 3.1.1–4.

$$\equiv Ti^{IV}–OOH + hv\ (>400\ nm) \rightarrow [\equiv Ti^{IV}–OOH]^* \qquad (3.1.1)$$

$$[\equiv Ti^{IV}–OOH]^* \rightarrow [\equiv Ti^{IV}–^{\bullet}OOH]^+ + e^-\ (CB\ of\ TiO_2) \qquad (3.1.2)$$

$$\equiv Ti^{IV}–OOH + e^-\ (CB\ of\ TiO_2) \rightarrow [\equiv Ti^{III}–OOH]^- \qquad (3.1.3)$$

$$[\equiv Ti^{IV}–^{\bullet}OOH]^+ + [\equiv Ti^{III}–OOH]^- \rightarrow 2 \equiv Ti^{IV}–OOH \qquad (3.1.4)$$

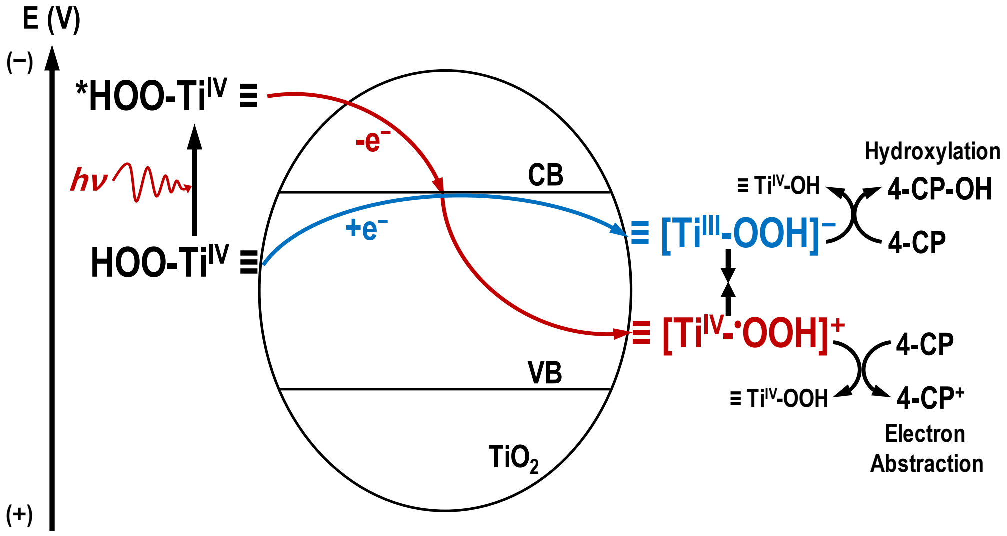

Fig. 3.1.18. Schematic diagrams of photochemical reactions occurring on visible light-illuminated Am-peroxo-TiO_2 in the absence (a) and presence (b) of organic compounds.

2.4 Mechanism of organic compound degradation by illuminated Am-peroxo-TiO_2

The data suggests that the two photogenerated intermediates ($[\equiv Ti^{IV}–{}^\bullet OOH]^+$ and $[\equiv Ti^{III}–OOH]^-$) are responsible for the oxidative degradation of organic compounds (Fig. 3.1.18). These intermediates, $[\equiv Ti^{IV}–{}^\bullet OOH]^+$ and $[\equiv Ti^{III}–OOH]^-$, are believed to exhibit similar properties to surface-bound $HO_2^\bullet$ and ${}^\bullet OH$, respectively. $[\equiv Ti^{IV}–{}^\bullet OOH]^+$ can oxidize specific organic compounds (e.g., 4-CP) via an electron abstraction mechanism (reaction 3.1.5).

$$[\equiv Ti^{IV}–{}^\bullet OOH]^+ + 4\text{-CP} \rightarrow \equiv Ti^{IV}–OOH + 4\text{-CP}^+ \qquad (3.1.5)$$

$[\equiv Ti^{III}–OOH]^-$, which possesses ${}^\bullet OH$-like properties (e.g., $[\equiv Ti^{III}–OOH]^- \leftrightarrow [\equiv Ti^{IV}–O^-\cdots{}^\bullet OH]$), is assumed to hydroxylate a given organic compound (reaction 3.1.6).

$$[\equiv Ti^{III}–OOH]^- + 4\text{-CP} \xrightarrow{H^+} \equiv Ti^{IV}–OH + 4CP\text{-}OH \qquad (3.1.6)$$

The primary products of 4-CP oxidation (4-chlorocatechol (Product 7), hydroquinone (Product 2), and benzoquinone (Product 1)) can form via reactions initiated by electron abstraction and hydroxylation of 4-CP, as described in Fig. 3.1.19.

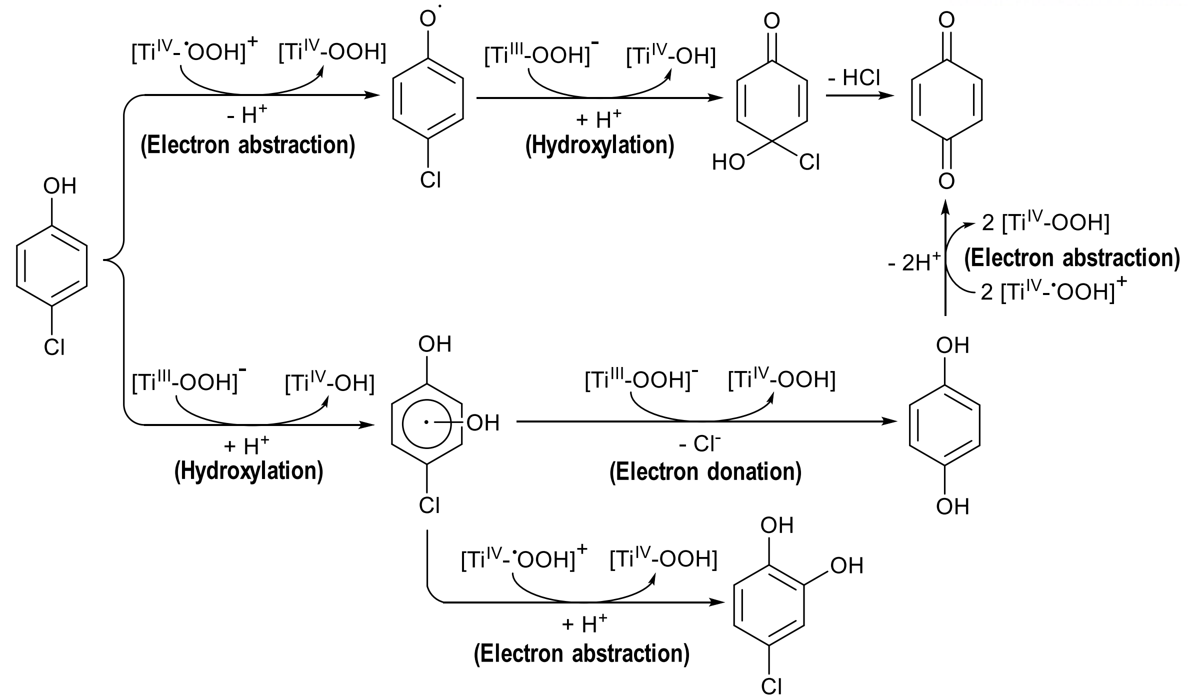
[Ti^IV-•OOH]+
[Ti^IV-OOH]
- H+
(Electron abstraction)
[Ti^III-OOH]-
[Ti^IV-OH]
+ H+
(Hydroxylation)
- HCl
HO
Cl
OH
Cl
O
2 [Ti^IV-OOH]
- 2H+
(Electron abstraction)
2 [Ti^IV-•OOH]+
[Ti^III-OOH]-
[Ti^IV-OH]
+ H+
(Hydroxylation)
[Ti^III-OOH]-
[Ti^IV-OOH]
- Cl-
(Electron donation)
[Ti^IV-•OOH]+
[Ti^IV-OOH]
+ H+
(Electron abstraction)

Fig. 3.1.19. Proposed mechanisms for primary oxidation of 4-CP by visible light-illuminated Am-peroxo-TiO_2.

The loss of activity arising from illuminated Am-peroxo-TiO_2 in the repetition test with 4-CP degradation (Fig. 3.1.10) can be attributed to the destruction of surface peroxo groups by the reaction of $[\equiv Ti^{III}–OOH]^{-}$ with 4-CP (reaction 3.1.6). XPS data revealed that surface peroxo groups on Am-peroxo-TiO_2 almost disappeared after the reaction (Figs. 3.1.20a and b). Diffuse reflectance also increased after the reaction (Fig. 3.1.21a), which coincided with the fading of the yellow color of the powdered material.

Pt-Am-peroxo-TiO_2 exhibited enhanced photostability in the presence of 4-CP (Fig. 3.1.10b). Namely, the loss of surface peroxo groups was relatively small (Figs. 3.1.20c and d), and the increase in diffuse reflectance was also minor (Fig. 3.1.21b). It is believed that the Pt deposits trap electrons from the CB of TiO_2 [99] (also evidenced by the enhanced generation of photocurrents (Fig. 3.1.12), thereby inhibiting the formation of $[\equiv Ti^{III}–OOH]^{-}$ and reducing the subsequent loss of peroxo groups (reaction 3.1.6). The suppressed formation of $[\equiv Ti^{III}–OOH]^{-}$ also inhibited the recombination of $[\equiv Ti^{IV}–{}^{\bullet}OOH]^{+}$ and $[\equiv Ti^{III}–OOH]^{-}$ (reaction 3.1.4), which caused an enhancement of photochemical activity of the material; 4-CP degradation by Pt-Am-peroxo-TiO_2 occurs more rapidly than with Am-peroxo-TiO_2 (Fig. 3.1.10b). Although it has been reported that the redox states of Pt defects in the TiO_2 lattice can improve visible-light absorption [100], such an effect was not seen with our materials when comparing the reflectance spectra of Am-peroxo-TiO_2 and Pt-Am-peroxo-TiO_2 (Figs. 3.1.21a and b).

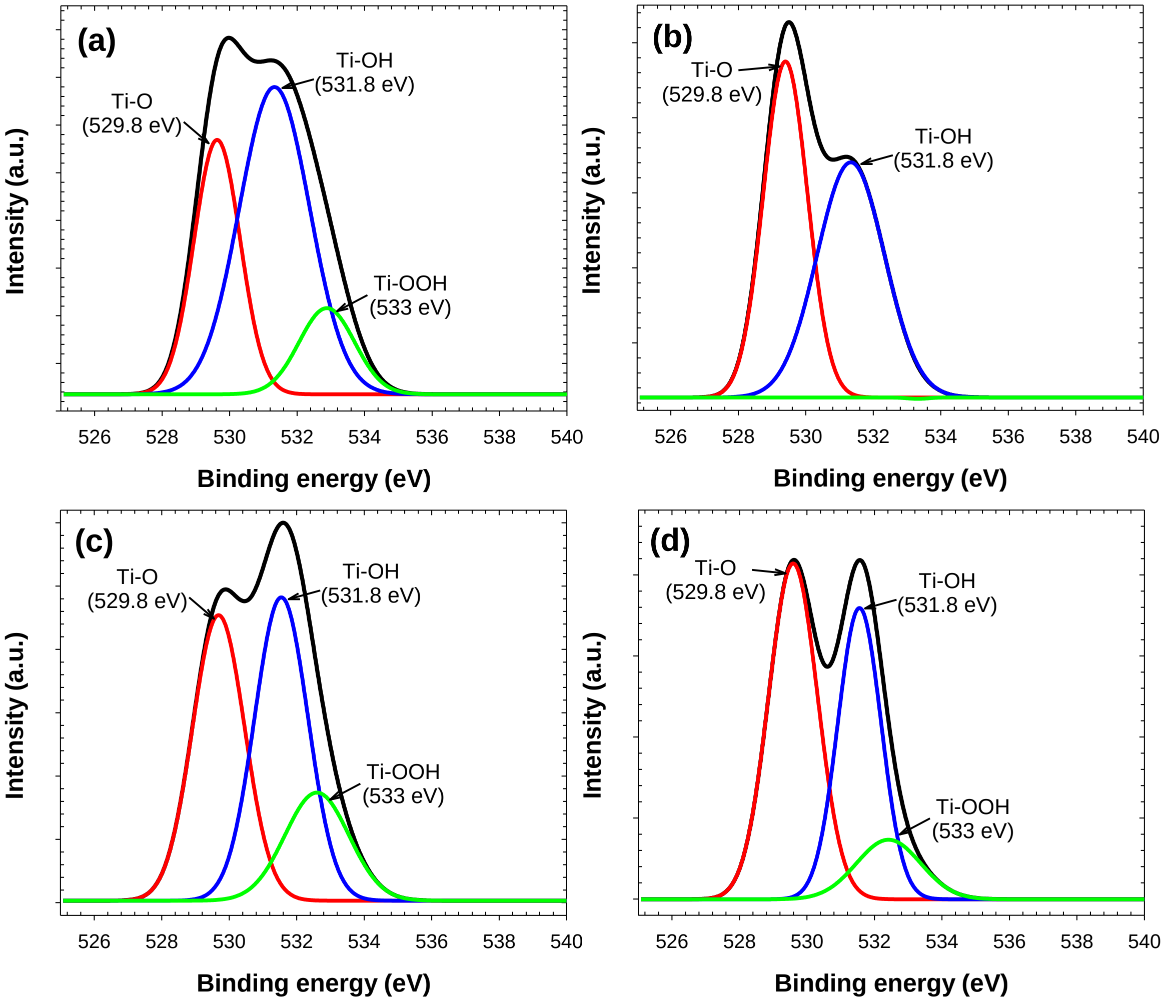

Fig. 3.1.20. X-ray photoelectron spectra (O 1s level) of Am-peroxo-TiO_2 (a, b) and Pt-Am-peroxo-TiO_2 (c, d) before (a, c) and after (b, d) 4-CP degradation under visible light illumination ($[\text{Am-peroxo-TiO}_2]_0 = [\text{Pt-Am-peroxo-TiO}_2]_0 = 0.5$ g/L, $[\text{4-CP}]_0 = 10$ μM, pH = 5, I = 6.43×10^{-6} Einstein/L·s (fluorescent lamp, λ > 400 nm)).

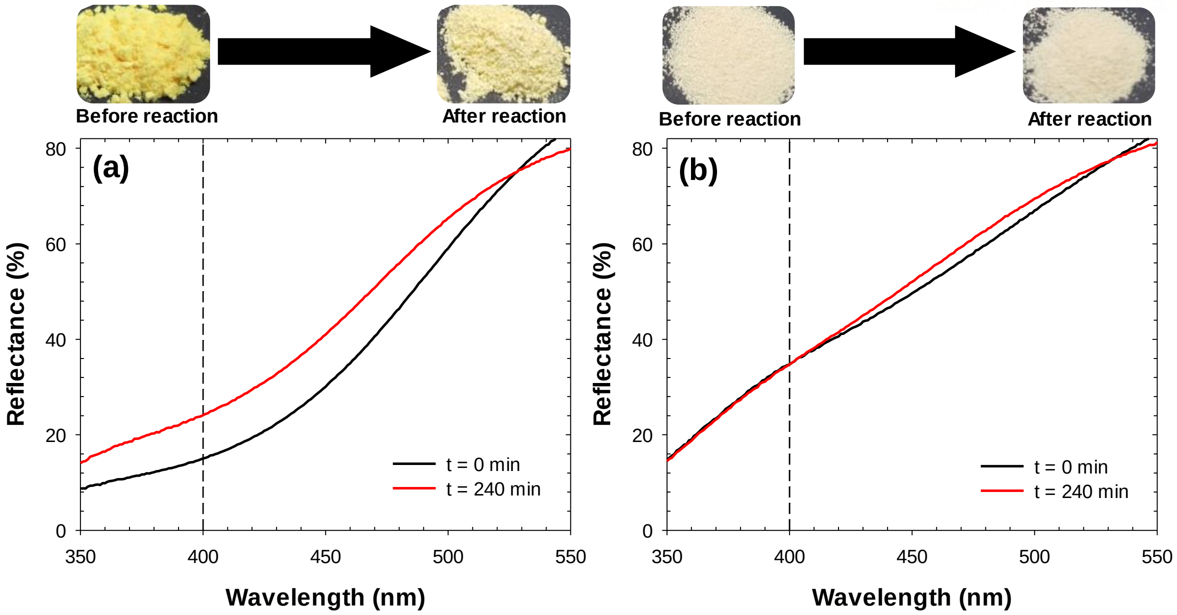

Fig. 3.1.21. Diffuse reflectance spectra of Am-peroxo-TiO_2 (a) and Pt-Am-peroxo-TiO_2 (b) before and after 4-CP degradation under visible light illumination ([Am-peroxo-TiO_2] = [Pt-Am-peroxo-TiO_2] = 0.5 g/L, $[4\text{-CP}]_0 = 10$ μM, pH = 5, $I = 6.43 \times 10^{-6}$ Einstein/L·s (fluorescent lamp, $\lambda > 400$ nm)).

4-CP degradation via the LMCT mechanism of $\equiv TiO_2$-4-CP complexes was also ruled out. The minor effects of oxygen in this system (Fig. 3.1.8b) contrasts those observed with the LMCT mechanism, in which oxygen acts as an electron acceptor to significantly accelerate 4-CP degradation by trapping electrons from surface complexes [85]. In this study, oxygen had a minor effect. Furthermore, in our proposed mechanism the negligible effect of oxygen suggests that oxygen fails to capture electrons from the CB of TiO_2 (possibly due to the rapid transit of CB electrons to the surface peroxo complexes), and correspondingly fails to abstract electrons from $[\equiv Ti^{III}–OOH]^-$. In addition, the positive effect of platiniazation (Fig. 3.1.10b) contradicts the LMCT mechanism, as Pt deposition acts as physical barriers, which is known to inhibit the formation of charge-transfer complexes of TiO_2 with the organic compound [85,101].

II. Sulfur doped TiO_2 (S-TiO_2)

1. Results

1.1. Synthesis and characterization of S-TiO_2

The XRD patterns and HRTEM images of S-TiO_2 were shown in Fig. 3.2.1. XRD patterns of S-TiO_2 recorded a mixed crystalline structure of anatase and rutile phases with high crystallinity (Fig. 3.2.1a). In general, anatase titania is nonreversibly converted to rutile at a temperature range of 600-700 °C [102]. However, the phase transition at high temperature was inhibited by the generation of titanyl oxysulfate ($TiOSO_4$) in the mixture of titanium isopropoxide and sulfuric acid [33]. $TiOSO_4$ remains its stable state up to 600°C [33] and, above 600°C, converts its structure to the sulfur-doped anatase phase. HRTEM images indicated that S-TiO_2 forms a rectangular-shaped crystalline structure (the average size is 50 nm) (Fig. 3.2.1b). Additionally, HRTEM-EDX reveals that S-TiO_2 contains 67.2, 32.7, and 0.1wt% of titanium, oxygen, and sulfur, respectively, which result coincides with the XRF analysis (Fig. 3.2.1b).

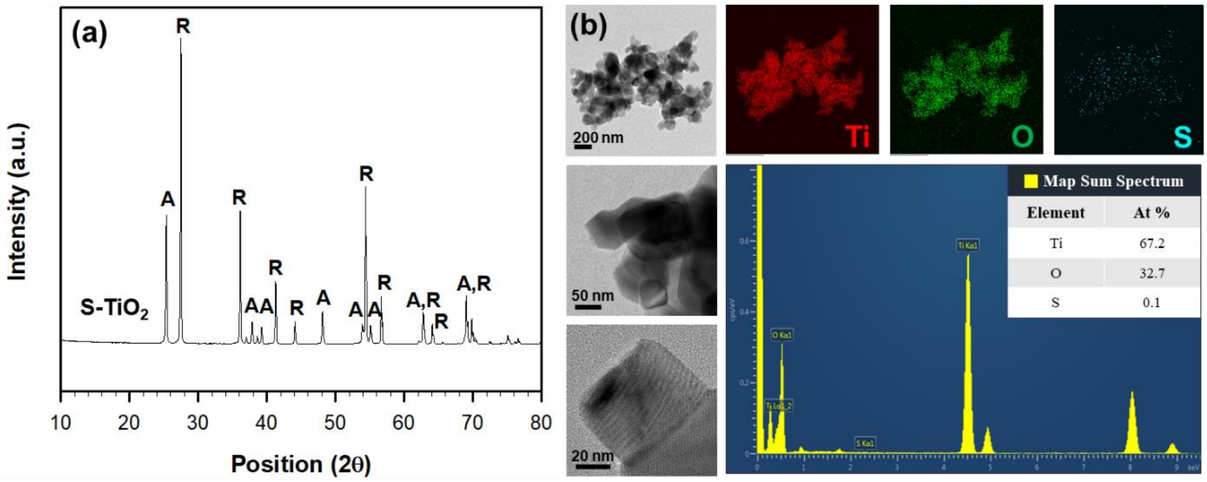

Map Sum Spectrum

Element	At %
Ti	67.2
O	32.7
S	0.1

Fig. 3.2.1. XRD pattern (a) and HRTEM image (b) of S-TiO_2. Notations ‘A’ and ‘R’ in (a) represent anatase and rutile crystalline phase.

An FT-IR spectrum of S-TiO_2 measured to confirm the existence of sulfur at the surface of S-TiO_2 (Fig. 3.2.2). The Ti-O-S functional groups are known to absorb the IR energy in the range of 1050 cm^{-1} to 1135 cm^{-1} [103]. The FT-IR spectrum of S-TiO_2 displayed an IR absorption peak centered at 1126 cm^{-1} that was attributed to Ti-O-S (Fig. 3.2.2).

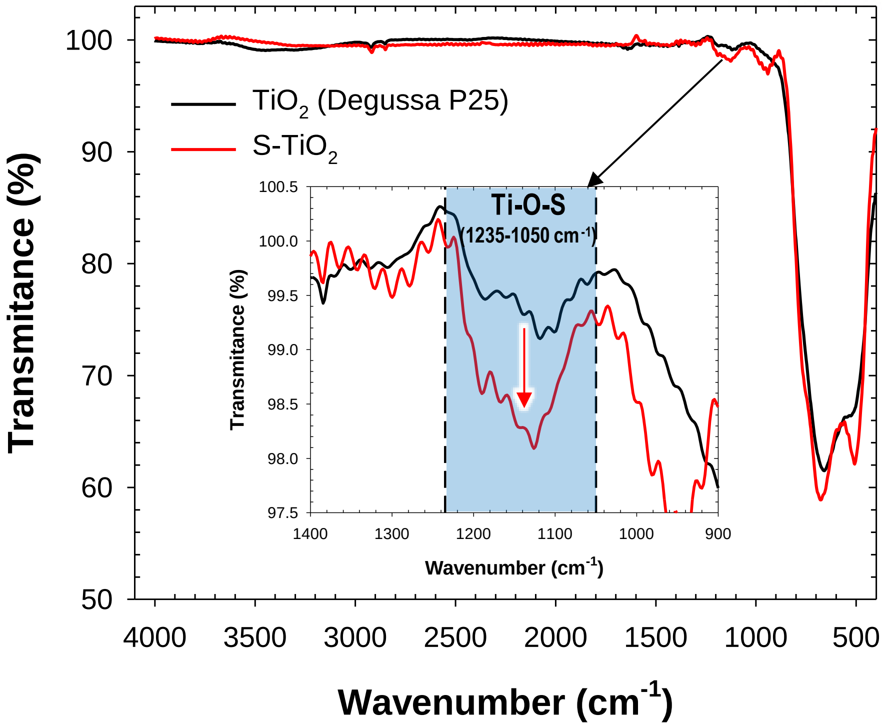

Fig. 3.2.2. FT-IR spectra of S-TiO_2 and TiO_2 (degussa P25).

The synthesized S-TiO_2 showed a bright-faint yellow color, which indicates that the synthesized S-TiO_2 weakly absorbs visible light. The diffuse reflectance spectrum of S-TiO_2 showed that the light absorption was observed in the wavelength range of 400 nm to 750 nm (Fig. 3.2.3a). To determine the bandgap energy and band position of S-TiO_2, a plot of modified Kubelka-Munk function versus the light energy and valence band XPS were utilized (Fig. 3.2.3) [104,105]. The Kubelka-Munk fuction, F(R), is known as equation (3.2.1), where R is the relative reflectance ratio of sample to standard $BaSO_4$.

$$\mathrm{F(R)} = \frac{(1-R)^2}{2R} \tag{3.2.1}$$

The modified Kubelka-Munk function is given as $[\mathrm{F(R)}E]^{\frac{1}{2}}$ where E indicates the light energy. The calculated bandgap energy was 2.92 eV. The valence band XPS indicated a valence band edge of the S-TiO_2 and the calculated valence band edge of S-TiO_2 was 2.35 eV (Fig. 3.2.3b). From the basis of the calculations, the electronic band structure of S-TiO_2 is expressed in Fig. 3.2.3c. The synthesized S-TiO_2 had a less positive energy level of conduction band comparing with bare TiO_2 (E_{VB} = +2.69 V at pH 7.0), which indicates the decrease of oxidizing power in S-TiO_2 [88].

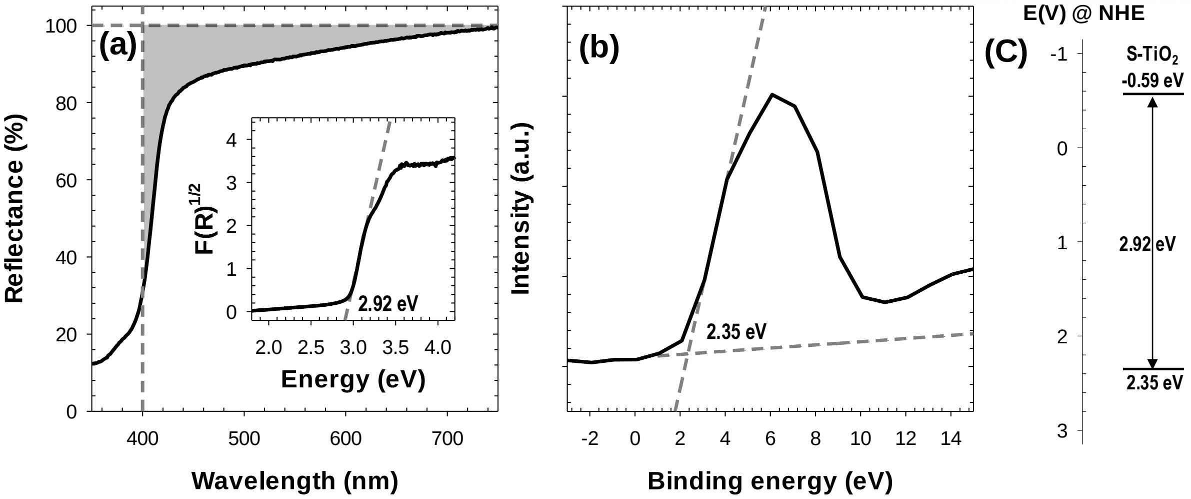

Fig. 3.2.3. Diffuse reflectance spectrum (a), valence band XPS (b), and electronic band structure (c) of S-TiO$_2$.

1.2. Photochemical degradation of organic compounds

Degradation of 4-CP by S-TiO$_2$/Fe(III) and the respective control systems (S-TiO$_2$ and Fe(III)) were examined under visible light illumination (Fig. 3.2.4a). S-TiO$_2$ system and Fe(III) system negligibly degraded 4–CP in 2 h. In contrast, the combined system of S-TiO$_2$/Fe(III) can completely degrade 4-CP in 2 h. Measurement of Fe(II) ion during the degradation of 4-CP indicates that approximately 90% of Fe(III) were reduced by the photocatalytic reaction of S-TiO$_2$ (Fig. 3.2.4b). Fe(III) adsorbed on the S-TiO$_2$ surface is reduced to Fe(II) via CB electron, which effectively prevents electron-hole recombination. The charge separation makes VB holes more available for the oxidation of organic compounds.

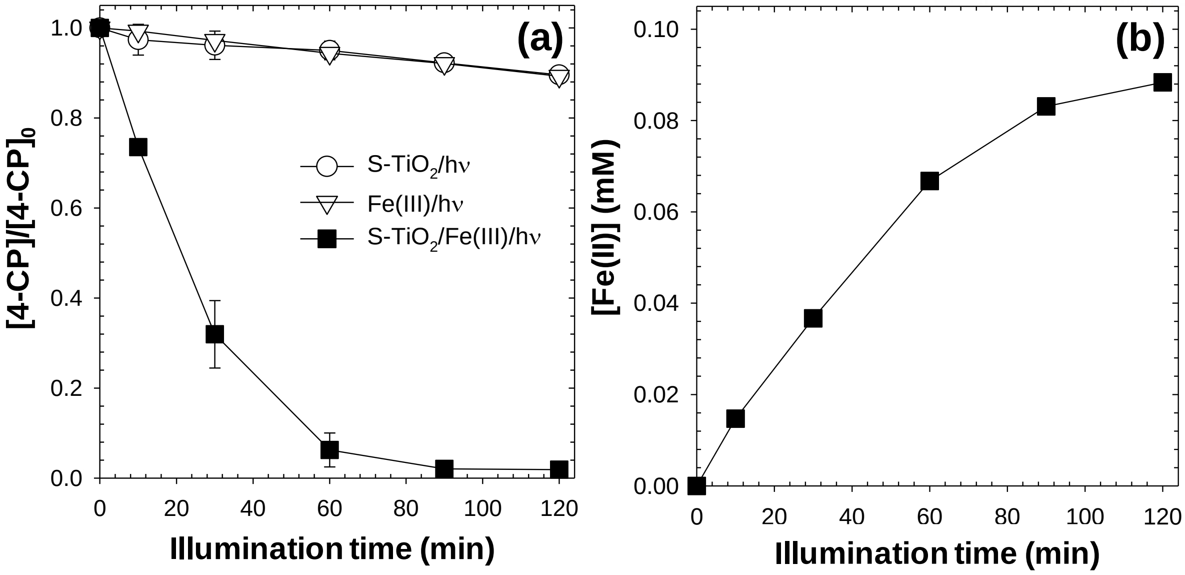

Fig. 3.2.4. Degradation of 4-CP (a) and reduction of Fe(III) (b) by S-TiO$_2$/Fe(III) system under visible light illumination ([S-TiO$_2$] = 0.5 g/L, [Fe(III)]$_0$ = 0.1 mM, [4-CP]$_0$ = 10 μM, pH = 3, I = 6.43 × 10^{-6} Einstein/L·s (fluorescent lamp, λ > 400 nm)).

Degradations of 4-CP by S-TiO$_2$/Fe(III) were investigated at different pH and varied Fe(III) concentration conditions under visible light illumination (Fig. 3.2.5). The pseudo-first order rate for the degradation of 4-CP was significantly accelerated only at pH 3.0 and drastically decreased in the range of pH 4.0-7.0, which may be affected by the limited usability of Fe(III) for the electron capture (Fig. 3.2.5a). The gradual increase in the pseudo-first order rate constant for the degradation of 4-CP was observed with increasing the initial concentration of Fe(III) until 0.1 mM (Fig. 3.2.5b). The maximized degradation rate was gradually decreased when the initial concentration of Fe(III) was further increased to 0.2 mM.

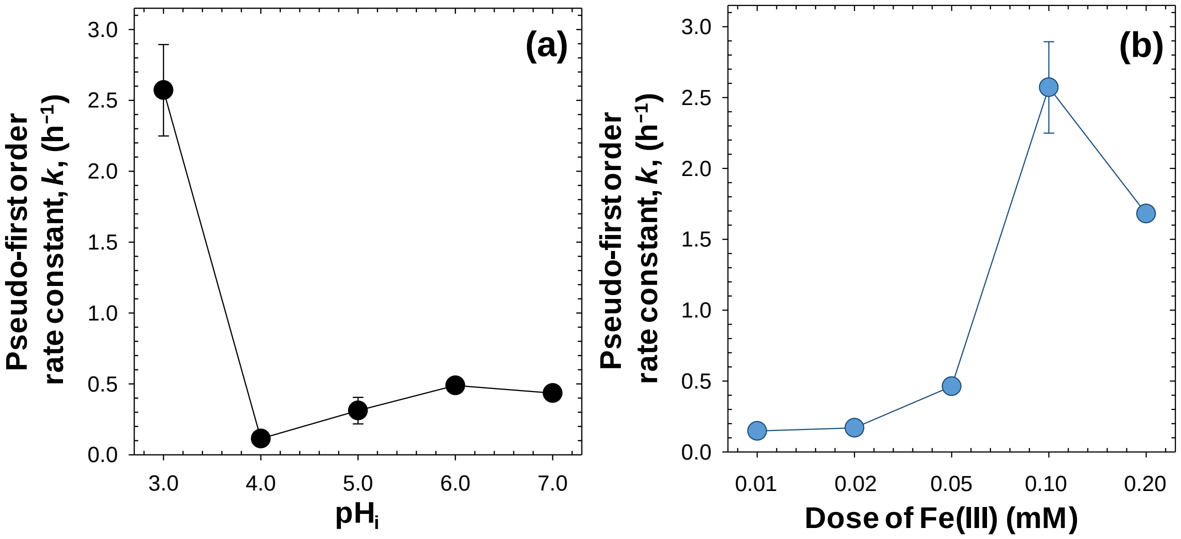

Fig. 3.2.5. Pseudo-first order rate constants for the degradation of 4-CP as a function of pH (a) and dose of Fe(III) (b) by S-TiO_2/Fe(III) system under visible light illumination ([S-TiO_2] = 0.5 g/L, [4-CP]$_0$ = 10 μM, I = 6.43 × 10^{-6} Einstein/L·s (fluorescent lamp, λ > 400 nm), [Fe(III)]$_0$ = 0.1 mM for (a), pH = 3 for (b)).

Degradation of benzoic acid by S-TiO_2/Fe(III)/H_2O_2 system and the respective control systems (Fe(III), H_2O_2, Fe(III)/H_2O_2, S-TiO_2/Fe(III), and S-TiO_2/H_2O_2) were examined (Fig. 3.2.6). The degradation of benzoic acid was negligible in the Fe(III), H_2O_2, S-TiO_2/Fe(III), and S-TiO_2/H_2O_2 systems without the visible light illumination (Fig. 3.2.6a). In the presence of Fenton-like reagents, partial amounts of benzoic acid were degraded without the visible light illumination (i.e., 15% and 34% for Fe(III)/H_2O_2 and S-TiO_2/Fe(III)/H_2O_2 systems, respectively). The degradation of benzoic acid was also negligible in Fe(III), H_2O_2, and S-TiO_2/Fe(III) under visible light illumination (Fig. 3.2.6b). 14% of benzoic acid was degraded by S-TiO_2/H_2O_2. Meanwhile, the combined system of Fe(III)/H_2O_2 and S-TiO_2/Fe(III)/H_2O_2 could completely degrade benzoic acid in 1 h under visible light illumination. S-TiO_2/Fe(III)/H_2O_2 system could effectively degrade benzoic acid comparing with Fe(III)/H_2O_2 under visible light illumination because Fe(II) reduced via conduction band electron from S-TiO_2 is used for the reaction with H_2O_2 (the Fenton reaction) to generate additional reactive oxidants.

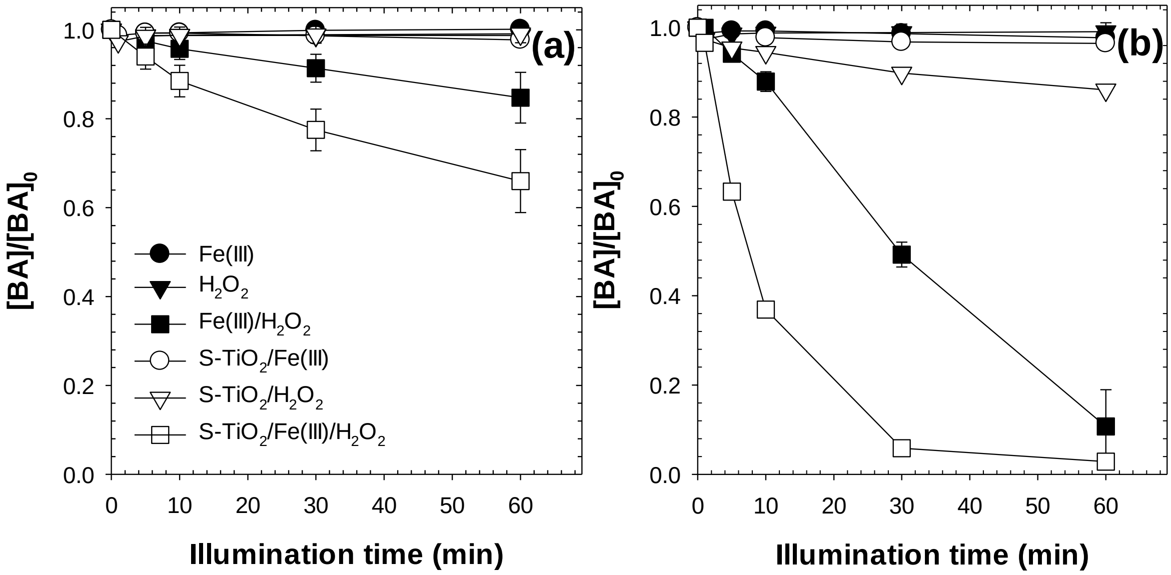

Fig. 3.2.6. Degradation of benzoic acid by S-TiO_2/Fe(III)/H_2O_2 systems under (a) dark condition and (b) visible light illumination ([S-TiO_2] = 0.5 g/L, $[Fe(III)]_0$ = 0.1 mM, $[H_2O_2]_0$ = 0.1 mM, $[BA]_0$ = 10 μM, pH = 3, I = 6.43 × 10^{-6} Einstein/L·s (fluorescent lamp, λ > 400 nm)).

Degradations of benzoic acid by S-TiO_2/Fe(III)/H_2O_2 were examined at different pH, and varied Fe(III) and H_2O_2 concentration conditions (Fig. 3.2.7). The calculated pseudo-first order rate constant for the degradation of benzoic acid was magnificent at pH 3.0 and drastically decreased with increasing the pH values, which showed similar trends with the degradation of 4-CP by S-TiO_2/Fe(III) system (Fig. 3.2.7a). The degradation rate of benzoic acid was enhanced with increasing the concentration of Fe(III) up to 0.08 - 0.1 mM (Fig. 3.2.7b). However, the iron loading over than 0.2 mM caused a gradual decrease in the degradation rate, which might be attributed to the iron oxyhydroxides precipitation on the S-TiO_2 surface. Fig. 3.2.7c shows that the increasement of H_2O_2 dosage caused a more effective degradation rate of benzoic acid under visible light illumination. However, the degradation rate of benzoic acid by Fe(III)/H_2O_2 system also drastically increased as increasing the injected concentration of H_2O_2 and exhibited the similar degradation rate with S-TiO_2/Fe(III)/H_2O_2 system in the high concentration of H_2O_2 (data are not shown). To emphasize the reduction effect of Fe(III) via photochemical reaction with S-TiO_2, 0.01 mM of H_2O_2 was utilized for the subsequent experiments.

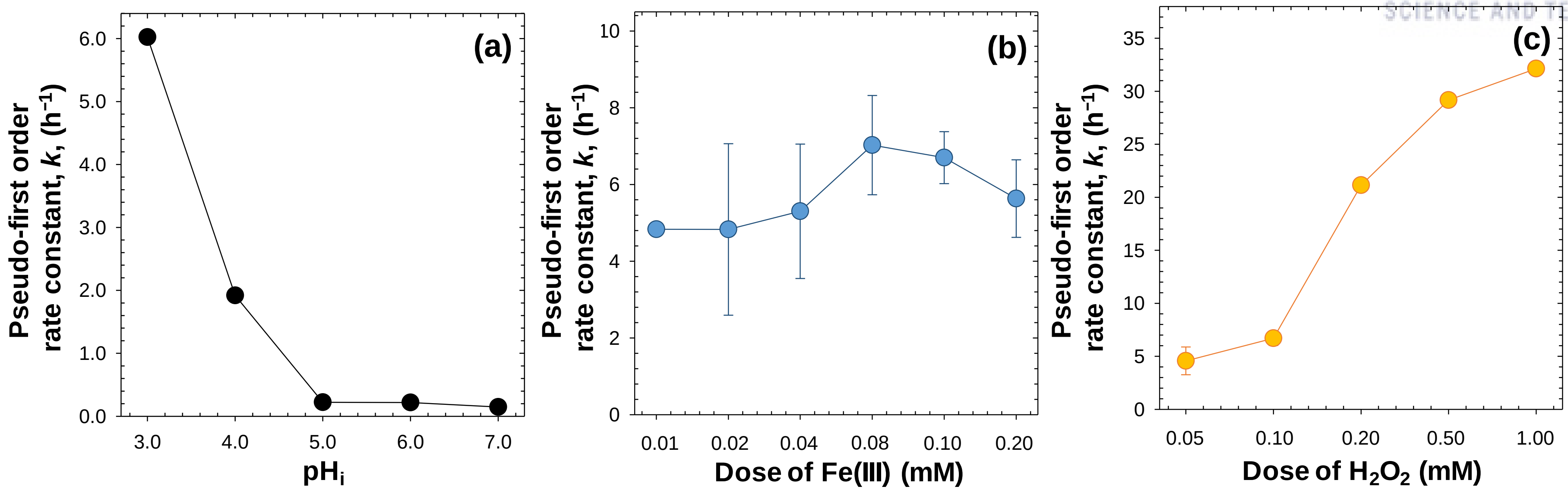

Fig. 3.2.7. Pseudo-first order rate constants for the degradation of benzoic acid as a function of pH (a), dose of Fe(III) (b), and dose of H_2O_2 (c) by S-TiO_2/Fe(III)/H_2O_2 system under visible light illumination ([S-TiO_2] = 0.5 g/L, $[BA]_0$ = 10 μM, I = 6.43 × 10^{-6} Einstein/L·s (fluorescent lamp, λ > 400 nm), $[H_2O_2]_0$ = 0.1 mM for (a) and (b), $[Fe(III)]_0$ = 0.1 mM for (a) and (c), pH = 3 for (b) and (c)).

Photochemical degradation of different organic compounds (phenol, 4–CP, BA, and CBZ) was examined in S-TiO_2/Fe(III) under visible light illumination (Fig. 3.2.8a). Phenol and 4-CP were mostly degraded by S-TiO_2/Fe(III) system under visible light illumination, however, BA and CBZ were negligibly degraded. On the other hand, S-TiO_2/Fe(III)/H_2O_2 system could degrade the target compounds effectively (Fig. 3.2.8b).

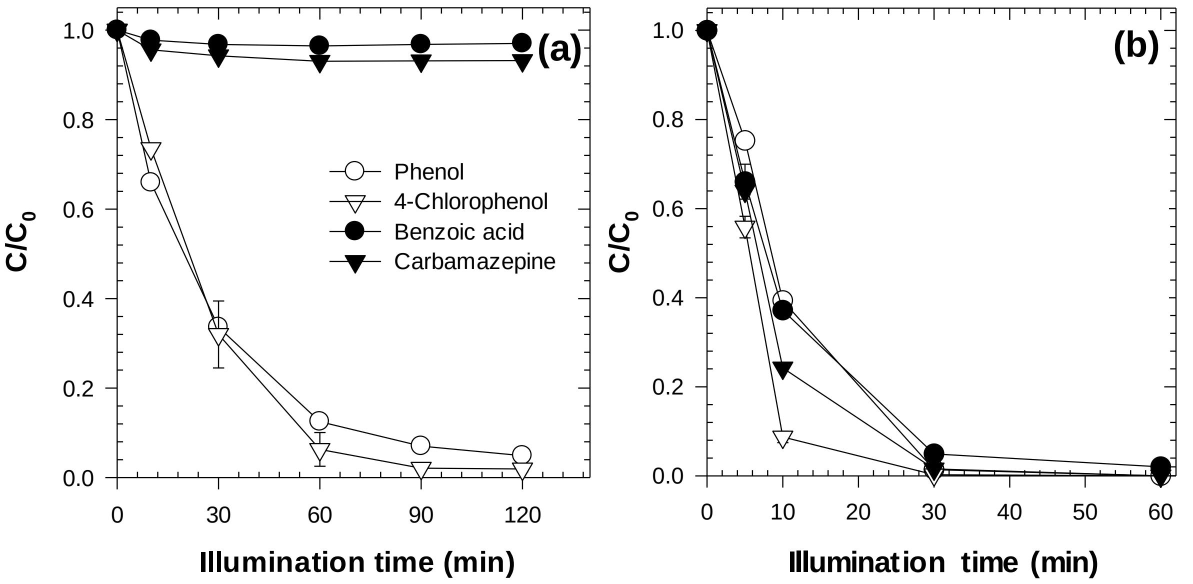

Fig. 3.2.8. Degradation of organic compounds by S-TiO_2/Fe(III) (a) and S-TiO_2/Fe(III)/H_2O_2 (b) under visible light illumination (([S-TiO_2] = 0.5 g/L, $[Fe(III)]_0$ = 0.1 mM, $[Phenol]_0 = [4\text{-}CP]_0 = [BA]_0 = [CBZ]_0$ = 10 μM, pH = 3, I = 6.43×10^{-6} Einstein/L·s (fluorescent lamp, $\lambda > 400$ nm).

1.3. Effect of radical scavengers

The effect of hole and $^{\bullet}OH$ scavengers on the photochemical degradation of organic compound was also examined (Fig. 3.2.9); methanol and *tert*–butanol were used as the respective hole and $^{\bullet}OH$ scavengers. It is believed that *tert*–butanol mainly scavenges $^{\bullet}OH$, but methanol can scavenge both hole and $^{\bullet}OH$.

As shown in Fig. 3.2.9a, the addition of *tert*-butanol did not affect the degradation rate of 4-CP by S-TiO_2/Fe(III) system under visible light illumination, however, methanol affected the degradation rate of 4-CP by S-TiO_2/Fe(III) system under visible light illumination. The negligible effects of $^{\bullet}OH$ scavenger (*tert*-butanol) on 4-CP degradation also lends support to the idea that $^{\bullet}OH$ plays an insignificant role in S-TiO_2/Fe(III) system.

The degradation of benzoic acid by S-TiO_2/Fe(III)/H_2O_2 system was significantly inhibited in the presence of methanol and *tert*-butanol (Fig. 3.2.9b). The effect of $^{\bullet}OH$ scavengers (methanol and *tert*-butanol) on benzoic acid degradation lends support to the idea that $^{\bullet}OH$ plays significant role in S-TiO_2/Fe(III)/H_2O_2 system.

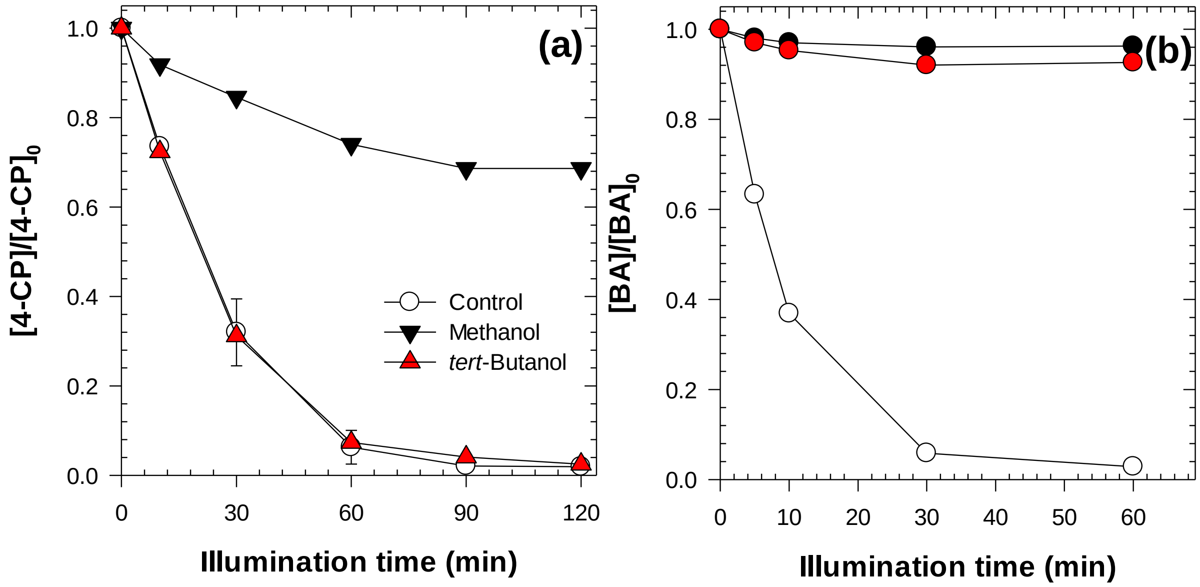

Fig. 3.2.9. Degradation of organic compounds by S-TiO_2/Fe(III) (a) and S-TiO_2/Fe(III)/H_2O_2 (b) under visible light illumination: effects ROS scavengers (([S-TiO_2] = 0.5 g/L, $[Fe(III)]_0 = 0.1$ mM, $[\text{Methanol}]_0 = [\textit{tert}\text{-Butanol}]_0 = 200$ mM, pH = 3, I = 6.43×10^{-6} Einstein/L·s (fluorescent lamp, $\lambda >$ 400 nm), $[4\text{-CP}]_0 = 10$ μM for (a), $[BA]_0 = 10$ μM for (b), $[H_2O_2]_0 = 0.1$ mM for (b)).

1.4. Oxidant production

The oxidative production of formaldehyde (HCHO), 4-hydxorybenzoic acid (4-HBA), and 7-hydroxycoumarin (7-HC) was examined under visible light illumination (Fig. 3.2.10). Methanol, benzoic acid, and coumarin were selected as probe compounds for the detection of reactive oxidant species. An excess amount of probe compounds was injected for scavenging all the generated reactive oxidant species and the major oxidized products were quantified.

As shown in Fig. 3.2.10a, the concentration of HCHO was about 60 μM in S-TiO_2/Fe(III) system under visible light illumination, whereas, the concentration of 4-HBA and 4-HC was negligibly quantified. On the other hand, the more amount of HCHO was quantified in S-TiO_2/Fe(III)/H_2O_2 system, and 4-HBA and 7-HC were detected: 9.4 μM and 4.4 μM for 4-HBA and 7-HC, respectively (Fig. 3.2.10b).

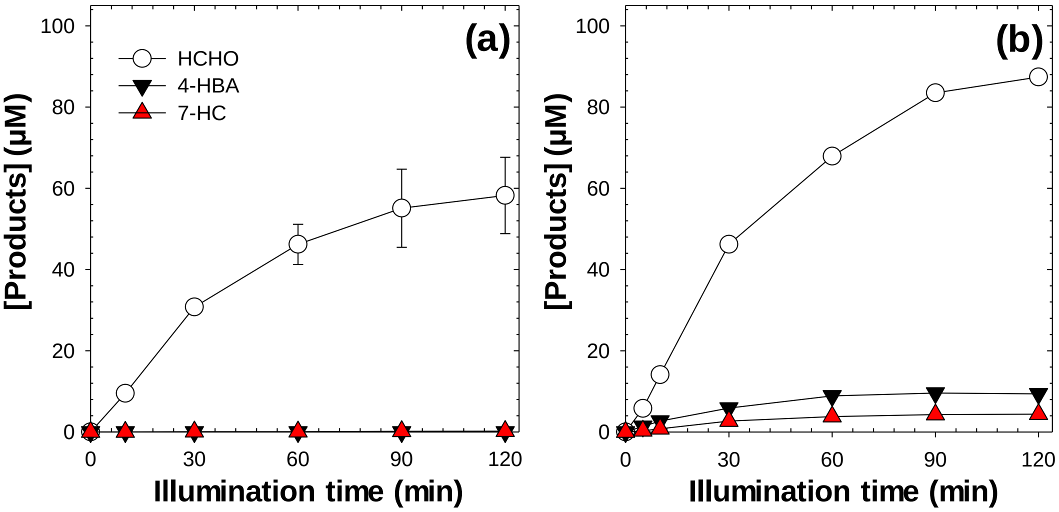

Fig. 3.2.10. Production of HCHO, 4-HBA, and 7-HC by S-TiO_2/Fe(III) (a) and S-TiO_2/Fe(III)/H_2O_2 (b) under visible light illumination ([S-TiO_2] = 0.5 g/L, $[Fe(III)]_0$ = 0.1 mM, $[Methanol]_0$ = 200 mM, $[Benzoic\ acid]_0$ = 10 mM, $[Coumarin]_0$ = 1 mM, pH = 3, $I = 6.43 \times 10^{-6}$ Einstein/L·s (fluorescent lamp, $\lambda > 400$ nm), $[H_2O_2]_0$ = 0.1 mM for (b)).

1.5. Repetition test under visible light illumination

To examine the stability of S-TiO_2, the repeated degradation of 4-CP in S-TiO_2/Fe(III) system was performed. In detail, S-TiO_2 was added once at the beginning of the photochemical experiment, and 10 μM of 4-CP was injected in every 1 h (Fig. 3.2.11a). 70% of 4-CP was degraded in the first 1 h, however, the degradation efficiency of 4-CP significantly decreased from the second cycle of photochemical reaction. It would be assumed that most of Fe(III) was reduced at the first cycle of the photochemical reaction, however, the accumulated Fe(II) could not be re-oxidized in the system, leading to the hole-electron recombination from the second cycle.

The repeated degradation of benzoic acid in S-TiO_2/Fe(III)/H_2O_2 system was also performed. In this experiment, 10 μM of benzoic acid and 0.1 mM of H_2O_2 were injected in every 1 h (Fig. 3.2.11b). S-TiO_2/Fe(III)/H_2O_2 system exhibited significant degradation of benzoic acid in each cycle. The degradation rate of benzoic acid was relatively slow in the first cycle because Fe(III) started to be reduced. From the second cycle, Fe(II), generated by photochemical reduction of Fe(III), existed at the starting point of each degradation cycle.

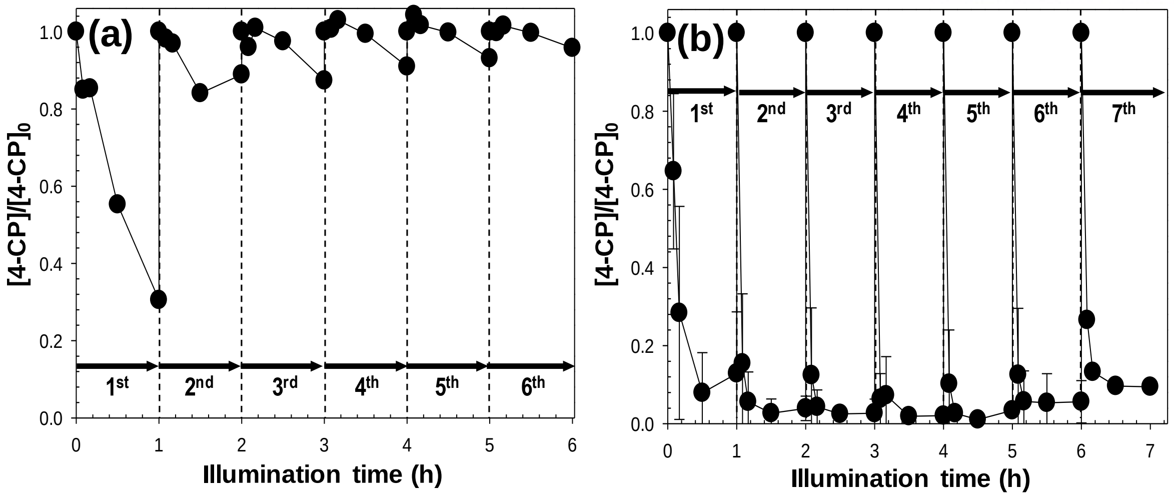

Fig. 3.2.11. Repeated degradation of 4-CP by S-TiO$_2$/Fe(III) (a) and benzoic acid by S-TiO$_2$/Fe(III)/H$_2$O$_2$ (b) under visible light illumination (([S-TiO$_2$] = 0.5 g/L, [Fe(III)]$_0$ = 0.1 mM, pH = 3, I = 6.43 × 10^{-6} Einstein/L·s (fluorescent lamp, λ > 400 nm), [4-CP]$_0$ = 10 μM for (a), [benzoic acid]$_0$ = 10 μM for (b), [H$_2$O$_2$]$_0$ = 0.1 mM for (b)).

2. Discussion

2.1 Roles of ROS

Photocatalysts generate the reactive redox species during the light illumination on the surface. The visible light illumination on the S-TiO$_2$ produces electron-hole pairs, which are further converted to $^{\bullet}$OH and superoxide radical ($O_2^{\bullet-}$). Among the photochemically generated reactive oxidant species, hole and $^{\bullet}$OH are mostly responsible for the oxidation of organic compounds [98].

The role of ROS was separated depending on the experimental systems (S-TiO$_2$/Fe(III) and S-TiO$_2$/Fe(III)/H$_2$O$_2$) in this study. The experimental results from S-TiO$_2$/Fe(III) system exhibit evidence in oppose to $^{\bullet}$OH. First, the target-selective reaction for the degradation of organic compounds cannot be generated by the oxidation reaction of $^{\bullet}$OH (Fig. 3.2.8a). Second, the hole scavenging effect for the degradation of 4-CP supports the idea that hole at the surface of S-TiO$_2$ is the main oxidant in the S-TiO$_2$/Fe(III) system (Fig. 3.2.9a). Lastly, the hydroxylated oxidation products (*p*-HBA and 7-HC) were negligibly produced by the photochemical oxidation of the respective probe compounds (BA and coumarin), which lends the last support to the insignificant role of $^{\bullet}$OH (Fig. 3.2.10a).

In contrast, the experimental results in S-TiO$_2$/Fe(III)/H$_2$O$_2$ system indicate that $^{\bullet}$OH is responsible for the degradation of organic compounds: nonselective target degradation (Fig. 3.2.8b), the $^{\bullet}$OH scavenging effect (Fig. 3.2.9b), and the generation of hydroxylated oxidation products (Fig. 3.2.10b).

2.2 Photochemical mechanisms for the degradation of organic compounds

The photochemical mechanisms of S-TiO$_2$/Fe(III) system and S-TiO$_2$/Fe(III)/H$_2$O$_2$ system are postulated in Fig. 3.2.12. In S-TiO_2/Fe(III) system, the hole oxidation reaction appears to be mainly responsible for the degradation of organic compounds. The sulfur-doping generates a mid-gap band above the valence band of TiO_2. [33] The mid-gap band narrows the bandgap energy of TiO_2, however, reduces the oxidizing power of hole reaction. In S-TiO_2/Fe(III)/H_2O_2 system, the additional reactive oxidant species are generated by the reaction with photochemically reduced Fe(II) and H_2O_2, which enhances the degradation efficiency of organic compounds.

The dissolved iron exhibited dual roles in S-TiO_2/Fe(III) system and S-TiO_2/Fe(III)/H_2O_2 system. First, Fe(III) scavenges the photochemically generated electron at the conduction band of S-TiO_2, which enhances the hole oxidation reaction by prevention of the electron-hole recombination effectively. Second, the photochemically reduced Fe(II) is used for the Fenton reaction with H_2O_2, which generates additional reactive oxidant species for the degradation of recalcitrant organic compounds.

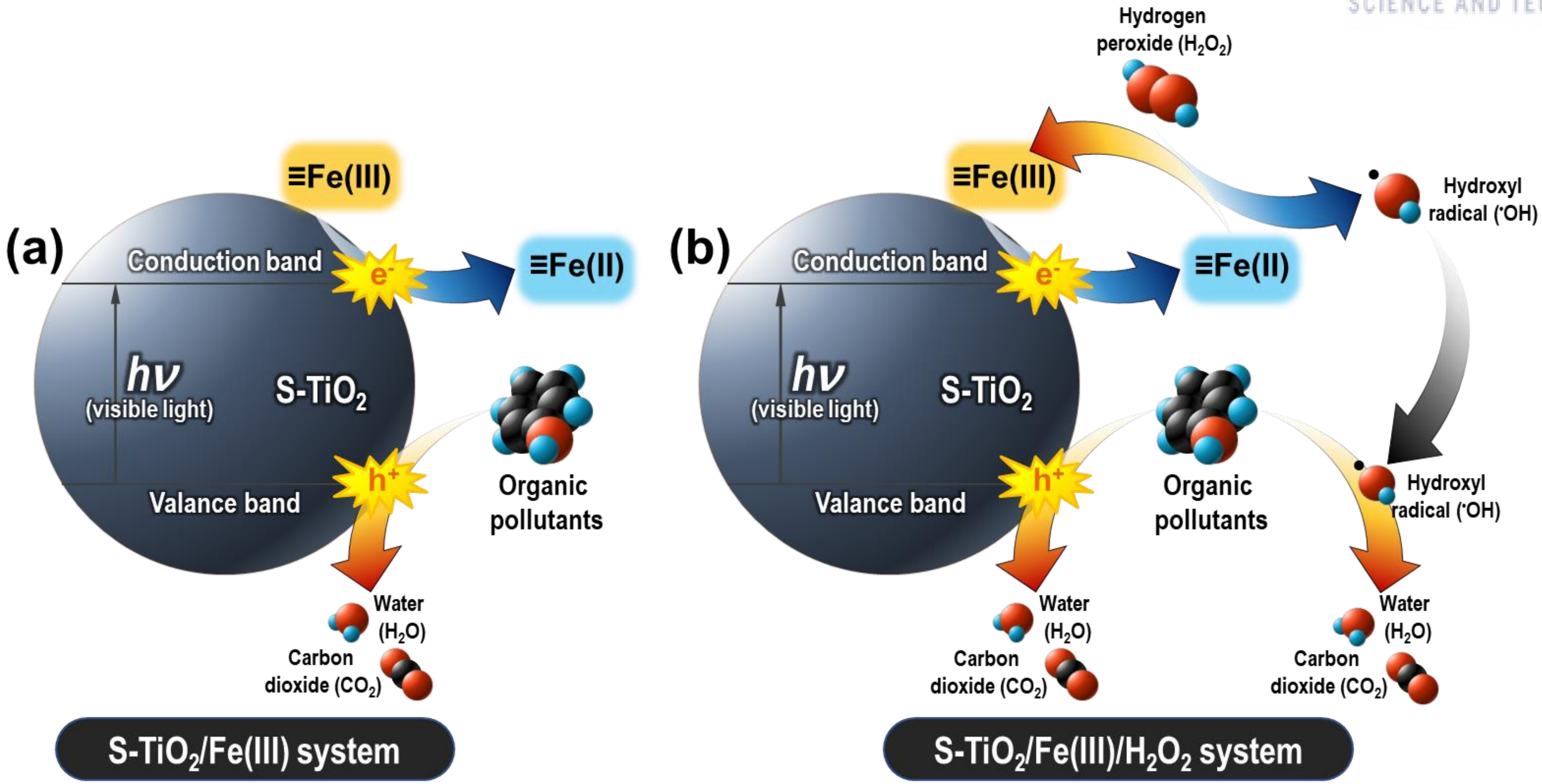
(a)
≡Fe(III)
Conduction band
e-
≡Fe(II)
hν
(visible light)
S-TiO2
Valance band
h+
Organic pollutants
Water (H2O)
Carbon dioxide (CO2)
S-TiO2/Fe(III) system
(b)
Hydrogen peroxide (H2O2)
≡Fe(III)
Hydroxyl radical (·OH)
Conduction band
e-
≡Fe(II)
hν
(visible light)
S-TiO2
Organic pollutants
Valance band
h+
Hydroxyl radical (·OH)
Water (H2O)
Carbon dioxide (CO2)
Water (H2O)
Carbon dioxide (CO2)
S-TiO2/Fe(III)/H2O2 system

Fig. 3.2.12. Photochemical reaction mechanisms for the degradation of organic compounds in S-TiO_2/Fe(III) system (a) and S-TiO_2/Fe(III)/H_2O_2 system (b).

III. Anthraquinone anchored graphitic carbon nitride (g-C_3N_4-AQ)

1. Results

1.1. Synthesis and characterization of g-C_3N_4-AQ

The XRD patterns of the synthesized g-C_3N_4 and g-C_3N_4-AQ were shown in Fig. 3.3.1a. The XRD peaks observed at 13.1° and 27.4° represented the (100) and (002) plane of graphitic materials, respectively [106]. The XRD pattern of g-C_3N_4-AQ could be completely overlapped with the pattern of g-C_3N_4, which is the evidence that the crystalline structure of g-C_3N_4-AQ was not affected by AQ.

The synthesized g-C_3N_4 and g-C_3N_4-AQ were bright yellow powders, which indicate the absorption of visible light. The diffuse reflectance spectra indicated that g-C_3N_4 and g-C_3N_4-AQ exhibited similar light absorption spectrum at the wavelength from 400 nm to 600 nm (Fig. 3.3.1b).

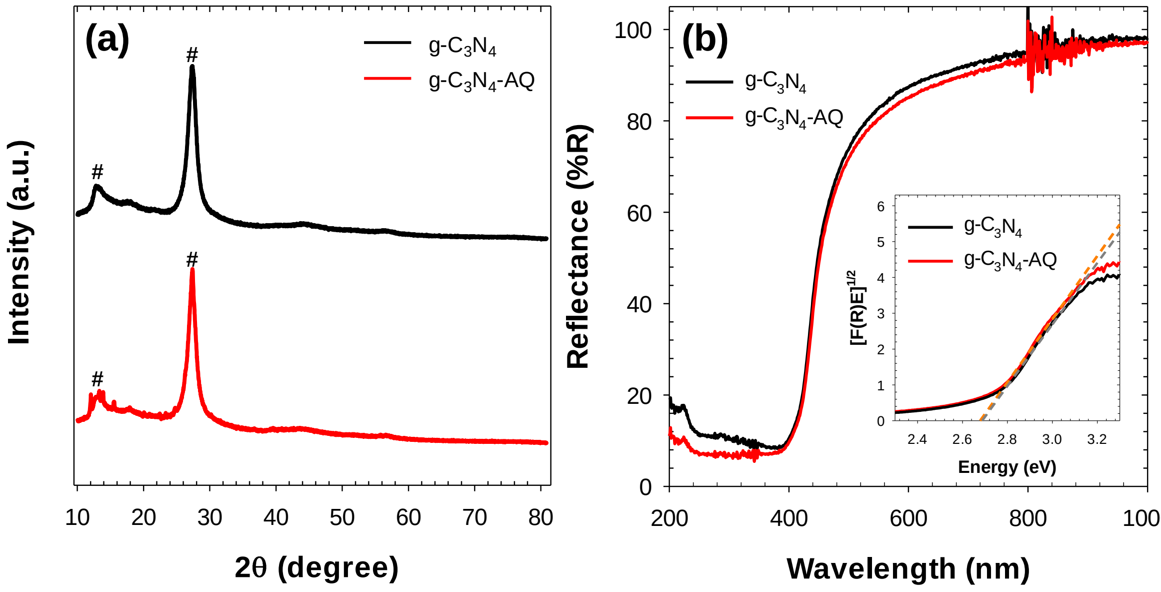

Fig. 3.3.1. X-ray diffraction patterns (a) and diffuse reflectance spectra (b)of g-C_3N_4 and g-C_3N_4-AQ.

To determine the bandgap energies of g-C_3N_4 and g-C_3N_4-AQ, modified Kubelka-Munk function was used [104,105]. The calculated bandgap energies of g-C_3N_4 and g-C_3N_4-AQ were 2.69 eV and 2.68 eV, respectively (Fig. 3.3.2a). The results of valence band XPS indicated the valence band edges of the g-C_3N_4 and g-C_3N_4-AQ. The calculated valence band edges of g-C_3N_4 and g-C_3N_4-AQ were 1.63 eV and 1.53 eV, respectively (Fig. 3.3.2b). From the basis of the calculations, the electronic band structures of g-C_3N_4 and g-C_3N_4-AQ are expressed in Fig. 3.3.2c. Both g-C_3N_4 and g-C_3N_4-AQ have enough conduction band positions for the reduction of oxygen ($E°[O_2/O_2^{\bullet-}] = -0.33\ V_{NHE}$), which indicates that g-C_3N_4 and g-C_3N_4-AQ can produce H_2O_2 by photocatalytic reduction reaction [81].

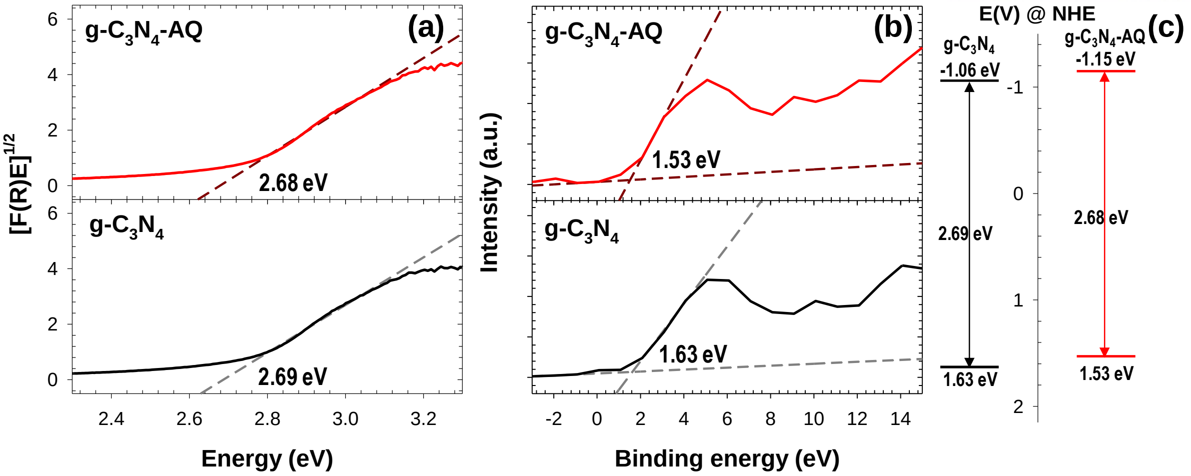

Fig. 3.3.2. Diffuse reflectance spectrum (a), valence band XPS (b), and electronic band structure (c) of g-C_3N_4 and g-C_3N_4-AQ.

The FT-IR spectra of g-C_3N_4 and g-C_3N_4-AQ were expressed in Fig. 3.3.3. The functional groups which prove the existence of g-C_3N_4 are known as the breathing mode peak of triazine unit (798 cm^{-1}), the skeletal stretching mode peak of C−N (1250 − 1420 cm^{-1}) and C=N (1550 – 1630 cm^{-1}), and –NH/NH_2 (3050 – 3400 cm^{-1}) [107,108]. The IR absorption peaks reflected AQ were also observed by C–H bending (698 cm^{-1}), C–H stretching vibration (2974 cm^{-1}), C–N stretching (1278 cm^{-1}), and carbonyl C=O stretching vibration (1676 cm^{-1}) [109-112]. The FT-IR spectrum of g-C_3N_4-AQ consists of the mixed IR absorption peak of g-C_3N_4 and AQ; the FT-IR spectrum of g-C_3N_4 was amplified by C–H bending (698 cm^{-1}), C–N stretching (1278 cm^{-1}), and carbonyl C=O stretching vibration (1676 cm^{-1}).

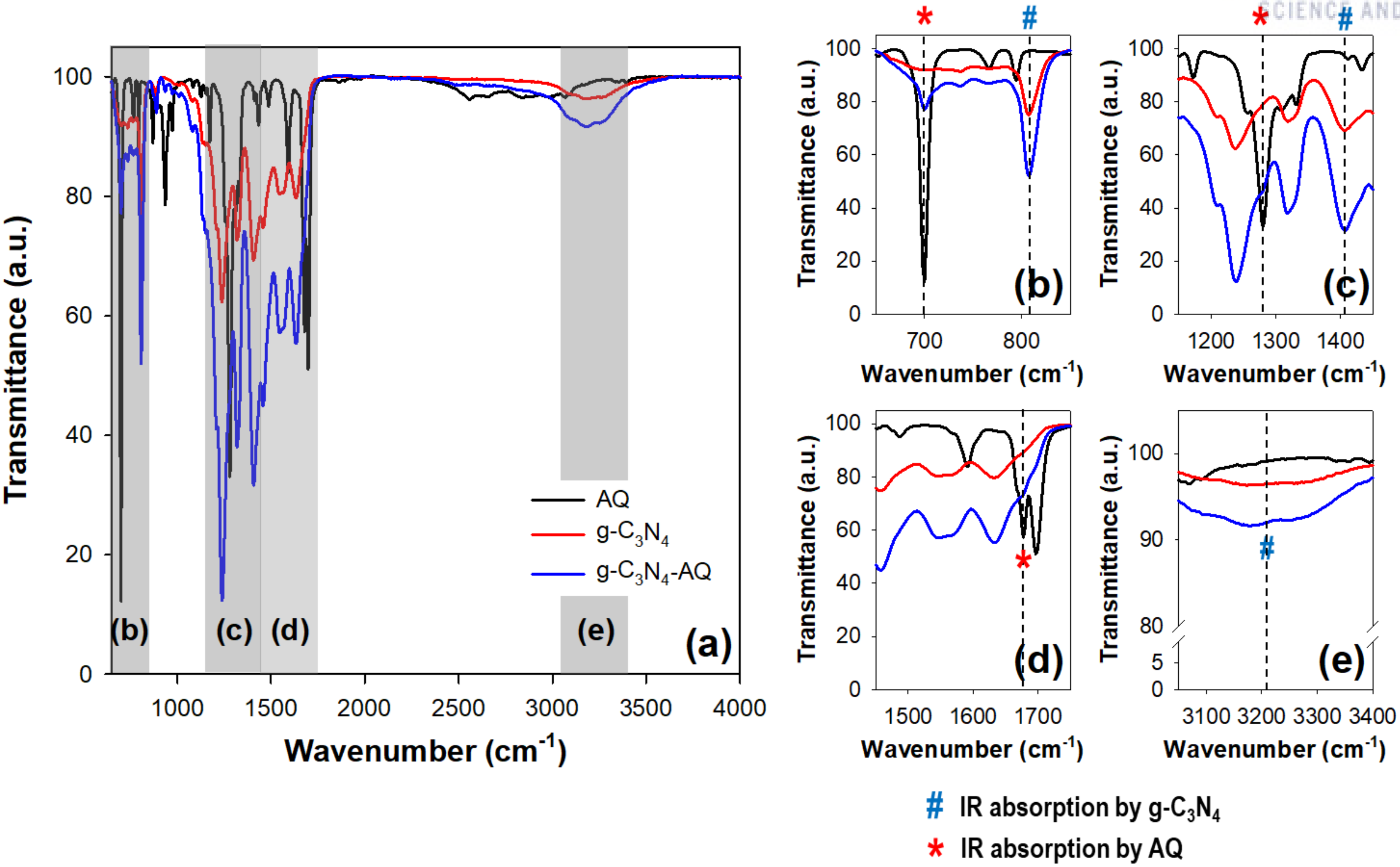

Fig. 3.3.3. FT-IR spectra of AQ, g-C_3N_4 and g-C_3N_4-AQ. Notations ‘#’ and ‘*’ in (b) – (e) represent the main IR absorption of g-C_3N_4 and AQ.

The XPS spectra of g-C_3N_4 and g-C_3N_4-AQ support the formation of a peptide bond between AQ-COOH and g-C_3N_4 in g-C_3N_4-AQ (Fig. 3.3.4). The C 1s XPS spectra of g-C_3N_4 and g-C_3N_4-AQ consisted of three binding energy: C-C peak (284.8 eV), C=C peak (287.3 eV), and N=C-N (288.2 eV) (Fig. 3.3.4a, d) [113]. In the C 1s XPS spectra, the dominant species in g-C_3N_4 were C=C and N-C=N peaks, however, the C-C peak in g-C_3N_4-AQ was amplified by the AQ (Fig. 3.3.4a, d) [113,114]. In the O 1s XPS spectrum of g-C_3N_4, the weak binding energy was observed, which emerged from the adsorbed CO_2 and H_2O on the surface of g-C_3N_4 (Fig. 3.3.4b) [115]. The O 1s XPS spectrum of g-C_3N_4-AQ revealed three binding energies (>C=O at 531.4 eV, O=C-N at 532.4 eV, and -COOH at 533.2 eV), which was attributed to the formation of a peptide bond between -COOH in AQ-COOH and -NH_2 in g-C_3N_4. (Fig. 3.3.4e) [114,116]. In the N 1s XPS spectra, the binding energies at 398.6 eV and 399.8 eV were observed, which correspond to the C=N-C and N-$(C)_3$, respectively [117]. The binding energy at 400.8 eV is attributed from the C-N-H or NHC=O, and was observed only in g-C_3N_4-AQ (Fig. 3.3.4f).

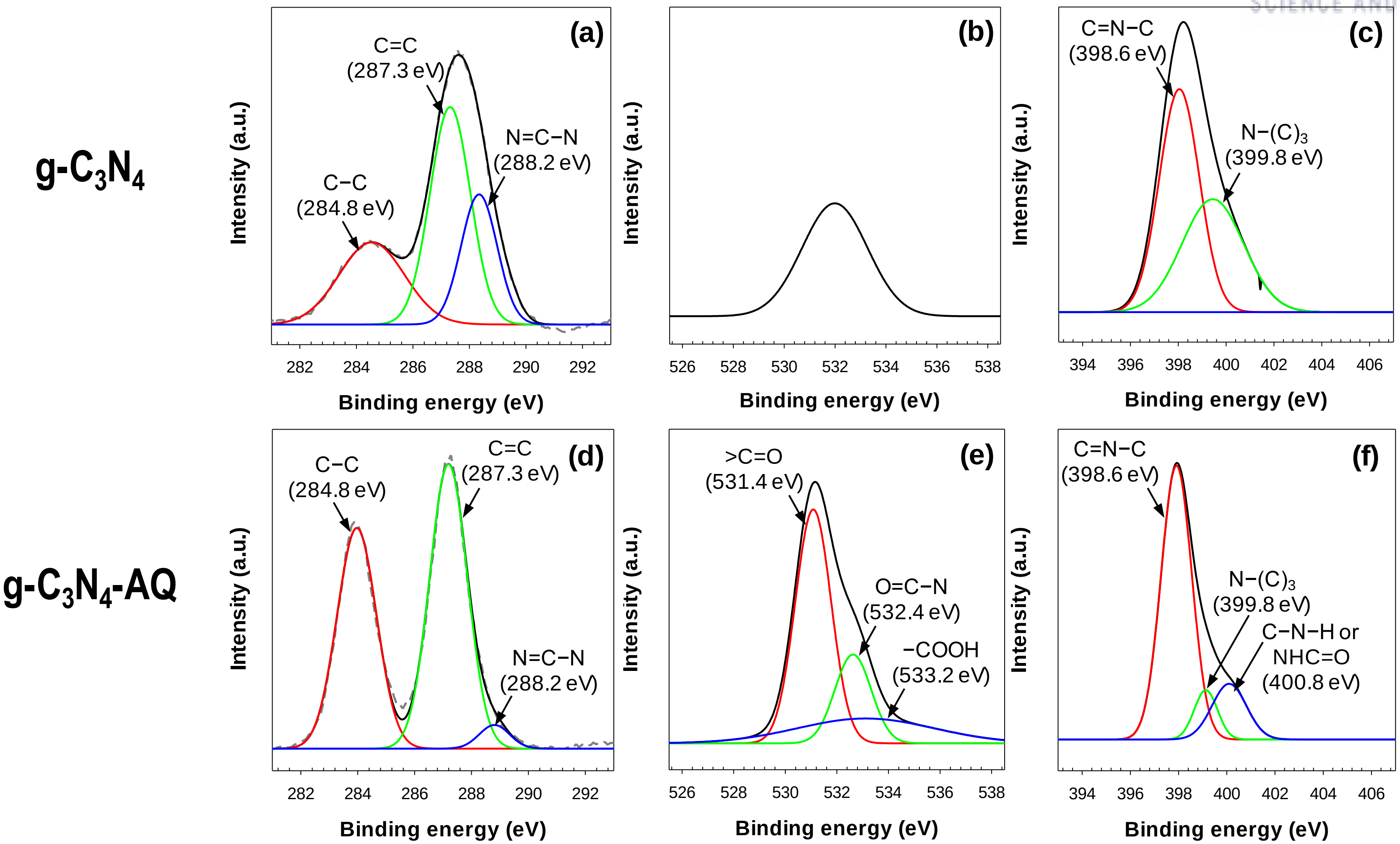

Fig. 3.3.4. X-ray photoelectron spectra (C 1s ((a) and (d)), O 1s ((b) and (e)), and N 1s ((c) and (f)) levels) of g-C_3N_4 ((a) – (c)) and g-C_3N_4-AQ ((d) –(f)).

1.2. Photochemical reaction of g-C_3N_4-AQ

Production of H_2O_2 by g-C_3N_4-AQ and the respective controls (AQ, g-C_3N_4, and g-C_3N_4/AQ) were examined under dark and visible light illumination condition (Fig. 3.3.5). In dark condition, all systems negligibly produced H_2O_2 in 2 h (Fig. 3.3.5a). In contrast, g-C_3N_4/AQ could produce 8 µM of H_2O_2 and g-C_3N_4-AQ could also produce 12 µM of H_2O_2 in 2 h under visible light illumination (Fig. 3.3.5b).

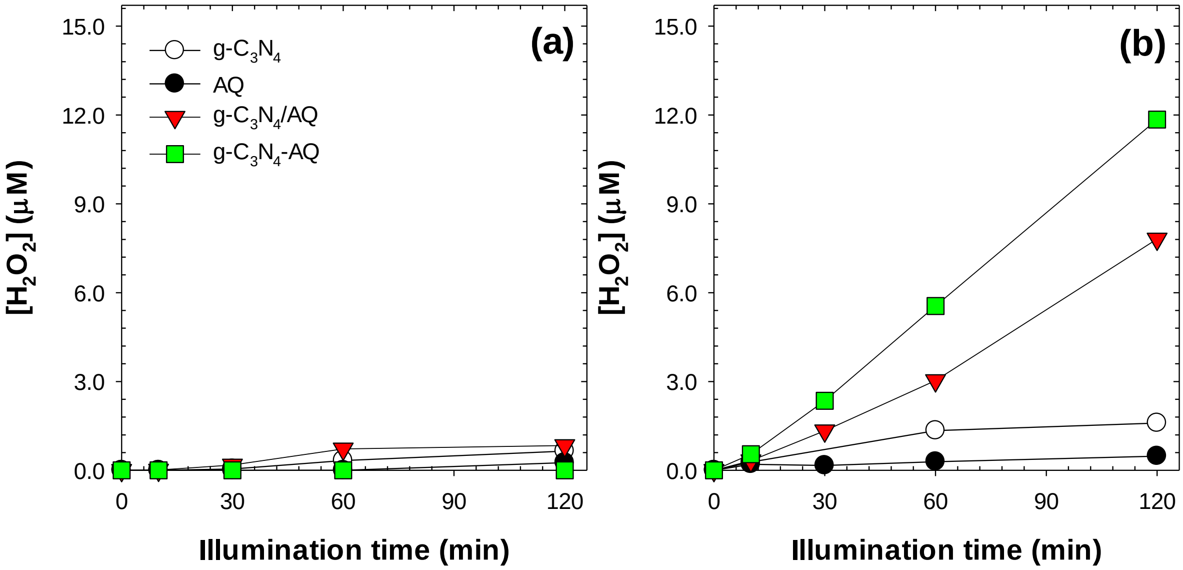

Fig. 3.3.5. Production of H_2O_2 by photocatalytic systems under visible light illumination: Dark condition (a) and light illumination condition (b) ([Catalyst] = 0.5 g/L, pH=3, Xenon lamp (150 W, λ > 400 nm) for (b)).

Degradation of benzoic acid by visible light illuminated g-C_3N_4-AQ system and the respective control systems (AQ, g-C_3N_4, and g-C_3N_4-AQ) were examined in the absence and presence of Fe(III) (Fig. 3.3.6). The degradation of benzoic acid was negligible in the AQ, g-C_3N_4, g-C_3N_4/AQ, and g-C_3N_4-AQ systems under visible light illumination (Fig. 3.3.6a). The degradation of benzoic acid was minor in the visible light illuminated AQ/Fe(III) and g-C_3N_4/Fe(III) under visible light illumination: 17% and 27% for AQ and g-C_3N_4, respectively (Fig. 3.3.6b). Meanwhile, 50% of benzoic acid was degraded by g-C_3N_4/AQ/Fe(III) system and g-C_3N_4-AQ/Fe(III) could degrade 88% of benzoic acid in 2 h under visible light illumination (Fig. 3.3.6b).

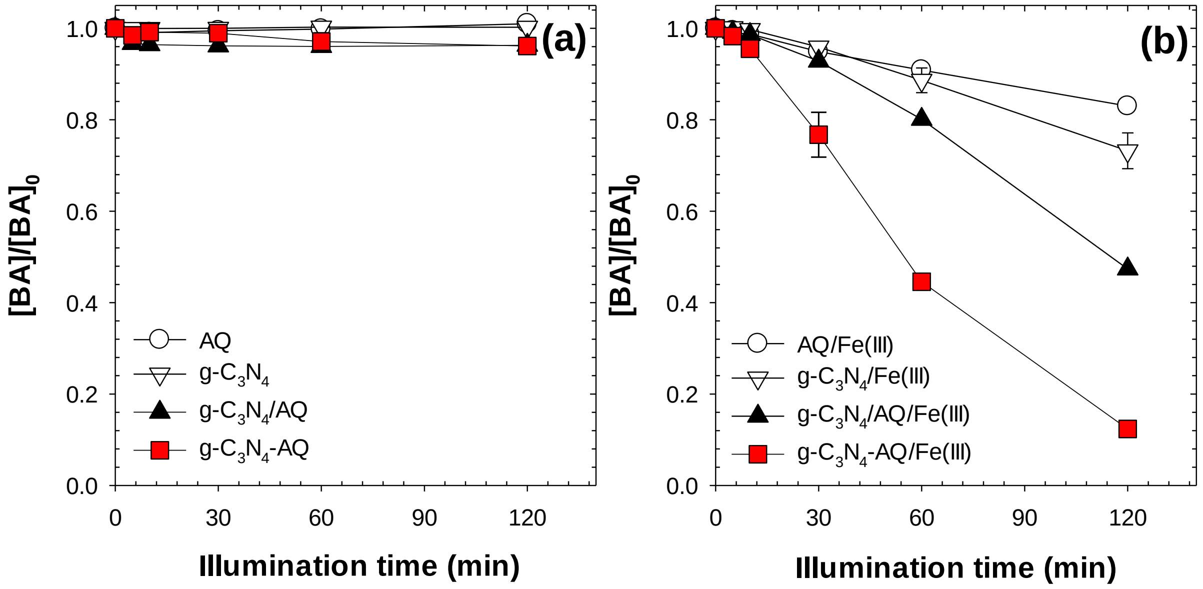

Fig. 3.3.6. Degradation of BA by photocatalytic systems under visible light illumination: In the absence of Fe(III) (a) and in the presence of Fe(III) (b) ([Catalyst] = 0.5 g/L, $[BA]_0$ = 10 μM, pH=3, Xenon lamp (150 W, λ > 400 nm), $[Fe(III)]_0$ = 0.1 mM for (b)).

1.3. Effect of AQ loading and Fe(III) injection

To confirm the effect of AQ loading, different varieties of g-C_3N_4-AQ were prepared as the varied dosage of AQ (for the formation of peptide bond), and then the degradation of benzoic acid by g-C_3N_4-AQ/Fe(III) was investigated under visible-light illumination (Fig. 3.3.7). The pseudo-first order rate for the degradation of benzoic acid was gradually increased up to 5wt% dosage of AQ and the rapid acceleration of benzoic acid degradation was observed at 10wt% dosage of AQ. The drastic decrease of reaction rate for the degradation of benzoic acid was observed when the 20wt% of AQ was dosed in the synthetic condition.

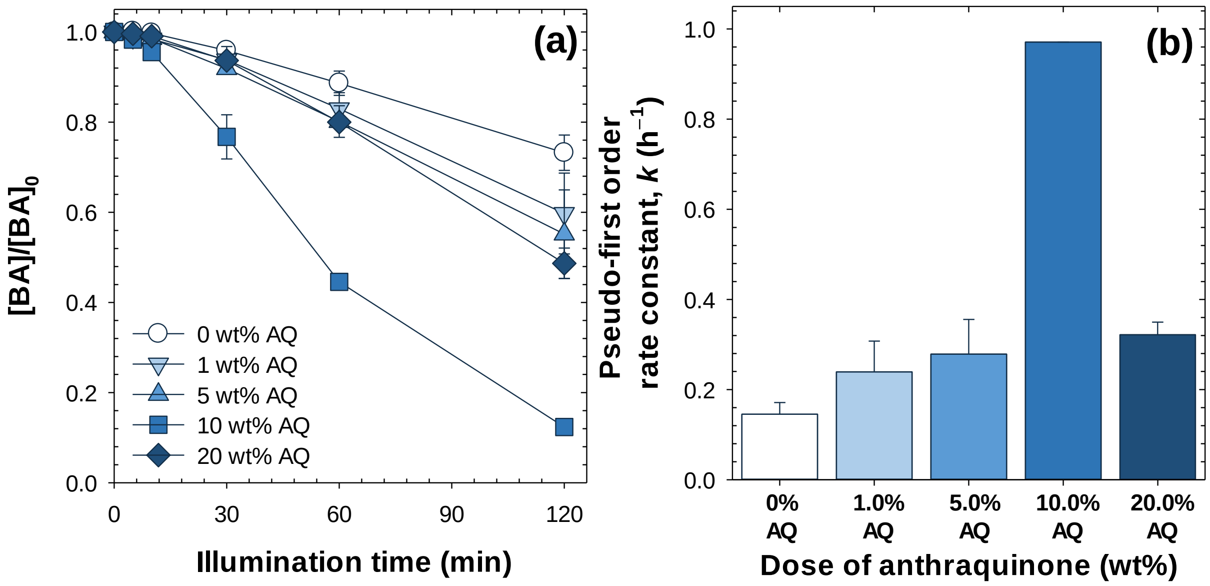

Fig. 3.3.7. Degradation of benzoic acid (a) and pseudo-first order rate constant of benzoic acid degradation (b) by varied g-C_3N_4-AQ/Fe(III) systems under visible light illumination: As dose of AQ ([g-C_3N_4-AQ] = 0.5 g/L, $[BA]_0$ = 10 μM, $[Fe(III)]_0$ = 0.1 mM, pH=3, Xenon lamp (150 W, $\lambda > 400$ nm)).

The effect of Fe(III) for the degradation of benzoic acid in g-C_3N_4-AQ/Fe(III) system was investigated using varying concentration of Fe(III) (Fig. 3.3.8). The degradation efficiency of benzoic acid significantly increased as the injection of Fe(III) (Fig. 3.3.8a). The pseudo-first order rate for the degradation of benzoic acid observed similar trends at the 0.01 mM to 0.05 mM of Fe(III) dosage and was maximized at the 0.1 mM of Fe(III) (Fig. 3.3.8b). The degradation rate rapidly decreased when the initial concentration of Fe(III) increased to 0.2 mM, which might be attributed to the precipitation of iron oxyhydroxides on the g-C_3N_4-AQ surface (Fig. 3.3.8b).

The reduction of Fe(III) was observed while the benzoic acid was degraded by the g-C_3N_4-AQ/Fe(III) system (Fig. 3.3.8c). The photochemical reaction of g-C_3N_4-AQ completely reduced Fe(III) in the 0.01 mM of Fe(III) dosage condition. The reduction of Fe(III) approached 60% at the 0.02 to 0.1 mM of Fe(III) dosage and significantly decreased up to 25% at the 0.2 mM of Fe(III) dosage.

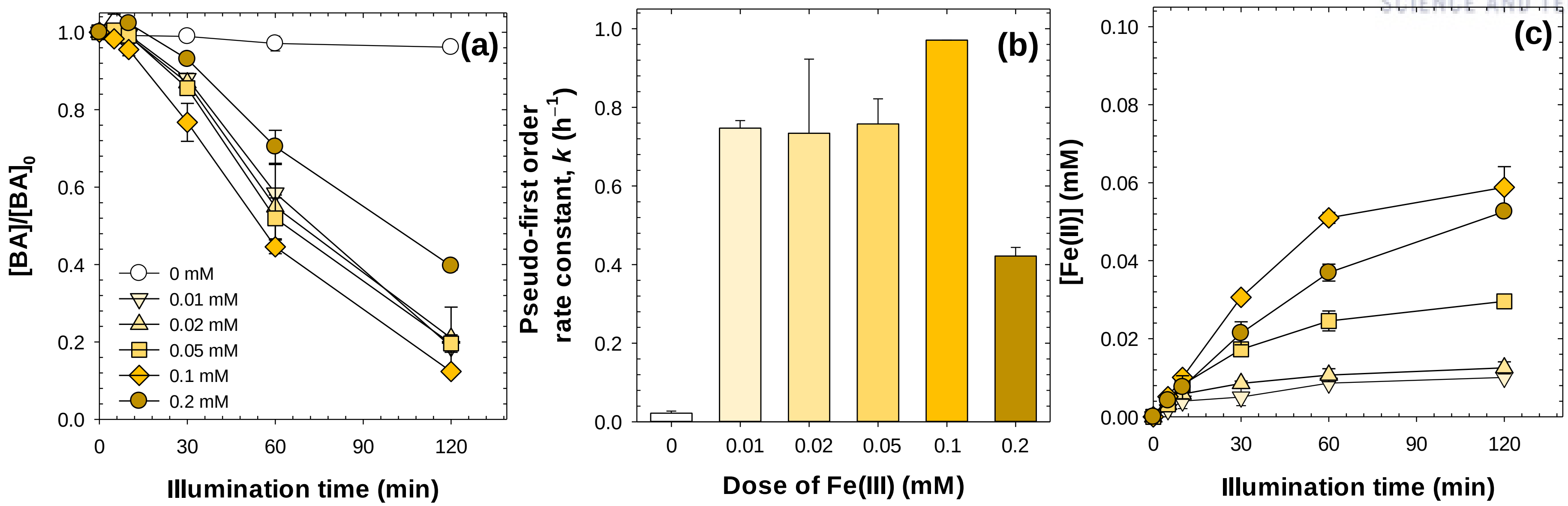

Fig. 3.3.8. Degradation of benzoic acid (a), pseudo-first order rate constant of benzoic acid degradation (b) and reduction of Fe(III) (c) by varied g-C_3N_4-AQ/Fe(III) systems under visible light illumination: As dose of Fe(III) ([g-C_3N_4-AQ] = 0.5 g/L, $[BA]_0$ = 10 μM, pH=3, Xenon lamp (150 W, λ > 400 nm)).

1.4. Photochemical degradation of various organic compounds

Photochemical degradation of various organic compounds (phenol, 4–CP, BA, and CBZ) was examined in g-C_3N_4-AQ/Fe(III) system under visible light illumination (Fig. 3.3.9). To confirm the effect of dissolved oxygen in g-C_3N_4-AQ/Fe(III) system, the photochemical degradation of organic compounds was conducted under air-saturated and deaerated condition.

In air-saturated condition, all the selected target organic compounds were effectively degraded by g-C_3N_4-AQ/Fe(III) system under visible light illumination (Fig. 3.3.9a). The degradation rate of phenol was the greatest (k_{Phenol} = 4.75 h^{-1}), which was followed by those of 4-CP, carbamazepine, and benzoic acid ($k_{\mathrm{4\text{-}CP}}$ = 4.63 h^{-1}, k_{CBZ} = 1.65 h^{-1}, and k_{BA} = 0.97 h^{-1}).

In deaerated condition, phenol and 4-CP were effectively degraded by g-C_3N_4-AQ/Fe(III) system under visible light illumination (k_{Phenol} = 1.58 h^{-1} and $k_{\mathrm{4\text{-}CP}}$ = 1.35 h^{-1}) (Fig. 3.3.9b). However, CBZ was resisted to the photochemical degradation by g-C_3N_4-AQ/Fe(III) and benzoic acid was hardly degraded (k_{CBZ} = 0.29 h^{-1}).

The reduction of Fe(III) was monitored while the target organic compounds were degraded by the g-C_3N_4-AQ/Fe(III) system (Fig. 3.3.9c, d). In air-saturated condition, 60% of Fe(III) was reductively converted to Fe(II) in 2 h while the selected target organic compounds were degraded, which is double amount in the photochemical reduction of Fe(III) without target organic compound (Fig. 3.3.9c). In deaerated condition, the reduction of Fe(III) during the degradation of organic compounds is consistent with the degradation of organic compounds: w/o target compounds < BA < CBZ < 4-CP < phenol (Fig. 3.3.9d).

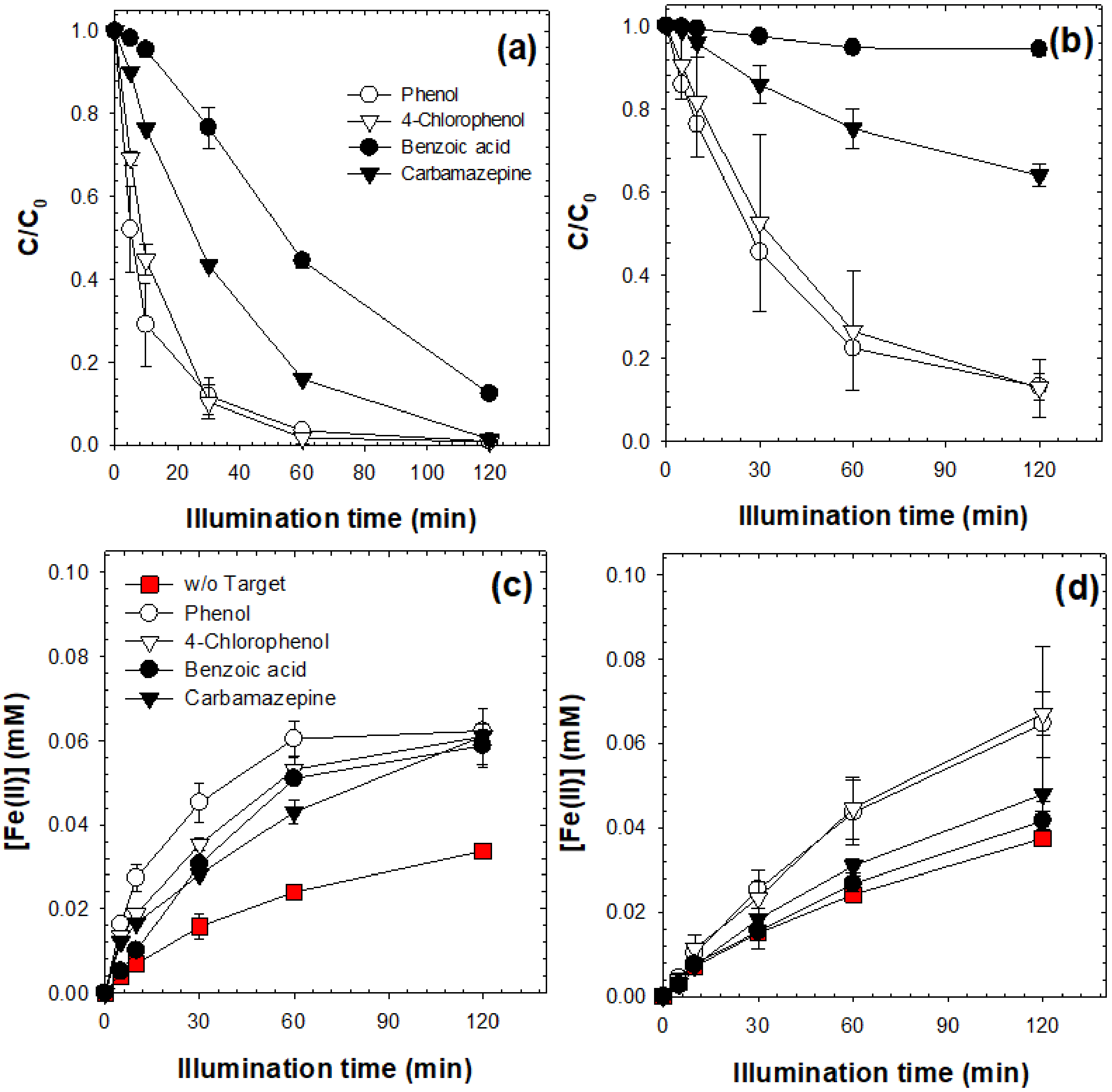

Fig. 3.3.9. Degradation of organic compounds ((a) and (b)) and reduction of Fe(III) ((c) and (d)) by g-C_3N_4-AQ/Fe(III) systems under visible light illumination: air saturation ((a) and (c)) and deaeration ((b) and (d)) condition ([g-C_3N_4-AQ] = 0.5 g/L, $[\text{Phenol}]_0 = [\text{4-CP}]_0 = [\text{BA}]_0 = [\text{CBZ}]_0 = 10\ \mu\text{M}$, $[\text{Fe(III)}]_0 = 0.1$ mM, pH=3, Xenon lamp (150 W, $\lambda > 400$ nm), N_2 gas sparging for (b)).

1.5. Effect of ROS scavengers

The effect of ROS scavengers on the photochemical degradation of organic compound was also examined (Fig. 3.3.10); methanol and *tert*–butanol were used as the respective hole and $^{\bullet}$OH scavengers. It is believed that *tert*–butanol mainly scavenges $^{\bullet}$OH, and methanol scavenge both hole and $^{\bullet}$OH.

In air-saturated condition, the degradation of benzoic acid by g-C_3N_4-AQ/Fe(III) system was significantly interrupted by the addition of methanol and *tert*-butanol (Fig. 3.3.10a). The effect of $^{\bullet}$OH scavengers (methanol and *tert*-butanol) on benzoic acid degradation lends support to the idea that $^{\bullet}$OH plays significant role in g-C_3N_4-AQ/Fe(III) system under air-saturated condition.

In deaerated condition, the degradation of phenol by g-C_3N_4-AQ/Fe(III) system was hardly affected in the scavenging effect of *tert*-butanol under visible light illumination, however, methanol affected the degradation of phenol in g-C_3N_4-AQ/Fe(III) system under visible light illumination (Fig. 3.3.10b). In deaerated condition, $^{\bullet}$OH plays an insignificant role in g-C_3N_4-AQ/Fe(III) system due to the negligible effect of $^{\bullet}$OH scavenger (*tert*-butanol) on phenol degradation.

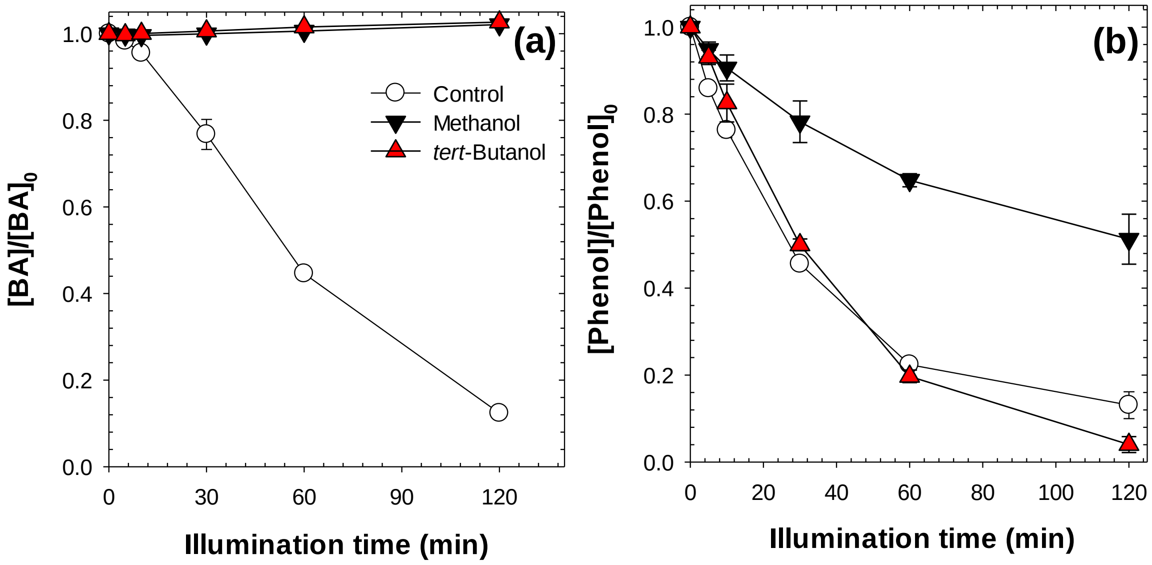

Fig. 3.3.10. Degradation of organic compounds by g-C_3N_4-AQ/Fe(III) in the presence of ROS scavengers under visible light illumination: air saturation (a) and deaeration (b) condition (([g-C_3N_4-AQ] = 0.5 g/L, $[Fe(III)]_0$ = 0.1 mM, pH = 3, Xenon lamp (150 W, $\lambda > 400$ nm), $[BA]_0$ = 10 μM for (a), $[Methanol]_0$ = [*tert*-Butanol]$_0$ = 200 mM for (a), $[phenol]_0$ = 10 μM for (b), $[Methanol]_0$ = [*tert*-Butanol]$_0$ = 1 M for (b), N_2 gas sparging for (b)).

1.6. Oxidant production

The oxidative production of HCHO, 4-HBA, and 7-HC was investigated under visible light illumination (Fig. 3.3.11). Probe compounds (methanol, benzoic acid, and coumarin) were selected for the detection of ROS and the major oxidized products were quantified.

As shown in Fig. 3.3.11a, The production of HCHO, 4-HBA, and 7-HC was monitored in visible light illuminated g-C_3N_4-AQ/Fe(III) system under air-saturated condition: 198 μM, 11 μM, and 27 μM for HCHO, 4-HBA, and 7-HC, respectively. On the other hand, 58 μM of HCHO was quantified in visible light illuminated g-C_3N_4-AQ/Fe(III) system under deaerated condition, whereas, 4-HBA and 7-HC were negligibly detected (Fig. 3.2.11b).

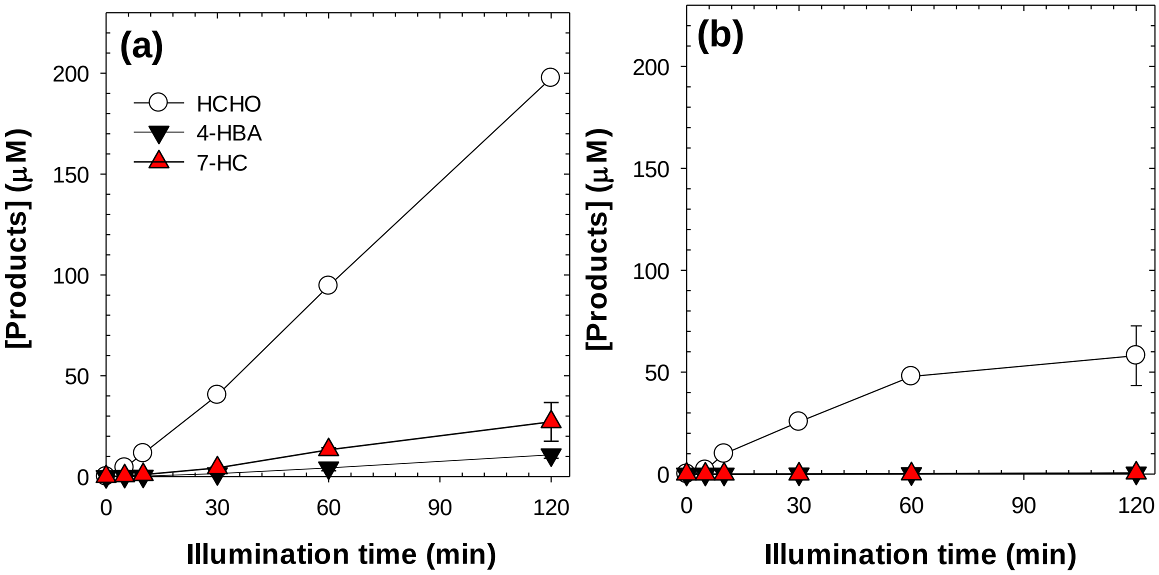

Fig. 3.3.11. Production of HCHO, 4-HBA, and 7-HC by g-C_3N_4-AQ/Fe(III) under visible light illumination: air saturation (a) and deaeration (b) condition (([g-C_3N_4-AQ] = 0.5 g/L, $[Fe(III)]_0 = 0.1$ mM, $[Methanol]_0 = 200$ mM, $[Benzoic\ acid]_0 = 10$ mM, $[Coumarin]_0 = 1$ mM, pH = 3, Xenon lamp (150 W, $\lambda > 400$ nm), N_2 gas sparging for (b)).

2. Discussion

2.1 Roles of ROS

The role of ROS in g-C_3N_4-AQ/Fe(III) system was separately investigated depending on the existence of dissolved oxygen. In air-saturated condition, the experimental results indicate that $^{\bullet}OH$ is responsible for the degradation of organic compounds. First, the non-selective degradation of organic compounds supports $^{\bullet}OH$ as the main ROS in visible light illuminated g-C_3N_4-AQ/Fe(III) (Fig. 3.3.9a). Second, the degradation of benzoic acid was interrupted by the $^{\bullet}OH$ scavengers (Fig. 3.3.10a). Lastly, the hydroxylated oxidation products (*p*-HBA and 7-HC) were produced by the photochemical oxidation of the respective probe compounds (BA and coumarin), which indicates the significant role of $^{\bullet}OH$ (Fig. 3.3.11a).

In contrast, visible light illuminated g-C_3N_4-AQ/Fe(III) system under deaerated condition showed evidence that the role of $^{\bullet}OH$ could be excluded for the degradation of organic compounds: target selective degradation (Fig. 3.3.9b), the hole scavenging effect (Fig. 3.3.10b), and the rare production of hydroxylated oxidation products (Fig. 3.3.11b).

2.2 Photochemical mechanisms for the degradation of organic compounds

The photochemical mechanism of g-C_3N_4-AQ/Fe(III) system in accordance with dissolved oxygen is suggested in Fig. 3.3.12. g-C_3N_4-AQ exhibited triple roles for the photochemical oxidation of organic compounds. First, hole generated at the valence band of g-C_3N_4-AQ oxidizes organic compounds selectively. Second, the dissolved oxygen on the g-C_3N_4-AQ surface is reduced to H_2O_2, which involves the photochemical hydrogenation of AQ and the auto-oxidation of hydrogenated AQ. [81] Lastly, Fe(III) homogeneously dispersed in g-C_3N_4-AQ/Fe(III) system is reductively converted to Fe(II), which can be further utilized with the photochemically generated H_2O_2.

The dissolved iron exhibited dual roles in g-C_3N_4-AQ/Fe(III) system. First, Fe(III) scavenges the photochemically generated electron at the conduction band of g-C_3N_4-AQ, which enhances the hole oxidation reaction by prevention of the electron-hole recombination effectively. Second, the photochemically reduced Fe(II) is used for the Fenton reaction with H_2O_2, which generates additional reactive oxidant species for the degradation of recalcitrant organic compounds.

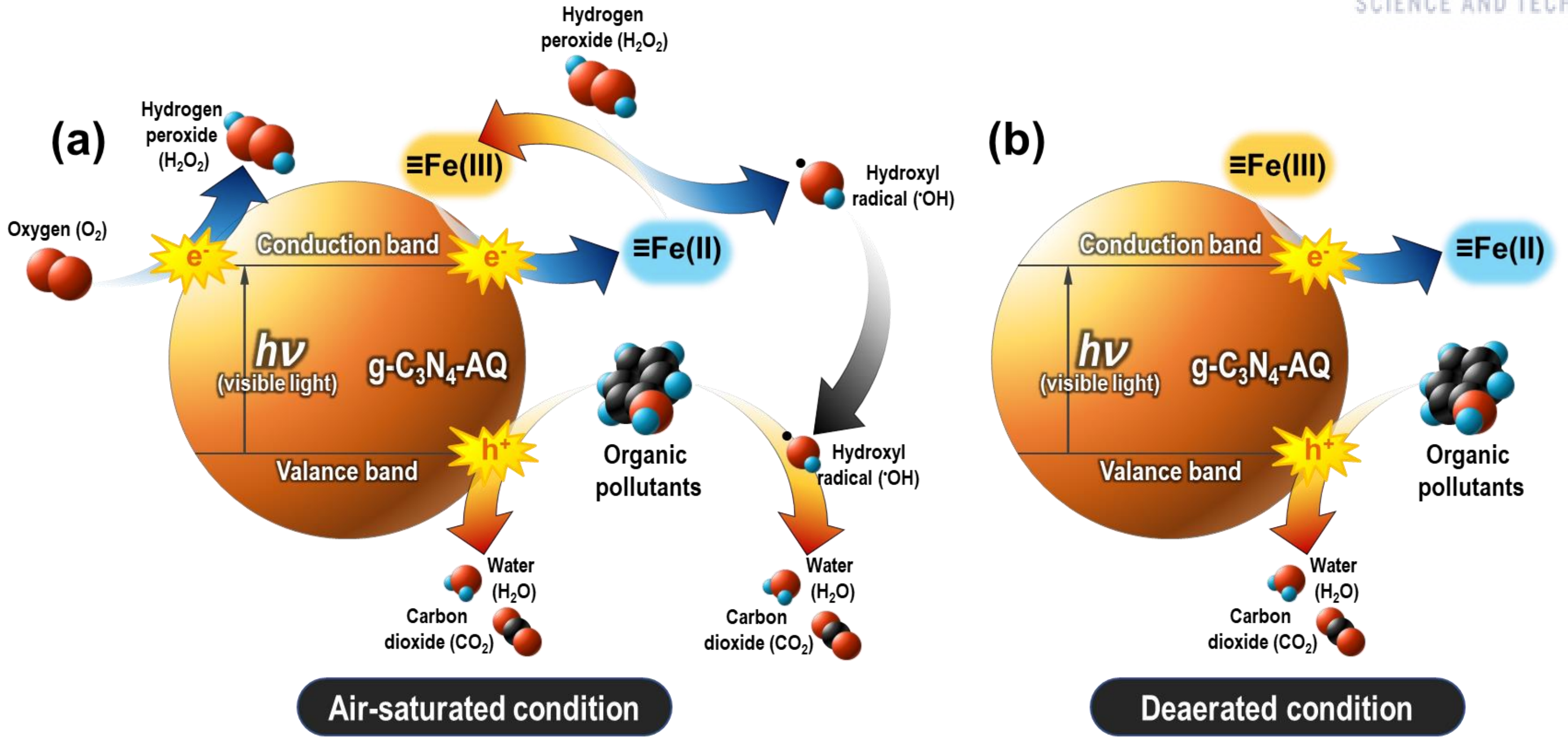
(a)
Hydrogen peroxide (H_2O_2)
Oxygen (O_2)
e⁻
Hydrogen peroxide (H_2O_2)
≡Fe(III)
Hydroxyl radical (•OH)
Conduction band
e⁻
≡Fe(II)
hν (visible light)
g-C_3N_4-AQ
Organic pollutants
h⁺
Valance band
Hydroxyl radical (•OH)
Water (H_2O)
Carbon dioxide (CO_2)
Water (H_2O)
Carbon dioxide (CO_2)
Air-saturated condition
(b)
≡Fe(III)
Conduction band
e⁻
≡Fe(II)
hν (visible light)
g-C_3N_4-AQ
Organic pollutants
h⁺
Valance band
Water (H_2O)
Carbon dioxide (CO_2)
Deaerated condition

Fig. 3.3.12. Photochemical reaction mechanisms for the degradation of organic compounds in g-C_3N_4-AQ/Fe(III) system in air-saturated (a) and deaerated (b) condition.

CHAPTER 4. CONCLUSIONS

This study investigated the photochemical degradation of various organic compounds by the visible light active photocatalysis (Am-peroxo-TiO_2) and hybrid photocatalytic systems (S-TiO_2/Fe(III), S-TiO_2/Fe(III)/H_2O_2, and g-C_3N_4-AQ/Fe(III)) in terms of the kinetics and oxidation mechanism. The experimental results of this study provide new approaches in the visible light active photocatalysis for the effective degradation of organic compounds. The major conclusions for each topic are presented as follows.

A novel visible light responsive photosensitizer (Am-peroxo-TiO_2) was synthesized by a facile method using titanium isopropoxide and H_2O_2 under mild conditions. Am-peroxo-TiO_2 was found to form aggregates of small amorphous titania nanoparticles with surface peroxo complexes. Am-peroxo-TiO_2 exhibited excellent but selective photochemical activity in degrading select organic compounds. Importantly, the roles of ROS such as $^{\bullet}OH$ and $O_2^{\bullet-}$ were found to be insignificant. Photogenerated reactive intermediates on the surface (i.e., $[\equiv Ti^{IV}–^{\bullet}OOH]^+$ and $[\equiv Ti^{III}–OOH]^-$) may be responsible for the degradation of select organic compounds. These reactive species are assumed to oxidize 4-CP via a series of electron abstraction and hydroxylation reactions. In the absence of any organic compounds, Am-peroxo-TiO_2 was stable under both dark and illuminated conditions. However, both light illumination and the presence of organic compounds gradually destroyed the surface peroxo complexes of Am-peroxo-TiO_2, causing a decrease in its photochemical activity. To counter this, Pt-loading was found to be an effective method to enhance the photostability and photochemical activity of Am-peroxo-TiO_2.

S-TiO_2 was synthesized by a sol-gal method using sulfuric acid as a sulfur-doping agent. The synthesized S-TiO_2 showed mixed crystalline phases of anatase and rutile, and 50 nm of crystalline morphology was observed in HRTEM image. The FT-IR spectra and XRF method revealed the sulfur doping on the surface of S-TiO_2. In the visible light-illuminated S-TiO_2/Fe(III) system, the oxidation by photogenerated holes appears to be mainly responsible for the degradation of organic compounds. The idea was supported by (1) the target selective degradation of organic compounds, (2) the effective interruption of hole scavenger in the degradation of 4-CP, and (3) the rare production of hydroxylated oxidation products. On the other hand, $^{\bullet}OH$ in S-TiO_2/Fe(III)/H_2O_2 plays the main role for the degradation of organic compounds.

g-C_3N_4-AQ was prepared by the sequential synthesis: thermal polymerization of dicyandimaine and formation of peptide bond. The AQ coupling, observed in the FT-IR and XPS spectra, does not affect the crystalline structure and visible light absorptivity in g-C_3N_4-AQ comparing with pristine g-C_3N_4. The combined system of photochemical H_2O_2 production and Fenton-like reaction examined oxidation efficacy of various organic compounds. g-C_3N_4-AQ/Fe(III) exhibited effective photochemical activity for oxidation of various organic compounds in the presence of dissolved oxygen because the photochemically generated H_2O_2 leads to Fenton-like reaction (Fe(III)/H_2O_2), which enhanced oxidation of organic compounds. In the absence of dissolved oxygen, hole at the surface of g-C_3N_4-AQ affected the oxidation of target organic compounds, selectively.

REFERENCES

[1] S. Zhang, Q. Zhang, S. Darisaw, O. Ehie, G. Wang, Simultaneous quantification of polycyclic aromatic hydrocarbons (PAHs), polychlorinated biphenyls (PCBs), and pharmaceuticals and personal care products (PPCPs) in Mississippi river water, in New Orleans, Louisiana, USA, *Chemosphere*, 2007, 66, 1057-1069.

[2] S.K. Behera, H.W. Kim, J.-E. Oh, H.-S. Park, Occurrence and removal of antibiotics, hormones and several other pharmaceuticals in wastewater treatment plants of the largest industrial city of Korea, *Sci. Total Environ.*, 2011, 409, 4351-4360.

[3] P.R. Gogate, A.B. Pandit, A review of imperative technologies for wastewater treatment I: oxidation technologies at ambient conditions, *Adv. Environ. Res.*, 2004, 8, 501-551.

[4] S.-Y. Pang, J. Jiang, J. Ma, S.-Y. Pang, F. Ouyang, New insight into the oxidation of arsenite by the reaction of zerovalent iron and oxygen. comment on “pH dependence of Fenton reagent generation and As(III) oxidation and removal by corrosion of zero valent iron in aerated water”, *Environ. Sci. Technol.*, 2009, 43(10), 3978-3979.

[5] K. Ikehata, M.G. El-Din, Aqueous pesticide degradation by ozonation and ozone-based advanced oxidation processes: a review (part I), *Ozone-Sci. Eng.*, 2005, 27, 83-114.

[6] K. Ikehata, M.G. El-Din, Aqueous pesticide degradation by ozonation and ozone-based advanced oxidation processes: a review (part II), *Ozone-Sci. Eng.*, 2005, 27, 173-202.

[7] F. Wang, D.W. Smith, M.G. El-Din, Application of advanced oxidation methods for landfill leachate treatment-a review, *J. Environ. Eng. Sci.*, 2003, 2(6), 413-427.

[8] K. Ikehata, M.G. El-Din, Aqueous pesticide degradation by hydrogen peroxide/ultraviolet irradiation and Fenton-type advanced oxidation processes: a review, *J. Environ. Eng. Sci.*, 2006, 5(2), 81-135.

[9] J.J. Pignatello, E. Oliveros, A. MacKay, Advanced oxidation processes for organic contaminant destruction based on the Fenton reaction and related chemistry, *Crit. Rev. Environ. Sci. Technol.*, 2006, 36, 1-84.

[10] E. Neyens, J. Baeyens, A review of classic Fenton’s peroxidation as an advanced oxidation technique, *J. Hazard. Mater.*, 2003, 98, 33-50.

[11] R. Aplin, T.D. Waite, Coparison of three advanced oxidation processes for degradation of textile dyes, *Water Sci. Technol.*, 2000, 42, 345-354.

[12] K. Vinodgopal, J. Peller, Hydroxyl radical-mediated advanced oxidation processes for textile dyes: a comparison of the radiolytic and sonolytic degradation of the monoazo dye Acid Orange 7, *Res. Chem. Intermed.*, 2003, 29, 307-316.

[13] I. Gültekin, N.H. Ince, Synthetic endocrine disruptors in the environment and water remediation by advanced oxidation processes, *J. Environ. Manage.*, 2007, 85, 816-832.

[14] K. demeestere, J. Dewulf, H. Van Langenhove, Heterogeneous photocatalysis as an advanced oxidation process for the abatement of chlorinated, monocyclic aromatic and sulfurous volatile organic compounds in air: state of the art, *Crit. Rev. Environ. Sci. Technol.*, 2007, 37, 489-538.

[15] R. Bauer, H. Fallmann, The photo-Fenton oxidation – a cheap and efficient wastewater treatment method, *Res. Chem. Intermed.*, 1997, 23, 341-354.

[16] O.A.H. Jones, P.G. Green, N. Voulvoulis, J.N. Lester, Questioning the excessive use of advanced treatment to remove organic micropollutants from wastewater, *Environ. Sci. Technol.*, 2007, 41, 5085-5089.

[17] I. Munoz, J. Rieradevall, F. Torrades, J. Peral, X. Domenech, Environmental assessment of different solar driven advanced oxidation processes, *Sol. Energy*, 2005, 79, 369-375.

[18] J. Kim, W. Choi, Hydrogen producing water treatment through solar photocatalysis, *Energy Environ. Sci.*, 2010, 3, 1042-1045.

[19] H. Park, W. Choi, M.R. Hoffmann, Effects of the preparation method of the ternary CdS/TiO_2/Pt hybrid photocatalysts on visible light-induced hydrogen production, *J. Mater. Chem.*, 2008, 18, 2379-2385.

[20] G.R. Dey, A.D. Belapurkar, K. Kishore, Photo-catalytic reduction of carbon dioxide to methane using TiO2 as suspension in water, *J. Photochem. Photobiol. A-Chem.*, 2004, 163, 503-508.

[21] G.-H. Moon, W. Kim, A.D. Bokare, N.-e. Sung, W. Choi, Solar production of H_2O_2 on reduced graphene oxide-TiO_2 hybrid photocatalysts consisting of earth-abundant elements only, *Energy Environ. Sci.*, 2014, 7, 4023-4028.

[22] G.-H. Moon, D.-h. Kim, H.-i. Kim, A.D. Bokare, W. Choi, Platinum-like behavior of reduced graphene oxide as cocatalyst on TiO_2 for the efficient photocatalytic oxidation of arsenite, *Environ. Sci. Technol. Lett.*, 2014, 1, 185-190.

[23] M. Yin, Z. Li, J. Kou, Z. Zou, Mechanism investigation of visible light-induced degradation in a heterogeneous TiO2/Eosin γ/rhodamine B system, *Environ. Sci. Technol.*, 2009, 43, 8361-8366.

[24] M.A. Rauf, N. Marzouki, B.K. Korbahti, Photolytic decolorization of Rose Bengal by UV/H_2O_2 and data optimization using response surface method, J. Hazard. Mater., 2008, 159, 602-609.

[25] D.B. Hamal, K.J. Klabunde, Valence state and catalytic role of cobalt ions in cobalt TiO2 nanoparticle photocatalysts for acetaldehyde degradation under visible light, *J. Phys. Chem. C*, 2011, 115, 17359-17367.

[26] J. Schneider, M. Matsuoka, M. Takeuchi, J. Zhang, Y. Horiuchi, M. Anpo, D.W. Bahnemann, Understanding TiO_2 photocatalysis: mechanisms and materials, *Chem. Rev.*, 2014, 114(19), 9919-9986.

[27] R. Yuan, D. Liu, S. Wang, B. Zou, F. Ma, Enhanced photocatalytic oxidation of humic acids using Fe^{3+}-Zn^{2+} co-doped TiO_2: The effects of ions in aqueous solutions, *Environ. Eng. Res.*, 2018, 23(2), 181-188.

[28] S. Kim, S.-J. Hwang, W. Choi, Visible-light-induced photocatalytic degradation of 4-chlorophenol and phenolic compounds in aqueous suspension of pure titania: demonstrating the existence of a surface-complex-mediated path, *J. Phys. Chem. B*, 2005, 109(51), 24260-24267.

[29] M. Kang, The superhydrophilicity of Al-TiO_2 nanometer sized material synthesized using a solvothermal method, *Mater. Lett.*, 2005, 59(24-25), 3122-3127.

[30] M. Pelaez, N.T. Nolan, S.C. Pillai, M.K. Seery, P. Falaras, A.G. Kontos, P.S.M. Dunlop, J.W.J. Hamilton, J.A. Byrne, K. O'Shea, M.H. Entezari, D.D. Dionysiou, A review on the visible light active titanium dioxide photocatalysts for environmental applications, *Appl. Catal. B-Environ.*, 2012, 125, 331-349.

[31] J.C. Yu, W. Ho, J. Yu, H. Yip, P.K. Wong, J. Zhao, Efficient visible-light-induced photocatalytic disinfection on sulfur-doped nanocrystalline titania, *Environ. Sci. Technol.*, 2005, 39(4), 1175-1179.

[32] S. In, A. Orlov, R. Berg, F. Garcia, S. Pedrosa-Jimenez, M.S. Tikhov, D.S. Wright and R.M. Lambert. Effective visible light-activated B-doped and B,N-codoped TiO_2 photocatalysts, *J. Am. Chem. Soc.*, 2007, 129(45), 13790-13791.

[33] P. Periyat, S.C. Pillai, D.E. McCormack, J. Colreavy, S.J. Hinder, Improved high-temperature stability and sun-light-driven photocatalytic activity of sulfur-doped anatase TiO_2, *J. Phys. Chem. C*, 2008, 112(20), 7644-7652.

[34] K. Selvam, M. Swaminathan, Nano N-TiO_2 mediated selective photocatalytic synthesis of quinaldines from nitrobenzenes, *RSC Adv.*, 2012, 2(7), 2848-2855.

[35] E.M. Neville, J.M.D. MacElroy, K.R. Thampi, J.A. Sullivan, Visible light active C-doped titanate nanotubes prepared via alkaline hydrothermal treatment of C-doped nanoparticulate TiO_2: Photo-electrochemical and photocatalytic properties, *J. Photochem. Photobiol. A-Chem.*, 2013, 267, 17-24.

[36] T. Umebayashi, T. Yamaki, H. Itoh, K. Asai, Band gap narrowing of titanium dioxide by sulfur doping, *Appl. Phys. Lett.*, 2002, 81(3), 454-456.

[37] T. Umebayashi, T. Yamaki, S. Tanaka, K. Asai, Visible light-induced degradation of methylene blue on S-doped TiO_2, *Chem. Lett.*, 2003, 32, 330-331.

[38] T. Umebayashi, T. Yamaki, S. Tanaka, K. Asai, Sulfur-doping of rutile-titanium dioxide by ion implantation: Photocurrent spectroscopy and first-principles band calculation studies, *J. Appl. Phys.*, 93(9), 5156-5160.

[39] T. Ohno, T. Mitsui, M. Matsumura, Photocatalytic activity of S-doped TiO_2 photocatalyst under visible light, Chem. Lett., 2003, 32(4), 364-365.

[40] T. Ohno, M. Akiyoshi, T. Umebayashi, K. Asai, T. Mitsui, M. Matsumura, Preparation of S-doped

TiO_2 photocatalysts and their photocatalytic activities under visible light, *Appl. Catal. A*, 265, 115-121.

[41] X. Li, C. Chen, J. Zhao, Mechanism of photodecomposition of H_2O_2 on TiO_2 surfaces under visible light irradiation, *Langmuir*, 2001, 17, 4118-4122.

[42] T. Ohno, Y. Masaki, S. Hirayama, M. Matsumura, TiO_2-photocatalyzed epoxidation of 1-decene by H_2O_2 under visible light, *J. Catal.*, 2001, 204, 163–168.

[43] M.V. Shankar, T. Kako, D.W.J. Ye, One-pot synthesis of peroxo-titania nanopowder and dual photochemical oxidation in aqueous methanol solution, *J. Colloid Interf. Sci.*, 2009, 331, 132-137.

[44] T. Liu, X. Li, X. Yuan, Y. Wang, F. Li, Enhanced visible-light photocatalytic activity of a TiO_2 hydrosol assisted by H_2O_2: surface complexation and kinetic modeling, *J. Mol. Catal. A-Chem.*, 2016, 414, 122-129.

[45] V. Etacheri, M.K. Seery, S.J. Hinder, S.C. Pillai, Oxygen rich titania: a dopant free, high temperature stable, and visible-light active anatase photocatalyst, *Adv. Funct. Mater.*, 2011, 21, 3744-3752.

[46] L.–L. Tan, W.–J. Ong, S.–P. Chai, A.R. Mohamed, Band gap engineered, oxygen-rich TiO_2 for visible light induced photocatalytic reduction of CO_2, *Chem. Commun.*, 2014, 50, 6923-6926.

[47] W. Chu, Y.F. Rao, Photocatalytic oxidation of monuron in the suspension of WO_3 under the irradiation of UV-visible light, *Chemosphere*, 2012, 86, 1079-1086.

[48] M. Muneer, J. Theurich, D. Bahnemann, Titanium dioxide mediated photocatalytic degradation of 1,2-diethylphthalate, *J. Photochem. Photobiol. A-Chem.*, 2001, 143, 213-219.

[49] U. Cernjgoj, U.L. Stangar, P. Trebse, Degradation of neonicotinoid insecticides by different advanced oxidation processes and studying the effect of ozone on TiO_2 photocatalysis, *Appl. Catal. B-Environ.*, 2007, 75, 229-238.

[50] A. Durán, J.M. Monteagudo, Solar photocatalytic degradation of reactive blue 4 using a Fresnel lens. *Water Res.*, 2007, 41, 690-698.

[51] H.E. Kim, J. Lee, H. Lee, C. Lee, Synergistic effects of TiO_2 photocatalysis in combination with Fenton-like reactions on oxidation of organic compounds at circumneutral pH, *Appl. Catal. B-Environ.*, 2012, 115, 219–224.

[52] H. Lee, J. Choi, S. Lee, S.-T Yun, C. Lee, J. Lee, Kinetic enhancement in photocatalytic oxidation of organic compounds by WO_3 in the presence of Fenton-like reagent, *Appl. Catal. B-Environ.*, 2013, 138-139, 311-317.

[53] S. Cao, J. Yu, g-C_3N_4-based photocatalysts for hydrogen generation, *J. Phys. Chem. Lett.*, 2014, 5, 2101−2107.

[54] X. Wang, S. Blechert, M. Antonietti, Polymeric graphitic carbon nitride for heterogeneous photocatalysis, *ACS Catal.*, 2012, 2, 1596−1606.

[55] J. Low, S. Cao, J. Yu, S. Wageh, Two-dimensional layered composite photocatalysts, *Chem.*

Commun., 2014, 50, 10768−10777.

[56] C. Butchosa, P. Guiglion, M.A. Zwijnenburg, Carbon nitride photocatalysts for water splitting: a computational perspective, *J. Phys. Chem. C*, 2014, 118, 24833−24842.

[57] H. Zhang, X. Zuo, H. Tang, G. Li, Z. Zhou, Origin of photoactivity in graphitic carbon nitride and strategies for enhancement of photocatalytic efficiency: insights from first-principles computations, *Phys. Chem. Chem. Phys.*, 2015, 17, 6280−6288.

[58] G. Dong, W. Ho, Y. Li, L. Zhang, Facile synthesis of porous graphene-like carbon nitride ($C_6N_9H_3$) with excellent photocatalytic activity for NO removal, *Appl. Catal. B*, 2015, 174−175, 477−485.

[59] J. Fang, H. Fan, M. Li, C. Long, Nitrogen self-doped graphitic carbon nitride as efficient visible light photocatalyst for hydrogen evolution, *J. Mater. Chem. A*, 2015, 3, 13819−13826.

[60] L. Shi, T. Wang, H. Zhang, K. Chang, J. Ye, Electrostatic self-assembly of nanosized carbon nitride nanosheet onto a zirconium metal−organic framework for enhanced photocatalytic CO_2 reduction, *Adv. Funct. Mater.*, 2015, 25, 5360−5367.

[61] M. Tahir, N. Mahmood, J. Zhu, A. Mahmood, F.K. Butt, S. Rizwan, I. Aslam, M. Tanveer, F. Idrees, I. Shakir, One dimensional graphitic carbon nitrides as effective metal-free oxygen reduction catalysts, *Sci. Rep.*, 2015, 5, 12389.

[62] J. Bian, Q. Li, C. Huang, J. Li, Y. Guo, M. Zaw, R.-Q. Zhang, Thermal vapor condensation of uniform graphitic carbon nitride films with remarkable photocurrent density for photoelectrochemical applications, *Nano Energy*, 2015, 15, 353−361.

[63] J. Oh, R.J. Yoo, S.Y. Kim, Y.J. Lee, D.W. Kim, S. Park, Oxidized carbon nitrides: water-dispersible, atomically thin carbon nitride-based nanodots and their performances as bioimaging probes, *Chem. - Eur. J.*, 2015, 21, 6241−6246.

[64] G. Zhang, M. Zhang, X. Ye, X. Qiu, S. Lin, X. Wang, Iodine modified carbon nitride semiconductors as visible light photocatalysts for hydrogen evolution, *Adv. Mater.*, 2014, 26, 805−809.

[65] Y. Wang, H. Li, J. Yao, X. Wang, M. Antonietti, Synthesis of boron doped polymeric carbon nitride solids and their use as metal-free catalysts for aliphatic C-H bond oxidation, *Chem. Sci.*, 2011, 2, 446−450.

[66] T.Y. Ma, Y. Tang, S. Dai, S.Z. Qiao, Proton-functionalized two-dimensional graphitic carbon nitride nanosheet: an excellent metal-/label-free biosensing platform, *Small*, 2014, 10, 2382−2389.

[67] Q. Liang, Z. Li, Z.-H. Huang, F. Kang, Q.-H. Yang, Holey graphitic carbon nitride nanosheets with carbon vacancies for highly improved photocatalytic hydrogen production, *Adv. Funct. Mater.*, 2015, 25, 6885−6892.

[68] J. Liu, W. Li, L. Duan, X. Li, L. Ji, Z. Geng, K. Huang, L. Lu, L. Zhou, Z. Liu, A graphene-like oxygenated carbon nitride material for improved cycle-life lithium/sulfur batteries, *Nano Lett.*, 2015,

15, 5137−5142.

[69] X. Song, Y. Hu, M. Zheng, C. Wei, Solvent-free in situ synthesis of g-C_3N_4/{001}TiO_2 composite with enhanced UV- and visible-light photocatalytic activity for NO oxidation, *Appl. Catal., B-Environ.*, 2016, 182, 587−597.

[70] Z. Zhang, D. Jiang, D. Li, M. He, M. Chen, M. Construction of $SnNb_2O_6$ nanosheet/g-C_3N_4 nanosheet two-dimensional heterostructures with improved photocatalytic activity: synergistic effect and mechanism insight, *Appl. Catal., B-Environ.*, 2016, 183, 113−123.

[71] D.H. Wang, J.N. Pan, H.H. Li, J.J. Liu, Y.B. Wang, L.T. Kang, J.N. Yao, A pure organic heterostructure of μ-oxo dimeric iron(III) porphyrin and graphitic-C_3N_4 for solar H_2 reduction from Water, *J. Mater. Chem. A,* 2016, 4, 290−296.

[72] C.A. Paez, D.Y. Liquet, C. Calberg, S.D. Lambert, I. Willems, A. Germeau, J.P. Pirard, B. Heinrichs, Study of photocatalytic decomposition of hydrogen peroxide over ramsdellite-MnO_2 by O_2-pressure monitoring, *Catal. Commun.*, 2011, 15, 132–136.

[73] J. Liu, Y. Liu, N.Y. Liu, Y.Z. Han, X. Zhang, H. Huang, Y. Lifshitz, S.T. Lee, J. Zhong, Z.H. Kang, Metal-free efficient photocatalyst for stable visible water splitting via a two-electron pathway, *Science*, 2015, 347, 970–974.

[74] Y. Shiraishi, S. Kanazawa, Y. Sugano, D. Tsukamoto, H. Sakamoto, S. Ichikawa, T. Hirai, Highly selective production of hydrogen peroxide on graphitic carbon nitride (g-C_3N_4) photocatalyst activated by visible light, *ACS Catal.*, 2014, 4, 774–780.

[75] G.H. Moon, M. Fujitsuka, S. Kim, T. Majima, X.C. Wang, W. Choi, Eco-friendly photochemical production of H_2O_2 through O_2 reduction over carbon nitride frameworks incorporated with multiple heteroelements, *ACS Catal.*, 2017, 7, 2886–2895.

[76] M.V. Dozzi, L. Prati, P. Canton, E. Selli, Effects of gold nanoparticles deposition on the photocatalytic activity of titanium dioxide under visible light, *Phys. Chem. Chem. Phys.*, 2009, 11, 7171–7180.

[77] D. Tsukamoto, A. Shiro, Y. Shiraishi, Y. Sugano, S. Ichikawa, S. Tanaka, T. Hirai, Photocatalytic H2O2 production from ethanol/O_2 system using TiO_2 loaded with Au-Ag bimetallic alloy nanoparticles, *ACS Catal.*, 2012, 2, 599–603.

[78] W.C. Wan, S. Yu, F. Dong, Q. Zhang, Y. Zhou, Efficient C_3N_4/graphene oxide macroscopic aerogel visible-light photocatalyst, *J. Mater. Chem. A*, 2016, 4, 7823–7829.

[79] Q.J. Xiang, J.G. Yu, M. Jaroniec, Preparation and enhanced visible-light photocatalytic H_2-production activity of graphene/C_3N_4 composites, *J. Phys. Chem. C*, 2011, 115, 7355–7363.

[80] Y. Kofuji, S. Ohkita, Y. shiraishi, H. Sakamoto, S. Ichikawa, S. Tanaka, T. Hirai, Mellitic triimide-doped carbon nitride as sunlight-driven photocatalysts for hydrogen peroxide production, *ACS Sustainable Chem. Eng.*, 2017, 5, 6478-6485.

[81] H.-i. Kim, Y. Choi, S. Hu, W. Choi, J.-H. Kim, Photocatalytic hydrogen peroxide production by anthraquinone-augmented polymeric carbon nitride, *Appl. Catal. B-Environ.*, 2018, 229, 121-129.

[82] S. Zhao, T. Guo, X. Li, T. Xu, B. Yang, X. Zhao, Carbon nanotubes covalent combined with graphitic carbon nitride for photocatalytic hydrogen peroxide production under visible light, *Appl. Catal. B-Environ.*, 2018, 224, 725-732.

[83] Y. Gao, Y. Masuda, K. Koumoto, Light-excited superhydrophilicity of amorphous TiO_2 thin films deposited in an aqueous peroxotitanate solution, *Langmuir*, 2004, 20, 3188–3194.

[84] G. Munuera, A.R. González–Elipe, A. Fernández, P. Malet, J.P. Espinós, Spectroscopic characterization and photochemical behavior of a titanium hydroxyperoxo compound, *J. Chem. Soc., Faraday Trans. 1*, 1989, 85, 1279–1290.

[85] S. Kim, W. Choi, Visible-light induced photocatalytic degradation of 4-chlorophenol and phenolic compounds in aqueous suspension of pure titania: demonstrating the existence of a surface-complex-mediated path, *J. Phys. Chem. B*, 2005, 109, 5143-5149.

[86] M. Cho, H. Chung, W. Choi, J. Yoon, Different inactivation behaviors of MS-2 phage and *Escherichia coli* in TiO_2 photocatalytic disinfection, *Appl. Environ. Microbiol.*, 2005, 71, 270-275.

[87] S. Kim, W. Choi, Dual photocatalytic pathways of trichloroacetate degradation on TiO_2: effects of nanosized platinum deposits on kinetics and mechanism, *J. Phys. Chem. B*, 2002, 106, 13311-13317.

[88] H. Park, Y. Park, W. Kim, W. Choi, Surface modification of TiO_2 photocatalyst for environmental applications, *J. Photochem. Phobiol. C-Photochem. Rev.*, 2013, 15, 1–20.

[89] L. Brunet, D.Y. Lyon, E.M. Hotze, P.J.J. Alvarez, M.R. Wiesner, comparative photoactivity and antibacterial properties of C_{60} fullerenes and titanium dioxide nanoparticles, *Environ. Sci. Technol.*, 2009, 43, 4355-4360.

[90] J. Theurich, M. Lindner, D. W. Bahnemann, Photocatalytic degradation of 4-chlorophenol in aerated aqueous titanium dioxide suspensions: a kinetic and mechanistic study, *Langmuir*, 1996, 12, 6368-6376.

[91] K. Vinodgopal, U. Stafford, K.A. Gray, P.V. Kamat, Electrochemically assisted photocatalysis. 2. the role of oxygen and reaction intermediates in the degradation of 4-chlorophenol on immobilized TiO_2 particulate films, *J. Phys. Chem.*, 1994, 98, 6796-6803.

[92] X. Li, J.W. Cubbage, T.A. Tetzlaff, W. S. Jenks, Photocatalytic degradation of 4-chlorophenol. 1. the hydroquinone pathway, *J. Org. Chem.*, 1999, 64, 8509-8524.

[93] X. Li, J.W. Cubbage, W.S. Jenks, Photocatalytic degradation of 4-chlorophenol. 2. the 4-chlorocatechol pathway, *J. Org. Chem.*, 1999, 64, 8525-8536.

[94] S. Sakthivel, M. Janczarek, H. Kisch, Visible light activity and photoelectrochemical properties of nitrogen-doped TiO_2, *J. Phys. Chem. B*, 2004, 108, 19384-19387.

[95] W. Ho, J. C. Yu, S. Lee, Low-temperature hydrothermal synthesis of S-doped TiO2 with visible light photocatalytic activity, *J. Solid State Chem.*, 2006, 179, 1171-1176.

[96] H. Sun, Y. Bai, Y. Cheng, W. Jin, N. Xu, Preparation an characterization of visible-light-driven carbon-sulfur-codoped TiO2 photocatalysts, *Ind. Eng. Chem. Res.*, 2006, 45, 4971-4976.

[97] M. Nasir, S. Bagwasi, Y. Jiao, F. Chen, B. Tian, J. Zhang, Characterization and activity of the Ce and N co-doped TiO_2 prepared through hydrothermal method, *Chem. Eng. J.*, 2014, 236, 388–397.

[98] G.V. Buxton, C.L. Greenstock, W.P. Helman, A.B. Ross, Critical review of rate constants for reactions of hydrated electrons, hydrogen atoms and hydroxyl radicals ($^{\bullet}OH/^{\bullet}O^{-}$) in aqueous solution, *J. Phys. Chem. Ref. Data*, 1998, 17, 513–886.

[99] J. Kim, J. Lee, W. Choi, Synergic effect of simultaneous fluorination and platinization of TiO_2 surface on anoxic photocatalytic degradation of organic compounds, *Chem. Commun.*, 2006, 6, 756-758.

[100] S. Kim, S.-J. Hwang, W. Choi, Visible light active platinum-ion-doped TiO_2 photocatalyst, *J. Phys. Chem. B*, 2005, 109, 24260-24267.

[101] G. Kim, W. Choi, Charge-transfer surface complex of EDTA-TiO_2 and its effect on photocatalysis under visible light, *Appl. Catal. B-Environ.*, 2010, 100, 77-83.

[102] K.V. Baiju, P. Periyat, P.K. Pillai, P. Mukundan, K.G.K. Warrier, W. Wunderlich, Enhanced photoactivity and anatase thermal stability of silica–alumina mixed oxide additives on sol–gel nanocrystalline titania, *Mater. Lett.*, 2007, 61, 1751.

[103] X. Wang, J.C. Yu, P. Liu, X. Wang, W. Sua, X. Fua, Probing of photocatalytic surface sites on SO_4^{2-}/TiO_2 solid acids by in situ FT-IR spectroscopy and pyridine adsorption, *J. Photochem. Photobiol. A-Chem.*, 2006, 179, 339–347.

[104] S. Sakthivel, H. Kisch, Daylight photocatalysis by carbon-modified titanium dioxide, *Angew. Chem. Int. Edit.*, 2003, 42(40), 4908-4911.

[105] L.G. Devi, B. Nagaraj, K.E. Rajashekhar, Synergistic effect of Ag deposition and nitrogen doping in TiO_2 for the degradation of phenol under solar irradiation in presence of electron acceptor, *Chem. Eng. J.*, 2012, 181-182, 259-266.

[106] P.X. Qiu, H. Chen, C.M. Xu, N. Zhou, F. Jiang, X. Wang, Y.S. Fu, Fabrication of an exfoliated graphitic carbon nitride as a highly active visible light photocatalyst, *J. Mater. Chem. A*, 2015, 3, 24237–24244.

[107] S. Martha, A. Nashim, K.M. Parida, Facile synthesis of highly active g-C_3N_4 for efficient hydrogen production under visible light, *J. Mater. Chem. A*, 2013, 1(26), 7816–7824.

[108] M. Xu, L. Han, S.J. Dong, Facile fabrication of highly efficient g-C_3N_4/Ag_2O heterostructured photocatalysts with enhanced visible-light photocatalytic activity, *ACS Appl. Mater. Interfaces,*, 2013, 5(23), 12533–12540.

[109] M. Higo, T. Miake, M. Mitsushio, T. Yoshidome, Y. Ozono, Adsorption state and morphology of anthraquinone-2-carboxylic acid deposited from solution onto the atomically-smooth native oxide surface of Al(111) films studied by infrared reflection absorption spectroscopy, X-ray photoelectron spectroscopy, and atomic force microscopy, *Anal. Sci.*, 2008, 24, 313–320.

[110] M. Srivastava, S.K. Srivastava, N.R. Nirala, R. Prakash, A chitosan-based polyaniline–Au nanocomposite biosensor for determination of cholesterol, *Anal. Methods*, 2014, 6, 817–824.

[111] H.S. Randhawa, J.L. Kapoor, CN stretching frequencies in amide systems, *J. Comput. Chem.*, 1981, 2, 12–13.

[112] W. Chen, L.J. Huang, J. Hu, T.F. Li, F.F. Jia, Y.F. Song, Connecting carbon nanotubes to polyoxometalate clusters for engineering high-performance anode materials, *Phys. Chem. Chem. Phys.*, 2014, 16, 19668–19673.

[113] Q. Huang, J.G. Yu, S.W. Cao, C. Cui, B. Cheng, Efficient photocatalytic reduction of CO_2 by amine-functionalized g-C_3N_4, *Appl. Surf. Sci.*, 2015, 358, 350–355.

[114] S.W. Han, S.W. Joo, T.H. Ha, Y. Kim, K. Kim, Adsorption characteristics of anthraquinone-2-carboxylic acid on gold, *J. Phys. Chem. B*, 2000, 104, 11987–11995.

[115] B.C. Zhu, P.F. Xia, W.K. Ho, J.G. Yu, Isoelectric point and adsorption activity of porous g-C_3N_4, *Appl. Surf. Sci.*, 2015, 344, 188–195.

[116] C. Goel, H. Bhunia, P.K. Bajpai, Synthesis of nitrogen doped mesoporous carbons for carbon dioxide capture, *RSC Adv.*, 2015, 5, 46568–46582.

[117] Q. Su, J. Sun, J.Q. Wang, Z.F. Yang, W.G. Cheng, S.J. Zhang, Urea-derived graphitic carbon nitride as an efficient heterogeneous catalyst for CO_2 conversion into cyclic carbonates, *Catal. Sci. Technol.*, 2014, 4, 1556–1562.

감사의 글

2009년 3월, 아직 캠퍼스가 덜 만들어져 모래바람이 부는 UNIST라는 생소한 대학에 와서 어느덧 10년이라는 시간이 지났습니다. 처음으로 외지 생활을 시작하며 '과연 잘 해 나갈 수 있을까?' 라는 걱정을 하며 학교를 다니기 시작했는데 벌써 박사 졸업을 앞두게 되어 감회가 남다릅니다.

학부 과정이 끝나갈 무렵, 대학원 진학을 위해 실험실을 정해야 하는데 아직 어떤 실험실을 선택해야 할 지 고민을 하고 있던 찰나에 저에게 우리 실험실로 오라고 이야기 주시던 이창하 교수님의 목소리가 아직도 기억에 남아있습니다. 이런 저런 생각들로 고민만 계속 하고 있을 때 교수님의 한 마디로 모든 생각들이 정리가 되었습니다. 지금 돌이켜보면 좋은 선택을 했다는 생각이 듭니다. 실험실 생활을 하면서 교수님의 연구를 하는 방법과 연구에 대한 열정을 배울 수 있었고, 무엇보다 저에게 한참 부족했던 자신감을 키울 수 있었습니다. 아직 여러모로 부족하지만 교수님의 가르침에 맞춰 더 발전할 수 있도록 하겠습니다.

이번 학위논문 심사에 참석 해 주셨던 교수님들께도 감사의 말을 전달 드립니다. 학부 과정 중에도 많은 도움을 주셨고, 이번 학위 논문심사에서도 여러 조언을 주셨던 권영남 교수님, 이창수 교수님, 조경화 교수님께 감사의 인사를 전달 드립니다. 또한, 이번 학위논문 심사에 참석 해 주셔서 광촉매의 연구 방향을 바로잡아 주셨던 포항공과대학교 조강우 교수님께도 감사의 인사를 전달 드립니다.

기나긴 6년의 대학원 기간동안 같이 동고동락을 하며 많은 도움을 준 선배님들과 동료, 후배들에게도 감사의 인사를 전달합니다. 실험실의 연구 분위기 조성에 최선을 다하셨던 이홍신 박사님, 부족한 모습을 보였던 저를 이곳 저곳에서 많은 도움을 주셨던 ARTlab의 어머니 김형은 박사님, 연구실의 첫 실험부터 졸업의 마지막 논문까지 도움을 주셨던 저의 사수 이혜진 박사님, 실험실의 첫 유부남이자 도희, 한결이에게 자랑스러운 아버지 김민식 박사님, 나긋한 모습과 밝은 웃음소리로 실험실의 분위기를 밝게 만들어 주었던 민정누나, 저의 첫 부사수이자 인생선배로서 사회 생활에 대한 많은 조언을 줬던 준영이 형, 나의 동기이자 실험실의 아이디어 뱅크 학현이, 조금은 독특하지만 본인의 일에 최선을 다 할 줄 아는 기명이, 조만간 소독으로 Nature와 Science에 논문을 투고

할 태완이, 아쉽게도 2인자가 될 거지만 아직까지는 실험실의 최장신 형진이, 실험실의 아이돌 조퀸 지윤이, 토양오염 처리의 대가가 될 예비 박사 현석이, 당차고 활기찬 모습을 보여주는 지혜, FBR 연구 메이트로 고생이 많았지만 앞으로는 미생물 연구로 승승장구할 중훈이, 고원자가 연구를 통해 실험실 연구의 중심축을 맡게 될 동현이, 옆에서 성실하게 일을 도와 주어 내 걱정을 덜어주는 수연이, 아쉽게도 ARTlab을 떠나게 되었지만 고려대에서 좋은 연구들을 계속 진행하게 될 재민이에게 감사의 인사를 전합니다. 그리고 아직 제대로 만나보지 못했지만 이번에 대학원에 입학하게 된 종우와 동원이에게는 앞으로의 대학원 생활에 좋은 일들이 가득하기를 응원합니다.

마지막으로 아직까지도 철없이 응석을 부리고 있는 아들을 묵묵히 응원해 주시고 한결같은 사랑으로 도움을 주시는 아버지, 어머니와 힘들 때마다 전화를 통해 항상 응원의 메시지를 전달해 주던 누나에게도 감사의 마음을 전달합니다. 그리고 친형과도 같이 항상 챙겨 주시는 매형에게도 감사의 말을 전달합니다. 아직 여러모로 부족하지만 그 부족함을 채워준 모든 분들에게 감사의 말을 전달하고, 또한 도와 주신 부분에 대해 보답을 할 수 있도록 더욱더 발전하도록 하겠습니다.

2019년 1월 ART lab에서